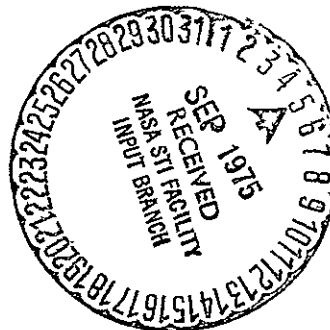# NASA TECHNICAL MEMORANDUM

NASA TM X- 62,463

PARTICLE MOTION IN ATMOSPHERIC BOUNDARY LAYERS OF MARS AND EARTH

Bruce R. White
University of California, Davis, CA 95616

James D. Iversen
Iowa State University, Ames, IA 50010

Ronald Greeley
University of Santa Clara
   and
Ames Research Center, Moffett Field, CA 94035

James B. Pollack
Ames Research Center, Moffett Field, CA 94035

August 1975

1. Report No. TM X-62,463	2. Government Accession No.	3. Recipient's Catalog No.
4. Title and Subtitle PARTICLE MOTION IN ATMOSPHERIC BOUNDARY LAYERS OF MARS AND EARTH		5. Report Date
		6. Performing Organization Code
7. Author(s) Bruce R. White,[1] James D. Iversen,[2] Ronald Greeley,[3] and James B. Pollack[4]		8. Performing Organization Report No. A-6210
9. Performing Organization Name and Address [1]University of California, Davis, CA 95616 [2]Iowa State University, Ames, Iowa 50010 [3]University of Santa Clara and Ames Research Center, NASA, Moffett Field, CA 94035 [4]Ames Research Center, NASA, Moffett Field, CA 94035		10. Work Unit No. 384-50-60
		11. Contract or Grant No.
12. Sponsoring Agency Name and Address National Aeronautics and Space Administration Washington, D.C. 20546		13. Type of Report and Period Covered Technical Memorandum
		14. Sponsoring Agency Code

15. Supplementary Notes

16. Abstract   In view of recent imagery received from the Mariner 9 spacecraft showing evidence of variable surface features and surface erosion resulting from atmospheric winds, a renewed interest has occurred in the eolian mechanics of saltating particles. To study this phenomenon both an experimental investigation of the flow field around a model crater in an atmospheric boundary layer wind tunnel and numerical solutions of the two- and three-dimensional equations of motion of a single particle under the influence of a turbulent boundary layer were conducted. Two-dimensional particle motion was calculated for flow near the surfaces of both Earth and Mars. For the case of Earth both a turbulent boundary layer with a viscous laminar sublayer and one without were calculated. For the case of Mars it was only necessary to calculate turbulent boundary layer flow with a laminar sublayer because of the low values of friction Reynolds number; however, it was necessary to include the effects of slip flow on a particle caused by the rarefied Martian atmosphere. In the equations of motion the lift force functions were developed to act on a single particle only in the laminar sublayer or a corresponding small region of high shear near the surface for a fully turbulent boundary layer. The lift force functions were developed from the analytical work by Saffman concerning the lift force acting on a particle in simple shear flow.

The numerical solutions for Earth were used to develop an approximate solution for the transition region and were empirically adjusted to agree with the experimental data. These modified equations were then solved to estimate particle motion under Mars surface conditions. These calculations show the importance of a lift force used in both Mars and Earth calculations.

Major findings include a comparison between Earth and Mars particle trajectories for equal ratios of friction to threshold friction speeds that shows Mars length scales in trajectories to be larger and with higher terminal particle velocities with lower collision angles at the surface than Earth's. Other significant results include simulated particle flow in the wake of a crater with a horseshoe vortex that shows extremely high terminal velocities and smaller than normal collision angles, especially for smaller particles, resulting in high erosion rates at the surface. Further, turbulence was shown not to play a major role in shaping particle trajectories, except for small particles. Also, particle rebound resulting from an inelastic collision at the Martian surface was calculated and showed increasing trajectory lengths for increasing momentum retained upon collision.

17. Key Words (Suggested by Author(s)) Planetary boundary layer Grain saltation Flow around crater	18. Distribution Statement Unlimited STAR Categories - 34, 88, 91

19. Security Classif. (of this report) Unclassified	20. Security Classif. (of this page) Unclassified	21. No. of Pages 211	22. Price* $7.25

TABLE OF CONTENTS

SYMBOLS AND NOTATION[1]

A	threshold friction speed parameter, $u_{*t}/\sqrt{\rho_p g D_p/\rho}$ or the numerical factor in rarefied flows depending upon the nature of the reflection of the gas molecules from the particle surface $(=\beta/\lambda)$
A_1, A_2, A_3, A_4	constant empirical numerical coefficients used in the friction threshold determination
B	particle friction Reynolds number $(=u_{*t} D_p/\nu)$
B_1	constant of the Riccati equation $(=3K_3\,\rho_g/4D_p\rho_p)$
c	exponential constant used in correction factor of slip flow $(=1.10)$
c_p	specific heat at constant pressure
C_1	constant
C_D	drag coefficient $[=\text{drag force}/(1/2\rho V_r^2 S_A)]$
C_L	lift coefficient $[=\text{lift force}/(1/2\rho V_r^2 S_A)]$
D	drag force
$\underline{D}$	vector drag force
D_c	crater rim diameter
D_p	particle diameter
D_x, D_y, D_z	directional cosines of the vector drag force
e	coefficient of restitution
E_c	Eckert number $(=U_o^2/c_{p_o}(\Delta\bar{T})_o)$
f_1	function that relates vortex crossflow velocity to u_{*r_1}
f_2	empirical wall effect function for vortex crossflow

---

[1]Symbols and notation not in this list are defined and used locally within the text.

F	force
F_{am}	apparent mass force
F_B	Basset force
F_{mo}	resistance for molecular-regime particle motion
F_{pg}	pressure gradient force
g	acceleration of gravity
G_g	mean velocity of gas molecules
h	ripple height or reference height
H	heat flux at planet surface or boundary layer shape factor $(=\delta^*/\theta)$
$\underline{i},\underline{j},\underline{k}$	unit normal vectors of orthogonal coordinate system x, y, and z respectively
k	von Karman's universal constant (≈ 0.4)
K	apparent mass coefficient, equal to 2/3 for solid spherical particles
k_1, k_2, k_3	numerical constants associated with drag coefficients (see Appendix A)
ℓ	length
ℓ_t	wake length
L	reference length or lift force
$\underline{L}$	vector lift force
L*	Monin-Obukhov Stability length, $L^* = u_*^3 c_p \rho T/kgH$ (where c_p is specific heat, T is temperature, H is heat flux at surface)
L_x, L_y, L_z	directional cosines of the vector lift force
m	mass
m_g	mass of gas molecules
m_p	particle mass

M	overturning moment exerted on a particle
p	pressure
Pr	Prandtl number $(=c_{p_o}\rho_o/\mu_o)$
r	magnitude of position vector or distance between particle and vortex core
$\underline{r}$	position vector
r_1	vortex core radius
R	Reynolds number $(=V_r D_p/\nu)$
R_f	friction Reynolds number $(=u_* D_p/\nu)$
R_H	crater rim height
Ri	bulk Richardson number $(=(\Delta\bar{\bar{T}})_o L_o g_o/T_o U_o^2)$
R_κ	Reynolds number $(=\rho\kappa D_p^2/\nu)$
Ro	Rossby number $(=U_o/L_o\Omega_o)$
R_ν	Reynolds number $(=V_r D_p/\nu)$
S	shear $(=\partial V_r/\partial z)$
S_A	surface area, equal to $\pi D_p^2/4$ for a spherical particle
t	time
T	temperature or time
$\bar{T}_w$	mean temperature at $z = 0$
u	velocity
u_F	final particle velocity
u_g	gas speed
$\overline{u_i u_j}$	Reynolds stress velocity terms
u_∞	freestream speed
u_*	friction speed

$u_{*\ell}$	local friction speed
u_{*t}	friction threshold speed
u_{*un}	friction speed of undisturbed velocity profile
U, V, W	components of stream velocity x, y, and z, respectively
U_o	characteristic speed
U_p, V_p, W_p	components of particle velocity x, y, and z, respectively
$\underline{V}$	stream velocity vector
$\underline{V}_p$	particle velocity vector
V_r	magnitude of relative velocity
$\underline{V}_r$	relative velocity vector
V_{r_x}	x-component of relative velocity ($=U-\dot{x}$)
V_{r_y}	y-component of relative velocity ($=V-\dot{y}$)
V_{r_z}	z-component of relative velocity ($=W-\dot{z}$)
V_θ	tangential velocity component in the vortex
$V_{\theta_{eff}}$	effect velocity component in the vortex—
w	width
w_o	initial or maximum vertical velocity of a particle's trajectory
W	weight
W_s	sample width
x, y, z	coordinates of a particle's position
$\dot{x}, \dot{y}, \dot{z}$	components of a particle's velocity
X	correction factor of rarefied flow
y_{max}	maximum length of a particle's trajectory
z_{max}	maximum height of a particle's trajectory

z_0	roughness height
z_0'	roughness height in saltation
α	fraction of gas molecules undergoing diffuse reflection at a particle's surface
β	slip coefficient $(=\eta/\eta_e)$
γ	specific weight
Γ	vortex circulation strength
$\Delta\bar{T}$	temperature difference $\bar{T}-\bar{T}_w$
$(\Delta\bar{T})_0$	temperature difference $\bar{T}_0-\bar{T}_w$
δ	boundary layer thickness
$\delta*$	boundary layer displacement thickness
δ_{ij}	Kronecker delta (=0 for $i \neq j$; = 1 for i=j)
ε_{ijk}	alternating epsilon (permutation tensor)
η	viscosity of medium
η_e	coefficient of external friction
η_g	number of gas molecules in one cubic centimeter
θ	potential temperature or momentum thickness
θ'	fluctuation of temperature from the mean
κ	coefficient of thermal conductivity
λ	mean free path or ripple wave length
μ	absolute viscosity
ν	kinematic viscosity
ρ	mass density of planet's atmosphere
ρ_p	particle density
τ	shear stress or time
ϕ	dissipation function

ϕ_1, ϕ_2 functions of the one-dimensional Riccati particle equation of motion

ω magnitude of rotation

$\underset{\sim}{\omega}$ angular velocity vector

Ω angular velocity

Subscripts:[1]

$(\ )_o$ denotes reference quantity

$(\ )_m$ refers to model conditions

i,j,k represents standard tensor notation

$(\hat{\ })$ nondimensional quantity

$(\bar{\ })$ time averaged

$(\ )'$ instantaneous fluctuation from time average

$(\_)$ vector quantity

---

[1]Unless already presented earlier or used locally within the text.

PARTICLE MOTION IN ATMOSPHERIC

BOUNDARY LAYERS OF MARS AND EARTH

Bruce R. White[1]

James D. Iversen[2]

Ronald Greeley[3]

James B. Pollack[4]

[1]Mechanical Engineering Department, University of California
Davis, Calif. 95616

[2]Department of Aerospace Engineering, Iowa State University
Ames, Iowa 50010

[3]Physics Department, University of Santa Clara, Calif. 95053
(Mail Address: Space Science Division, Ames Research Center,
National Aeronautics and Space Administration,
Moffett Field, Calif. 94035)

[4]Space Sciences Division, Ames Research Center
National Aeronautics and Space Administration
Moffett Field, Calif. 94035

I. INTRODUCTION

The numerical calculation of particle trajectories under
the influence of two- and three-dimensional turbulent boundary
layers in an incompressible Newtonian fluid flow and the
experimental investigation of a three-dimensional downstream
flow field around an idealized raised rim crater are the
subjects of this study. Very few experimental investi-
gations have been performed on three-dimensional turbulent
boundary layer flow around a disturbing roughness element and
none are known to the author with specific application to flow
over a crater before this investigation was initiated. Also
of interest was the numerical study of particle trajectories
in a two-dimensional flow field under Martian surface condi-
tions in which the effect of the rarefied atmosphere is
included in the analysis. A combination of the particle
trajectories and three-dimensional flow field around a crater
is made by calculating a particle motion in the downstream
flow field of a crater for Mars conditions.

The study of particle movement and its associated
trajectory is one with far reaching interests. An obvious
case is that of wind erosion of soil and farm land. The study
of snow storms, dust, and sandstorms and control is important
to several regions of the earth and an important problem of
the future. Particle movement studies may even solve such
distant and complex problems as the Martian eolian phenomena.

Also important is the understanding of the complex turbulent

planetary boundary layer which moves the material.

The trajectories and movement of particles by an eolian

(wind blown) process is a complex phenomenon. A classical work

which deals with this problem is that of Bagnold (1941) in

which he derives the relationship of the basic parameters

based on data obtained from his field and wind tunnel studies.

The yield of experiments Bagnold performed was equations for

threshold friction speeds and mass transport of sand by wind.

These relations were recently expanded from the specific case

of movement of sand by wind to a general case of various

density materials and any type fluid media motion by Iversen

et al. (1973) and then to the case of low pressure flows (Mars)

by Iversen et al. (1975a).

Two-dimensional particle flow for surface conditions was

calculated for both cases of Earth and Mars. For the case of

Earth, a turbulent boundary layer with a viscous laminar sub-

layer and one without were calculated. For the case of Mars

it was only necessary to calculate turbulent boundary layer

flow with a laminar sublayer because of the low values of

friction Reynolds number; however, it was necessary to include

the effects of slip flow on a particle caused by the rarefied

atmosphere.

The effect of lift force on the initiation of particle

motion has long been thought to have a role in their movement.

This idea was analytically expressed by Saffman (1965, 1968). In the equations of motion. a lift force term was developed that acts on a single particle only in the laminar sublayer or a corresponding small region of high shear near the surface for a fully turbulent boundary layer. The lift force functions were developed from the analytical work of Saffman (1965) for a single particle in simple shear flow. The lift force functions were consequently modified by empirical factors to account for wall effect and to match the limited experimental data available for Earth. An estimated interpolation for particle flow in the transition region for the case of Earth surface conditions was made from a combination of the laminar and turbulent sublayer solutions. The lift force, although relatively large near the surface, diminishes very rapidly, increasing in height above the surface.

With use of the modified lift functions the simulated particle solution was numerically calculated for the Martian surface conditions. A comparison is made between the effects of the surface conditions of Mars and that of Earth on the motion of the particle's trajectory. The effect of momentum loss due to an inelastic collision and rebounding of particles is considered for the Martian atmosphere.

The advancement from a two-dimensional flow to the three-dimensional case significantly complicates the mathematical developments of the problem. The equations of motion of the particle become more difficult, but with the usage of high

speed computers can be solved numerically to sufficient degrees of accuracy. Once the equations are developed any type particle flow problem can be solved accurately if the flow field is known. Even with just basic characteristics of the flow field known an approximate solution of particles can be obtained.

The effect of turbulence (for Earth) on the particle's trajectories was modeled empirically by a cyclic fluctuating vertical velocity component and found to be of minor influence. The effect of turbulence on the Mars trajectories was not accounted for after an analysis of its effect on Earth; calculation showed only a 4% or less altering of its trajectories for a particle of 100 microns diameter. Also the computing time to obtain a solution with the effect of turbulence included increased by an order of magnitude over the case without turbulence present.

The path of the trajectory for a single particle was calculated for an idealized three-dimensional vortex system superimposed on a turbulent boundary layer flow under Martian surface conditions. Here a combination of the time-averaged velocity distribution and a Rankine vortex was made and particle trajectories were numerically solved under its influence. An empirically developed function was used to simulate the wall effect on the Rankine vortex. The flow was assumed to be symmetric and stable around the model crater.

Several solutions of the particle's motion were calculated, each having a different relative position with respect to the vortex core. Two cases were calculated for the vortex motion, one of which was for a particle diameter of 100 microns and the other for a 500 micron particle. The results of the effect of a Rankine vortex present in a three-dimensional flow field simulating the wake crater flow show increased erosional properties outside of the horseshoe vortex system and also greatly increased particle trajectory heights. Also, smaller size particle trajectories followed the motion of the vortex flow causing lateral curvature of the particle's trajectory.

II. REVIEW OF LITERATURE

What follows is a basic review of some of the aspects of
the turbulent boundary layer, particle simulation, and crater
modeling. It is not intended to be a complete or comprehensive
compendium of these subjects.

A. Turbulent Atmospheric Boundary Layer

One of the basic features of a turbulent boundary layer
is the turbulence. The most unique feature and the basic
nature of turbulent motion is the fact flow parameters are not
constant with respect to time at a fixed point in space, but
fluctuate randomly through a wide range of frequencies. The
mean temperature and velocity profile are directly affected by
the random fluctuation of temperature and velocity. Turbulent
flow has long been thought of as a three-dimensional flow with
a random distribution of vortical eddies superimposed on the
main flow. The mathematical expression for this was developed
by Reynolds, i.e.,

$$u = \bar{u} + u' \qquad (2.1)$$

$$\bar{u} = \frac{1}{T} \int_{t_0}^{t_0+T} u \, dt \qquad (2.2)$$

where u is the instantaneous velocity, $\bar{u}$ is the time averaged
mean velocity, u' is the instantaneous fluctuating velocity,

t_o is the initial time of the integral time period, and T is a
sufficiently long length of time necessary to make $\bar{u}$ independ-
ent of time. Of course there exist time averaging integrals
for all variable flow quantities. By definition the time
averaged integral of the fluctuating quantities is zero.

The study of the turbulent shear layer has been wide. In
particular the specific study of the turbulent boundary layer
has been conclusive (Monin and Yaglom, 1965 and Lumley and
Panofsky, 1964). From experiments conducted by Nikuradse
(1932, 1933) on flow in rough-walled pipes, Schlichting (1968)
and Sutton (1953) with others discuss the logarithmic wind
profile law. For the case of a neutrally stratified planetary
boundary layer Jensen (1958) and others observed that it also
obeys the logarithmic law, i.e.,

$$\frac{\bar{u}(z)}{u_*} = \frac{1}{k} \log\left(\frac{z}{z_o}\right) \tag{2.3}$$

where $\bar{u}(z)$ is the time averaged velocity which is a function
of height, z; u_* is the friction velocity; k is von Karman's
universal constant; z is the height above the surface; and z_o
denotes the equivalent surface roughness height.

The two-dimensional turbulent boundary layer has been
shown by Clauser (1956) to have a double structure. The
double structured layer consists of an inner (or "surface")
layer and an outer (or "defect") layer. The atmospheric
boundary layer also has a similar type of double structure.

The surface layer is like the two-dimensional inner layer, while the outer layer is three-dimensional in nature. The three dimensionality of the outer layer is caused by a balance of the rotation force of the earth (or planet) and frictional force. The resultant force caused by the rotation is called the Coriolis force. Coriolis force causes the direction of the mean wind in the outer portion of the planetary layer to turn to the right with increasing height (in the northern hemisphere). The three-dimensional turbulent atmospheric boundary layer is also known as an "Ekman Spiral" or "Ekman layer" named after V. W. Ekman (1905) who first discovered the phenomenon and used it in a discussion of wind-generated ocean currents on a rotating earth. The rate of turning with height of the Ekman layer depends on the distribution of eddy viscosity and density.

B. Laboratory Simulation

An important problem in an experimental application of the atmospheric boundary layer is the laboratory simulation by use of wind tunnels. Great insight and understanding of the physical flow can be ascertained if correct similitude parameters are obeyed. A basic review of the criteria of correct model simulation is given here within. The review will be restricted to the lower portion of the turbulent boundary layer which, for the most part, is the most relevant

to the present problem.

In order to properly model the lower portion of the planetary boundary layer in a wind tunnel certain necessary conditions must be met.

Cermak et al. (1966), Hidy (1966), and McVehil et al. (1967) have shown that wind tunnels can model the atmospheric boundary layer. Many have applied the problem of modeling the atmospheric boundary layer by laboratory simulation with some degree of success (Halitsky, 1969; Plate and Ouraishi, 1965; and Cermak, 1963). Arya and Plate (1969) have shown that the Monin and Obukhov (1954) similarity theory offers a good foundation on which to base modeling of a stably stratified atmospheric boundary layer.

In the last fifteen years the study of surface (or inner) layer has been thoroughly extensive. As a result there are a large number of studies that have been conducted. Some good discussions of these are given in Monin and Yaglom (1965), Lumley and Panofsky (1964), and a basic review of the atmospheric layer in Monin (1970).

From the similarity theory of Monin and Obukhov (1954) the surface layer can be modeled if planar homogeneity exists. A detailed review of the implications of homogeneity to the similarity theory is given by Calder (1966).

Exact modeling of the atmospheric layer in detail is not possible. However, by selecting certain similitude parameters

that need not be strictly matched and relaxing these require-
ments, one can obtain good laboratory results for special type
atmospheric flows.

As reported by Cermak (1971) the similarity criteria can
be obtained from the equations of motion for the particular
flow problem by nondimensionalizing the equations. As a
result the nondimensional equations will yield similitude
governing parameters as coefficients of the equations of
motion.

If horizontal and vertical geometry is kept it will result
in an invariant nondimensional transformation of the conserva-
tion of mass[1]

$$u_{i,i} = 0 \quad \text{and} \quad \frac{\partial \rho}{\partial t} + \frac{\partial (\rho u_i)}{\partial x_i} = 0 \tag{2.4}$$

Nondimensionalization of the time averaged momentum
equation yields the criteria for dynamic similarity. The
time averaged momentum equation is

$$\frac{\partial \bar{u}_i}{\partial t} + \bar{u}_j \frac{\partial \bar{u}_i}{\partial x_j} + 2 \, \varepsilon_{ijk} \Omega_j \, \bar{u}_k$$

$$= -\frac{1}{\rho_o} \frac{\partial \bar{p}}{\partial x_i} - \frac{\Delta \bar{T}}{\bar{T}_o} g \delta_{i3} + \nu_o \frac{\partial^2 \bar{u}_i}{\partial x_k \partial x_k} + \frac{\partial (\overline{-u_j u_i})}{\partial x_j} \tag{2.5}$$

---

[1]Cartesian tensor notation and Einstein summation
convention is used.

where the dependent variables are represented by mean (quantity represented by the bar over the variable and fluctuating values. The Boussinesq density approximation is made thus limiting the application of the equation to flows of $\Delta \bar{T} \ll \bar{T}_o$ where $\bar{p}$ is the deviation of pressure from the atmospheric pressure associated with ρ_o. Using,

$$\hat{\bar{u}}_i = \bar{u}_i/u_o \quad ; \quad \hat{u}_i' = u_i'/u_o \quad ; \quad \hat{x}_i = x_i/L_o$$

$$\hat{t} = tu_o/L_o \quad ; \quad \hat{\Omega}_j = \Omega_j/\Omega_o \quad ; \quad \hat{\bar{p}} = \bar{p}/\rho_o u_o^2$$

$$\Delta\hat{\bar{T}} = \Delta\bar{T}/(\Delta\bar{T})_o \quad ; \quad \hat{g} = g/g_o \tag{2.6}$$

to nondimensionalize the momentum equation yields:

$$\frac{\partial \hat{\bar{u}}_i}{\partial \hat{t}} + \hat{\bar{u}}_j \frac{\partial \hat{\bar{u}}_i}{\partial \hat{x}_j} + \left[\frac{L_o\Omega_o}{u_o}\right] 2 \, \varepsilon_{ijk}\hat{\Omega}_j \hat{\bar{u}}_k \tag{2.7}$$

$$= -\frac{\partial \hat{\bar{p}}}{\partial \hat{x}_i} - \left[\frac{\Delta\bar{T}}{\bar{T}_o}\frac{L_o g_o}{u_o^2}\right] \Delta\hat{\bar{T}}\,\hat{g}\,\delta_{i3} + \left[\frac{\nu_o}{u_o L_o}\right]\frac{\partial^2 \hat{\bar{u}}_i}{\partial \hat{x}_k \partial \hat{x}_k} + \frac{\partial (\overline{-\hat{u}_i'\hat{u}_j'})}{\partial \hat{x}_j}$$

Three dimensionless parameters result as coefficients for the nondimensionalization of the momentum equation. In order to maintain proper dynamic similarity the three similitude parameters must be matched. These three parameters are known as

Rossby number; $R_o = u_o/L_o \Omega_o$

bulk Richardson number; $R_i = [(\Delta \bar{T})_o/T_o][L_o g_o/\bar{u}_o^2]$

Reynolds number; $R = u_o L_o/\nu_o$

The time averaged conservation of energy equation is,

$$\frac{\partial \bar{T}}{\partial t} + \bar{u}_i \frac{\partial \bar{T}}{\partial x_i} = \left[\frac{\kappa_o}{\rho_o c_{p_o}}\right] \frac{\partial^2 \bar{T}}{\partial x_k \partial x_k} + \frac{\partial(-\overline{\theta' u_i'})}{\partial x_i} + \frac{\bar{\phi}}{\rho_o c_{p_o}} \qquad (2.8)$$

where ϕ is the dissipation function. Nondimensionalizing as for the momentum equation it becomes

$$\frac{\partial \hat{\bar{T}}}{\partial \hat{t}} + \hat{u}_i \frac{\partial \hat{\bar{T}}}{\partial \hat{x}_i} = \left[\frac{\kappa_o}{\rho_o c_{p_o} \nu_o}\right]\left[\frac{\nu_o}{L_o u_o}\right] \frac{\partial^2 \hat{\bar{T}}}{\partial \hat{x}_k \partial \hat{x}_k} + \frac{\partial(-\overline{\hat{\theta}' \hat{u}_i'})}{\partial \hat{x}_i}$$

$$+ \left[\frac{\nu_o}{u_o L_o}\right]\left[\frac{u_o^2}{c_{p_o}(\Delta \bar{T})_o}\right] + \text{etc.} \qquad (2.9)$$

Here two additional similarity parameters result:

Prandtl number; $P_r = \nu_o \rho_o c_{p_o}/\kappa_o$

Eckert number; $E_c = u_o^2/c_{p_o}(\Delta \bar{T})_o$

If these two parameter criteria are satisfied then thermal similarity exists. For wind tunnel simulation in air the Prandtl number criteria is automatically satisfied and the Eckert number is only important in compressible flow.

For correct simulation of the pressure distribution (on various objects) in the atmospheric layer, in wind tunnel modeling Jensen (1958) observed that the roughness height ratio in the wind tunnel to that of the planetary boundary layer must be equal to a characteristic length of each, i.e.,

$$\frac{z_{o_m}}{z_o} = \frac{L_m}{L} \qquad (2.10)$$

Thus the geometric scaling of the boundary condition must also be satisfied as stated (Jensen, 1958). If the other similitude parameters are also satisfied then dynamic similitude will prevail. A zero pressure gradient criterion in the longitudinal direction must also be satisfied. This can be accomplished by having a flexible ceiling of wind tunnel equipment and adjusting it until the criterion is met. In addition to the above criteria it is also necessary that a natural fully turbulent boundary layer be developed. This is usually accomplished by one of two methods, the first is a long test section in order to develop a boundary layer of the proper temperature distribution and turbulent structure. The second method is the use of turbulent tripping fencing and roughness elements. The latter is not as desirable for the reason that it usually does not obtain the characteristic of a fully turbulent flow because basic flow variables change with distance downstream of the perturbating devices fairly rapidly. For the details of analysis see Cermak (1971) and Plate and Cermak (1963) and

Sundaram et al. (1972).

In addition a few other basic points are pointed out.
The geostrophic wind is not analogous to the free-stream
velocity in the wind tunnel. Wind tunnel studies are only
valid for simulation of the surface layer of the planetary
(or atmospheric) layer. Since this layer is essentially
independent of the geostrophic wind and the Ekman spiral
effect, it can be modelled without matching Rossby numbers.

In order to simulate the entire Ekman layer the Rossby
number criteria would have to be met which would involve a
rotation of some nature of the wind tunnel test section.

For the surface layer Monin and Obukhov (1954) have
developed a theory which uses only variable parameters defined
at the ground surface, i.e., the surface roughness height, z_0
and friction speed, u_*, to entirely describe the layer. The
surface layer extends up to a height of approximately 200 ft.

Effects due to a nonneutral atmosphere (stable or un-
stable) can be simulated to some extent by cooling and heating
the wind tunnel floor and/or ceiling Cermak (1971).

One condition that must be met in order to obtain proper
simulation is that the model flow be fully aerodynamically
rough. This condition can be assured if the friction Reynolds
number is greater than three, i.e.,

$$R_f = \frac{u_* z_0}{\nu} > 3 \qquad (2.11)$$

For a detailed discussion of the limits of the wind·
tunnel applications see Sundarum et al. (1972).

1. <u>Particle</u> <u>trajectories</u>

Very few scaled model experiments of sedimentation
patterns around obstacles in air have been performed. The
satisfying of the Froude number is not as crucial in air as
compared to water, since in air there is no pertinent free
surface. Of the experiments that have been performed most
deal with the accumulation of drifting snow. In one such
study by Strom et al. (1962) the important similitude
parameters were

$$D_p/L_{o_m}, \quad u^2/gD_p, \quad u_F/u, \quad e, \quad u_p/u$$

where L_{o_m} is a characteristic model length, u is the stream
speed at some reference height, D_p is the particle diameter,
u_F is the particles terminal speed, e is the coefficient of
restitution, and u_p is the speed of the snow particle.

Other practical applications of the particle simulation
study is that of the eolian phenomena that exists on Mars.
Dust storms and other eolian activities have been suspected
to occur on Mars on the basis of telescopic observations
(deVaucoulers, 1954; Kuiper, 1957; Rea, 1964; and others) and
theoretical considerations of the Martian surface and
atmosphere (Ryan, 1964; Sagan and Pollack, 1969). <u>Mariner</u> <u>9</u>
results confirm the existence of eolian features on Mars and .

show that eolian processes play a significant role in modifying the Martian surface (Sagan et al., 1973). Many eolian features were observed in various stages of formation as the Martian dust storm of 1971-1972 slowly subsided (Sagan et al., 1972). Analyses of Mariner 9 imagery reveal many features that appear to have resulted from long-term eolian processes (Masursky, 1973). Knowledge of Martian eolian activity as a geologic process is essential to the understanding of the complex surface characteristics and geologic history of the planet. The modeling of the Martian eolian process uniquely lends itself to an investigation of the similitude parameters.

The atmospheric pressure on Mars is much less than Earth, on the order of 5 millibars at the planet's surface. With these facts known, facilities with low pressure capabilities were conjectured to study the eolian phenomena (Bidwell, 1965 and Chang et al., 1968). One such wind tunnel was constructed and low pressure tests were conducted to find threshold speeds at what was believed to be Martian surface pressure (Hertzler, 1966a,b, and Adlon et al., 1969). For Martian threshold determination it is necessary to use extremely low pressure, equivalent to the pressures on Mars, which can only be accomplished in a low density wind tunnel. However, the simulation of eolian processes on the Martian surface can be accomplished by use of an atmospheric wind tunnel provided close attention is paid to satisfying appropriate modeling

parameters and proper simulation of the planetary boundary layer.

Several important parameters of general particle salta-tion, sedimentation process have been found to be (Iversen et al., 1973):

A   Bagnold's coefficient

B   Particle friction Reynolds number

C_L Lift coefficient, $C_L = L/(1/2\rho u^2 S_A)$

C_D Drag coefficient, $C_D = D/(1/2\rho u^2 S_A)$

D   Drag force, (force)

D_c Crater diameter (length)

D_p Particle diameter (length)

e   Coefficient of restitution

g   Acceleration of gravity (length/time^2)

h   Ripple height or reference height (length)

ℓ Length (length)

L   Reference length (length)

ℓ_t Wake length (length)

L*   Monin-Obhokhov Stability length, $L* = u_*^3 \, c_p \rho T/kgH$
       (length) (where c_p is specific heat, T is temperature, H is heat flux at surface)

R   Reynolds number, uL/ν

S_A Reference area (length^2)

t   Time (time)

T   Turbulence factor

u   Velocity (length/time)

u_* Friction velocity, $(= \sqrt{\tau/\rho}$ (length/time)

u_{*t} Threshold friction velocity (length/time)

u_F Terminal velocity (length/time)

u_∞ Free stream velocity (length/time)

u_g Geostrophic wind (above boundary layer)

W Weight (force)

W_s Sample width (length)

x Streamwise distance (length)

y Lateral distance (length)

z Vertical distance (length)

z_0 Roughness length (length)

z_0' Roughness length of saltation (length)

γ Specific gravity

δ Boundary layer thickness (length)

κ von Karman's constant (also C_1).

λ Ripple wave length (length)

μ Absolute viscosity (mass/length-time)

ν Kinematic viscosity (length^2/time)

ρ Mass density of atmosphere (mass/length^3)

ρ_p Particle density (mass/length^3)

τ Shear stress (force/length^2)

These parameters can be arranged to form dimensionless similitude parameters which can be used to overcome some of the difficulties in modeling the full-scale conditions. Several important dimensionless parameters can be formed

e.g. (Iversen et al., 1973),

1. $\rho D_c / \rho_p D_p$. By varying particle density and diameter and the crater diameter, this parameter can be varied from about 0.8 to 3. On Mars, this parameter would vary in value from about 1 for a 100 meter diameter crater to 100 for a 10 kilometer crater.

2. $u(h)/u_F$. Since the threshold friction speed u_* is proportional to the reference velocity $u(h)$, providing geometry (including roughness) is exactly modelled, the ratio of reference velocity $u(h)$ to terminal speed u_F will be modelled exactly if the ratio u_*/u_F is satisfied and if h/L is satisfied.

3. $[u(h)]^2/gL$. The Froude number cannot always be satisfied in the wind tunnel without having a tunnel speed far below threshold speed. It is desirable to make it as small as possible. Again since u_* is proportional to $u(h)$, this is equivalent to requiring a modelling material with as small a threshold speed as possible. The value of this parameter varies from 10 to 150 in the wind tunnel, and from approximately 20 for a 100 meter diameter crater to 0.2 for a 10 kilometer crater.

4. e. The coefficient of restitution is satisfied if model and atmospheric materials have equivalent elastic properties.

5. ℓ/L. Topographic features should be scaled exactly to satisfy this criterion. At large distances upstream from the region of interest, it is probably only necessary to have equivalent scaled aerodynamic roughness.

6. z_0/L. The aerodynamic roughness should, in general, be to scale (Jensen, 1958). Except for those craters surrounded by large-scale ejecta or other rough surface features, this is probably small on Mars. If the corresponding model surface in the wind tunnel is too smooth, it may be necessary to distort this parameter in order to obtain a turbulent boundary layer. It is important at the same time to insure that the ratio h/L be satisfied.

7. z_0'/D_c. If the equivalent roughness height in saltation z_0' is proportional to particle diameter, this parameter obviously cannot be satisfied on the laboratory scale model since such fine particles would have a very high threshold speed. Also, if introduced into the air stream, the particles would go into suspension and the saltation process would not occur. Calculations of saltation trajectory, however, show that the maximum height during saltation would be several times larger on Mars than on Earth, just as the saltation height on Earth is several times as large in air as it is in water. If the equivalent roughness z_0' is proportional to u_F^2/g, then z_0'/D_c is proportional to $\rho_p D_p/\rho D_c$, the inverse of the first

parameter.

8. h/L. The reference height h at which the reference speed is measured should be located within the logarithmic portions of the wind tunnel and atmospheric boundary layers.

9. z_o/L^*. With a "naturally" developed boundary layer in the wind tunnel, a boundary layer velocity profile is achieved which corresponds to a neutrally stratified atmosphere for which the Monin-Obhukov length L^* is infinite and the ratio z_o/L^* is zero. A finite value of L^* is achieved in the wind tunnel by heating or cooling the floor to obtain unstable or stable stratification. Another way of obtaining a nonneutral velocity profile in the wind tunnel (but perhaps not correct modelling of turbulence characteristics) would be by means of shear fences, graded grids, or the like (Counihan, 1969).

10. λ/L. The relative ripple length may be related to z_o'/L and the same comments apply.

11. $u_F u_{*t}$ and 12. $u_{*t} D_p/\nu$. As will be shown above, for a given condition such as for a modelling particle of diameter corresponding to minimum threshold speed, these two parameters would have the same values as for minimum threshold speed material on Mars.

13. u_*/u_{*t}. The manner in which particles are transported and, in particular, the amount of material which is moved

is a function of this ratio. Thus, in order to keep u_* as small as possible because of the Froude number, the threshold friction speed of the particle should be small.

14. $u(h)t/L$. The time scale in the wind tunnel is much shorter than the time necessary for pattern development on Mars since the characteristic time is the ratio of characteristic length L to reference velocity $u(h)$. The time necessary for pattern development on Mars can thus be predicted from wind tunnel tests.

15. A Reynolds number $u(h)L/\nu$ may or may not be an important modelling parameter. For turbulent flows over sharp-edged features, the flow is relatively independent of Reynolds number. The critical model Reynolds number (above which effects are independent of Reynolds number) depends upon model shape. If the model is too stream-lined so that the test Reynolds number is below the critical, the model may have to be distorted by roughening the surface, creating sharper edges, etc. in order to lower the critical Reynolds number. Snyder (1972) quotes critical Reynolds number for sharp-edged cubes of 11,000 and 79,000 for a hemisphere-cylinder. In the current tests, Reynolds numbers based on crater diameter were generally above these values for sharp-rimmed model craters.

In addition to the previously mentioned criteria for similitude analysis further discussions can be found in Strom et al. (1962) and Warnock (1948).

2. Crater modeling

Martian eolian features occur in a variety of forms, most of which are associated with craters or other topographic obstructions. The features are subdivided into two general types: dark streaks and light streaks (Figures 1 and 2). During the Mariner 9 mission, several areas were imaged repetitively in order to observe possible surface changes. Figure 1 shows a crater 17 km in diameter that developed a dark fan-shaped streak within a 38 day period (Sagan et al., 1972); it is typical of many dark features. Figure 2 shows light streaks associated with craters. These and all light streaks imaged repetitively during the mission showed no observable changes. Sagan et al. (1972) concluded that the light streaks are comparatively stable and the dark streaks unstable. Both types of features apparently can be used as surface wind direction indicators and some attempts have been made to derive surface wind patterns from streak orientation (Sagan et al., 1973; Arvidson, 1974).

A special interest case of this dissertation is the study of flow about impact craters under Martian surface conditions, therefore a brief review is in order of the problems
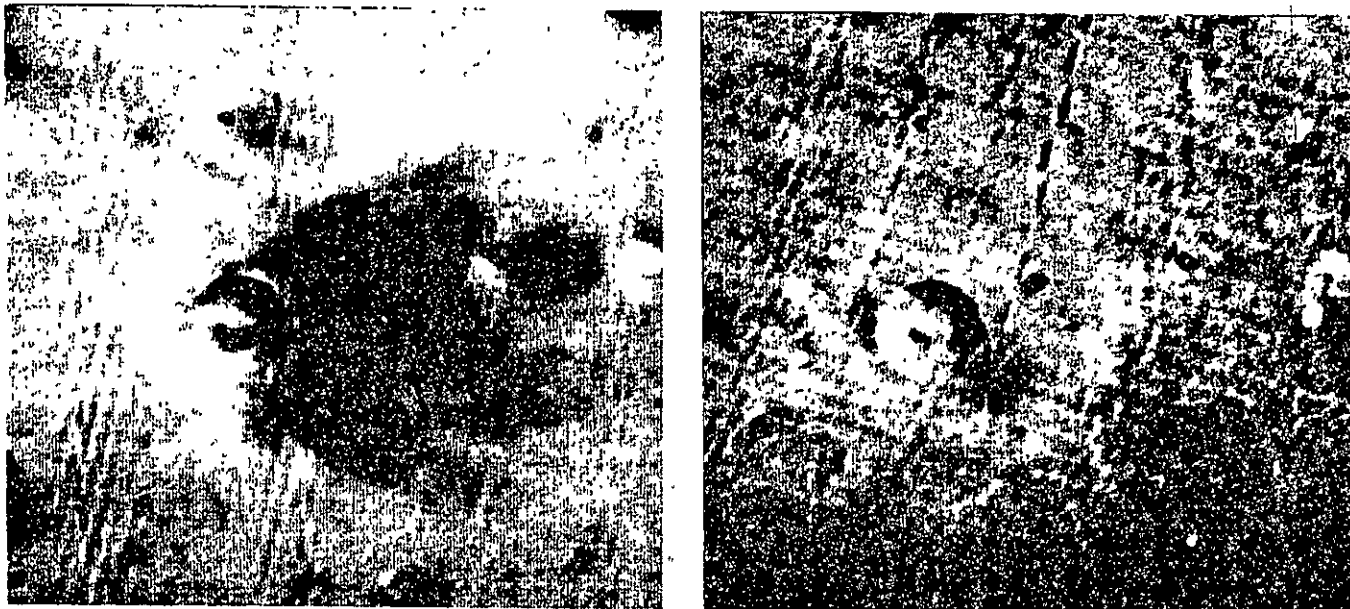
Figure 1.   Crater 17 km in diameter in the Daedalia region near Solis Lacus on Mars, photographed on two revolutions (Rev. 115 on left, Rev. 195 on right). The dark fan-shaped feature developed in a period of 38 days (from Sagan et al., 1972)

Figure 2. Cratered terrain in Hesperia on Mars, photographed on two revolutions (Rev. 128 on left, Rev. 167 on right), showing typical light streaks associated with craters and their apparent stability, compared to dark streaks (Figure 1). Difference in contrast is the result of image processing (from Sagan et al., 1972)

associated with wind tunnel simulation and also with the previous works already performed in the field.

The physical simulation of the movement, deposition and erosion of fine particles upon a complex terrain on a smaller geometric scale presents a complicated problem. The eroding of soil or sand is an intricate function of mean wind speed, frequency and intensity of wind gusts, particle size distribution, density and shape of particles, surface drag forces, and the geometry of the topographic features.

As Bagnold (1941) first reported there exists an optimum particle size that will correspond to a minimum threshold speed. The same universal trend is true for any planetary body. In the case of Mars, Iversen et al. (1973) and Greeley et al. (1973) report that both the optimum particle size and corresponding minimum threshold speeds are higher due to the low atmospheric density on Mars. The terminal speeds are approximately the same for like particles.

The wind pattern over the crater would be similar to wind patterns observed over proturberances in boundary layers with small height to diameter ratios in laboratory scale tests on earth (Sedney, 1973; Gregory and Walker, 1951; and Hunt, 1971). A horsehoe vortex is wrapped around the leading edge of the crater with the trailing vortices emanating downstream from the crater sides. The tangential component of velocity in each trailing vortex is outward away from the wake centerline near

the surface and inward above the vortex cores. The axial velocity components near the surface just behind the downstream crater rim are minimal on the wake centerline with maximum shear stresses occurring on either side of the wake of greater magnitude than outside the wake (see Figure 3). Further downstream the two surface shear maxima merge, and the maximum shear stress in the wake is then on the centerline.

Not all of the similitude parameters can be satisfied simultaneously in a scaled model experiment. In the case of modelling Martian craters the large geometric scaling factors which are necessary in order to properly simulate physical flow conditions cannot be met. The parameter D_p/L cannot be satisfied in normal simulation facilities, e.g., if D_p of a particle is 300 microns and the crater to be modelled is one kilometer, then the parameter D_p/L would be 3×10^{-7}. This would mean that the particle size of a 30 cm model crater would be less than 0.1 of a micron. Obviously such small particles are not suitable since the cohesive and inter-particle forces would result in a relatively high threshold speed that when blown from the surface would go into suspension and therefore would not simulate the saltating phenomenon associated with the eolian process. A further complication that would result in the use of such small particles is that the threshold speed would be too high in order to satisfy other parameters, namely u^2/gD_p. A vertical distortion may then be

FLOW OVER A RAISED RIM CRATER
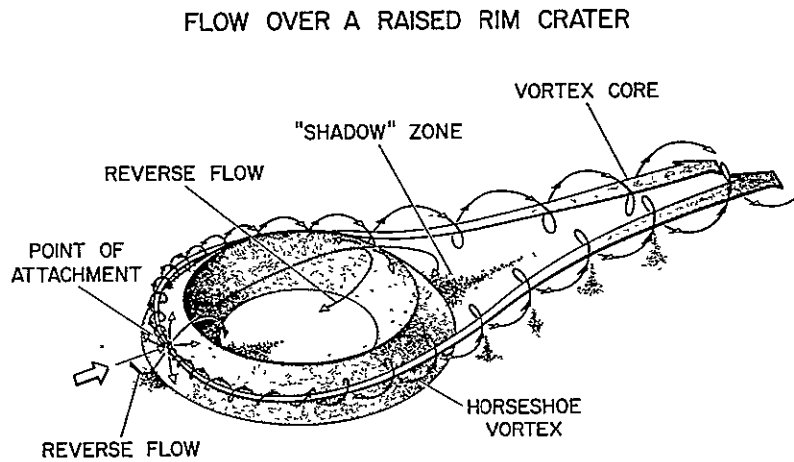
Figure 3. Raised-rim crater, showing horseshoe vortex. Axial
velocity maxima (shown as vortex cores) of the
trailing vortices converge downwind from the crater,
forming a zone of higher surface stress than out-
side the wake, and hence resulting in erosion
(from Greeley et al., 1974)

necessary, as in the case of sedimentation studies in water, to more effectively model the physical situation.

The use of additional aides is necessary in order to determine the most important parameters or combinations of parameters of model simulation since all parameter similitudes cannot be established. One proven method used to gain additional insight into the modelling problem is the nondimensionalization of the governing equations of the flow. Upon doing so several dimensionless parameters are manifested. After basic assumptions applied to the flow problem, the parameters needed to be satisfied to ensure dynamic similarity are (Iversen, 1975b):

$$\frac{R_H}{z'_0}\bigg)_{\substack{\text{wind} \\ \text{tunnel}}} = \frac{R_H}{z'_0}\bigg|_{\text{Mars}} \tag{2.12}$$

$$\frac{x}{D_c}\bigg)_{\substack{\text{wind} \\ \text{tunnel}}} = \frac{x}{D_c}\bigg)_{\text{Mars}} \tag{2.13}$$

$$\frac{C_D \rho D_c}{\rho_p D_p}\bigg)_{\substack{\text{wind} \\ \text{tunnel}}} = \frac{C_D \rho D_c}{\rho_p D_p}\bigg)_{\text{Mars}} \tag{2.14}$$

$$\frac{g D_c^2}{u_*^2 R_H}\bigg)_{\substack{\text{wind} \\ \text{tunnel}}} = \frac{g D_c^2}{u_*^2 R_H}\bigg)_{\text{Mars}} \tag{2.15}$$

The satisfaction of Equation 2.13 is simple as it just requires geometric similarity of topographic and gross erosional and depositional features in the horizontal directions. Small-scale bed-form features such as ripple wavelengths would not be expected to scale without simultaneous satisfaction of all the original modeling parameters.

The satisfaction of the other three similitude parameters is more difficult. Owen (1964) has shown that the equivalent roughness height in saltation is approximately proportional to the ratio of the friction velocity squared to the gravity. Thus Equation 2.12 becomes

$$\frac{R_H}{z_o^!} = \frac{2gR_H}{u_*^2} = \frac{2gR_H}{u_{*t}^2} \left(\frac{u_{*t}}{u_*}\right)^2 \tag{2.16}$$

but considering Bagnold's representation of the threshold friction velocity it becomes

$$\frac{R_H}{z_o^!} = \frac{2}{A^2} \frac{\rho}{\rho_p} \frac{R_H}{D_p} \left(\frac{u_{*t}}{u_*}\right)^2 = \frac{2}{A^2} \left(\frac{u_{*t}}{u_*}\right)^2 \frac{\rho D_c}{\rho_p D_p} \left(\frac{R_H}{D_c}\right) \tag{2.17}$$

Similarly for the Equation 3.15

$$\frac{gD_c^2}{u_*^2 R_H} = \frac{gD_c^2}{u_{*t}^2 R_H} \left(\frac{u_{*t}}{u_*}\right)^2 = \frac{1}{A^2} \left(\frac{u_{*t}}{u_*}\right)^2 \frac{\rho D_c}{\rho_p D_p} \left(\frac{D_c}{R_H}\right) \tag{2.18}$$

Assuming the threshold parameter A is a function only of the particle friction Reynolds number B, the drag coefficient is

$$C_D = \frac{4}{3A^2} \left[\frac{u_{*t}}{u_F} \right]^2 \tag{2.19}$$

The parameter A is constant for larger particles and values of A and C_D for earth and Mars would be approximately equal. This is true even accounting for recent evidence that B is not a unique function of A, even accounting for the rarefied atmospheric effects on Mars (Iversen et al., 1975b). This is not true for small particles. The ratio of terminal to threshold friction speed u_F/u_{*t} is also a function of the particle and the range of values of this quantity on Mars can also be duplicated in the wind tunnel. The ratio of u_*/u_{*t} is varied in the wind tunnel by adjusting the free-stream speed and so can be varied from values slightly below unity to several times unity as is also probably the case on Mars. Thus the groupings of parameters of most interest become

$$\left[\frac{1}{A^2} \left[\frac{u_{*t}}{u_*} \right] \frac{\rho D_c}{\rho_p D_p} \frac{R_H}{D_c} \right]_{\substack{\text{wind} \\ \text{tunnel}}} = \left[\frac{1}{A^2} \left[\frac{u_{*t}}{u_*} \right]^2 \frac{\rho D_c}{\rho_p D_p} \frac{R_H}{D_c} \right]_{\text{Mars}} \tag{2.20}$$

$$\left[\frac{1}{A^2} \left[\frac{u_{*t}}{u_F} \right]^2 \frac{\rho D_c}{\rho_p D_p} \right]_{\substack{\text{wind} \\ \text{tunnel}}} = \left[\frac{1}{A^2} \left[\frac{u_{*t}}{u_F} \right] \frac{\rho D_c}{\rho_p D_p} \right]_{\text{Mars}} \tag{2.21}$$

$$\left[\frac{1}{A^2} \left[\frac{u_{*t}}{u_*} \right]^2 \frac{\rho D_c}{\rho_p D_p} \frac{D_c}{R_H} \right]_{\substack{\text{wind} \\ \text{tunnel}}} = \left[\frac{1}{A} \left[\frac{u_{*t}}{u_*} \right]^2 \frac{\rho D_c}{\rho_p D_p} \frac{D_c}{R_H} \right]_{\text{Mars}} \tag{2.22}$$

The approximate ranges of values of the individual parameters
in the wind tunnel and on Mars are listed in Table 1.

Table 1. Similitude parameter values

Parameter	Mars	Wind tunnel
u_F/u_{*t}	1 to 15	1 to 15
u_*/u_{*t}	0.8 to 2.0	0.8 to 2.0
$\rho D_c/\rho_p D_p$	0.6 to 500	0.1 to 3.0
$1/A^2$	50 to 100	50 to 100

III. THRESHOLD DETERMINATION

With the recent images received from Mariner 9 showing
evidence of eolian processes, new interest was generated in
the conceptual understanding of the determination of static
and dynamic threshold speeds under Martian surface conditions.
This in turn created renewed interest in experimental and
theoretical studies of the threshold phenomena under earth's
atmospheric conditions (Iversen et al., 1973 and Greeley et al.,
1973). On Mars the atmospheric pressure is approximately two
orders of magnitude less than on earth and as a result the
ratio of fluid to particle density on Mars is much less than
earth's. This showed the need for experimental studies of
particles with a greater density than a typical earth-like
particle under earth's atmospheric conditions and ultimately
under Martian surface condition.[1]

A completely analytical development of a threshold theory
is very difficult and is usually amended to a semi-empirical
theory with the aid of empirical constants found by experimen-
tation. The following is a basic review of a recent paper by
Iversen et al. (1975a) in which a combination of theoretical
considerations and pertinent experimental data are combined to

---

[1]A low density atmospheric wind tunnel is presently under
construction at NASA Ames Research Center, California. This
facility would have the capability to duplicate the Martian
atmospheric surface conditions.

develope threshold relations. The final form of threshold expression accounts for both Reynolds number and interparticle force effects.

As reported by Bagnold (1941) there exists an optimum particle size which corresponds to a minimum threshold speed for a constant density material. The relation between the Reynolds friction number B and the threshold friction speed parameter is

$$A = u_{*t} \ / \ \sqrt{\rho_p g D_p / \rho} \qquad (3.1)$$

$$B = u_{*t} D_p / \nu \qquad (3.2)$$

where u_{*t} is the threshold friction speed, ρ_p and ρ are particle and air densities respectively, g is the gravitational acceleration, D_p is the particle diameter; and ν is the kinematic viscosity of the fluid media.

All variation of the parameter A occurs in flow where a laminar sublayer exists. A drastic increase occurs in the value of parameter A when the parameter B is less than one and is decreasing. The experimental data of Bagnold (1941), Chepil (1945, 1959), Zingg (1953), and Iversen et al. (1975a) support this claim. There is a large discrepancy in experimental data for friction Reynolds number less than five. Chepil (1945, 1959) explains the scatter by differences in particle size distribution. For small friction Reynolds

number B (very small particles) the parameter A is a function
not only of parameter B but also of particle size and shape
distributions as well as possibly other factors. Similar data
scatter was experienced by White (1970) in threshold experi-
ments of small particles in liquid.

Another factor is the cohesive properties of very small
particles. The cohesive forces are caused by van der Waals'
(London) forces, electrostatic charges, and forces between
absorbed film (Brown, 1961 and Kitchener, 1961). Particles of
any size, if small enough, cohere on contact even when
thoroughly dry and particularly in a vacuum (Gregg, 1961).
In metals, forces due to electrical interactions are more
important (Kuhn, 1961). The importance of cohesive effects
for small particles was recognized by investigators interested
in the erosive effects on lunar surface dust by lunar lander
rocket engines (Roberts, 1966). Thus data scatter may be
explained by the existence of interparticle forces due to
moisture, electrostatic effects, and other forces of cohesion.

The aerodynamic drag force and moment for a solid sphere
resting on a plane surface and immersed in a uniform shear
flow is calculated to be (Goldman et al., 1967 and O'Neill,
1968)

$$D = 1.7005(6 \ \pi \ \rho \ \nu \ S \ D_p^2/4) \tag{3.3}$$

$$M = 0.944(2 \ \pi \ \rho \ \nu \ D_p^3 \ S/8) \tag{3.4}$$

Saffman (1965, 1968) derived an expression for a transverse force in a simple shear flow for small friction Reynolds number (a first-order correction to the Stokes approximation) which is,

$$L = 6.46 \rho \nu u (D_p^2/4) \sqrt{S/\nu} \tag{3.6}$$

For the case of the flow in the laminar sublayer $u = u_*^2 z/\nu$ and assuming the center of the solid sphere to be at a distance of $z = D_p/2$ above the surface the transverse force becomes

$$L = 0.8077 \rho u_*^2 D_p^2 (u_* D_p/\nu) \tag{3.7}$$

Equating moments at threshold conditions about the down-stream point(s) of contact yields the friction threshold speed, however the moments due to drag, lift, weight, and interparticle force cannot be determined since they depend on the geometry of the sphere in relation to the surface of particles.

At threshold the moments acting on the sphere are zero, thus equating these (lift, drag, weight, overturning moment, and interparticle force) and solving for the friction threshold speed results in

$$u_{*t} = A_1 \sqrt{\frac{\rho_p g D_p}{\rho} \left[\frac{1 + A_4 I_p/\rho_p g D_p^3}{1 + A_3 B} \right]} \tag{3.8}$$

where I_p represents the interparticle force and A_1, A_2, and A_4 are constant coefficients. The coefficients A_1, A_3, and A_4 are unknown because the average geometry of the sphere's position relative to·the surface of particles and fluid force coefficients are not generally known upon which these ·numerical coefficients are determined. An empirical set of numerical· coefficients are calculated by letting the coefficients A_1, A_2, and·A_4 float for the data of Iversen et al. (1975a) and Weinberger and Adlon (1971) and solving for the least squares curve fit yields (Iversen et al., 1975a)

$$u_{*t} = 0.266 \sqrt{\frac{\rho_p g D_p}{\rho} \left[\frac{1 + 0.055/\rho_p g D_p^2}{1 + 2.123B} \right]} \qquad (3.9)$$

This equation is the best curve fit to Iversen's et al. (1975a) data points plus the four low air density data points of Weinberger and Adlon. The forms of the aerodynamic drag, lift and moment·are valid only for small Reynolds numbers ($R = uD_p/\nu \ll 1$ or $B = 0.45$). Equation 3.9 takes into account both Reynolds number and interparticle force effects. The interparticle forces are shown to be important in Iversen et al., 1975a paper.

Pollack et al. (1974) have shown that the corresponding threshold value of geostrophic wind will increase as non-erodible roughness increases up to a certain level and then ·will decrease as nonerodible roughness increases still further.

A very approximate expression has been derived which
included both the effects of nonerodible roughness and inter-
particle force. The expression for threshold friction speed
is (Iversen et al., 1975a

$$u_{*t} = 0.257 \sqrt{\frac{\rho_p g D_p}{\rho} \left[\frac{1 + 0.0314\, D_p^{0.837}/\rho_p g D_p^2}{1+0.221[\log_e(1+D_p/2z_o)]^2} \right]} \qquad (3.10)$$

These equations should be regarded as tentative, however,
until further low-density experimental threshold data are
available.

IV. PROBLEM FORMULATION

The type of flow where a particle is involved with a fluid media is called a two-phase flow system. When several particles are in motion the flow is termed multiphase flow, of which a two-phase flow system is a special case. There are basically three classifications of multiphase flow. The first is gas-particle flow, which has applications in fluidized beds, cosmic dust, nuclear fallout, and metallized propellant rocket flow. The second is gas-liquid drop flow with applications in air pollution studies, gasoline and rocket engines, and many aspects of meteorological studies of the atmosphere. The third is liquid fluid-solid particle flow with applications in studies of water sedimentation, underwater machines analysis, and soil erosion by rivers and rainfall. The problem of interest here is solid particles saltating in air which is one specific case of the gas-solid particle two-phase flow system.

As the flow of a gas over a surface of solid particles is increased from a very slow speed there occurs at a certain speed movement of particles which is caused by the net forces exerted on the particle by the fluid flow. These saltating particles are subject to three major forces, to the weight of the particle which tends to move the particles down toward the surface, a tangential force which maintains a forward motion, and a normal force which is predominant near the surface and

moves the particle up from the surface and is caused by the

pressure distribution on the individual particle's surface.

The normal force is predominant near the surface due to the

existence of strong shear flow between the particle in

motion and the particles forming the surface. These forces

exerted on the particle are resolved into two components, one

parallel to the direction of mean flow, called the drag

(tangential) force and the other normal to the flow, called

the lift (normal) force (Raudkivi, 1967). Particle shape

influences the magnitudes of these forces. The drag force

consists of surface drag (viscous skin friction) and form drag

due to the pressure difference in the front and back of the

particle. The net drag force depends on the position of the

particle when the force is applied and also on the position

which the lift force acts when applied, both of these are

functions of particle porosity, shape, size, and relative

location of the particles (particle geometry). In the follow-

ing analysis the particles are assumed to be solid spherical

particles of constant density.

In addition to the three major forces there are several

forces that are less dominant in this application. These

forces are the interparticle force, the force of the over-

turning moment in shear flow, the Magnus force, the pressure

gradient force, the Basset force, and the apparent mass force,

and also the force resulting from the effect of temperature

gradients in the flow field. Not all the above forces apply directly to the saltation of particles being driven by a planetary boundary layer. It is necessary to examine the nature of each force and judge how much relevance it has to the specific problem of saltating particles.

A. Drag Force and Coefficient

Studies on the force that a fluid exerts upon a sphere in steady motion began with Newton's experiments in 1719. He found the force to be F,

$$F = 0.055\pi D_p^2 \rho (u-u_p)^2 \tag{4.1}$$

where $(u-u_p)$ is a relative velocity, D_p is the diameter of the spherical particles, and ρ is the density of the fluid medium. This relation seems to be fairly accurate for a Reynolds number region from 700 to 20,000 (Gugan et al., 1964), where inertial terms cannot be neglected as they are for Stokes flow in the momentum equation.

Stokes reported in 1850 that for a symmetric flow field with small velocities (Reynolds number less than 1), the dominant force on the sphere for these Reynolds numbers is viscous and the inertial terms in the momentum equation can thus be neglected. The Stokes force is (Lamb, 1932 and Stokes, 1891)

$$F = 3\pi D_p \mu (u-u_p) \qquad (4.2)$$

where μ is the kinematic viscosity of the fluid material.

The drag force is highly dependent upon the Reynolds number. A standard way to manifest the Reynolds number dependence on the drag force is to maintain the same form of the drag force equation for all range of Reynolds numbers. This can be accomplished by introducing a dimensionless parameter called the drag coefficient C_D,

$$C_D = \frac{\text{Drag force}}{\frac{1}{2}\rho \ (u-u_p)^2 S_A} \qquad (4.3)$$

where S_A is a reference. In the case of a spherical particle' the appropriate reference area is S_A,

$$S_A = \pi D_p^2/4 \qquad (4.4)$$

For Newton's experiments C_D is a constant equal to 0.44. For Stokes flow C_D is inversely proportional to the Reynolds number, the constant being 24, i.e.,

$$C_D = 24/R \qquad (4.5)$$

For flow where the Reynolds number exceeds one Stokes results are no longer valid. The reason is that the flow is no longer symmetric about the sphere because of the increased effect of the inertial forces. The resultant flow up to a

Reynolds number of ten has an oscillating effect which is difficult to express analytically. For flows greater than ten boundary layer separation occurs and a stationery ring vortex forms at the rear of the sphere.

Oseen improved Stokes relation by including inertial terms in the flow field behind the sphere. The drag coefficient that results is a series expansion of the Reynolds number multiplied by Stokes relation; i.e.,

$$C_D = \frac{24}{R} \ [1 + \frac{3}{16} R + O(R^2)]$$ (4.6)

This relation is approximately valid for Reynolds numbers up to approximately four. Proudman and Pearson (1957) improved Oseen's relation by matching series expansion of the flow at the surface and away from the sphere. This resulted in additional terms of order Reynolds numbered squared multiplied by logarithm of Reynolds number (Proudman and Pearson, 1957). The region occupied by the vortex moves downstream with an increase in Reynolds number until a Reynolds number of 150 upon which the oscillation of the vortex system begins.

At Reynolds number roughly equal to 500 (in laminar flow) a wake pattern forms behind the sphere. Vortex rings are continually formed and shed from the sphere. This causes a periodic flow field which results in instantaneous unsteady values of the drag force.

At Reynolds number greater than 30,000 the boundary layer
on the spherical particle has changed from laminar to turbu-
lent. The point of separation moves downstream due to the
change from a laminar to turbulent boundary layer, this causes
a large decrease in the separated wake region behind the sphere
which results in a significant drop of the pressure drag force
of the sphere. This change accounts for a drastic reduction
in the value of the drag coefficient. The value of Reynolds
number at which the drastic drag decrease occurs is called the
critical Reynolds number.

Free-stream turbulence affects the value of critical drag
coefficient. Free-stream turbulence causing a lowering of the
value of the critical Reynolds number which causes backward
shifting of the standard C_D vs. Reynolds number curve. This
results in effectively reducing the value of the drag coeffi-
cient in the neighborhood of critical Reynolds number. The
value of the critical Reynolds number was reported by Giedt
(1951) to be dependent on turbulent intensity, characteristic
length of the turbulent motion and the diameter of the spheri-
cal particle. Generally, the drag coefficient is reduced due
to the presence of turbulence and with increasing flow
turbulence the critical Reynolds number continues to decrease.

Since Newton's first experiments on the sphere, many
investigators have experimentally developed the present C_D vs.
Reynolds number curve that is shown in Figure 4 (Schlichting,
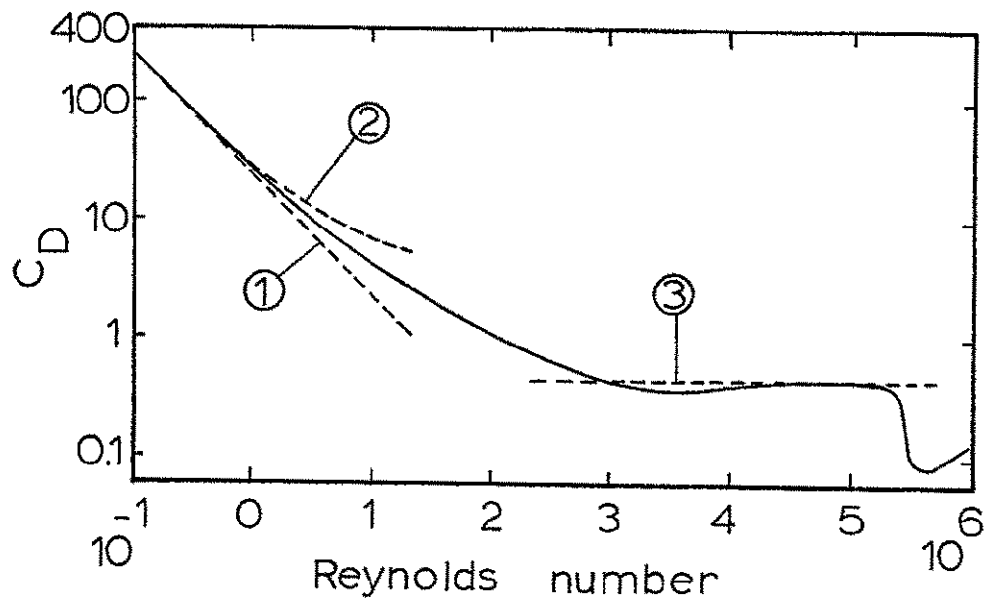
Figure 4. The 'standard' drag coefficient for solid spherical particles as a function of Reynolds number. Curve 1 shows the Stokes theory solution, curve 2 displays the solution to the theory of Oseen, and curve 3 records Newton's estimate of drag coefficient (from Schlichting, 1968)

1968). Also shown in the figure are the early drag coefficient relations of Newton, Stokes, and Oseen. This curve is valid for a single spherical particle moving in a continuum incompressible fluid at constant temperature and velocity. The effect of slip flow caused by rarefaction of the fluid will be covered later. The above description of flow about a spherical particle for various regions of Reynolds number is covered in depth by Soo (1967).

In a recent paper Bailey (1974) points out that many of the measurements of subsonic sphere drag have been affected by the experimental methods used in obtaining the C_D value. His major point, among others, is that in the testing of spheres, if any support device is used it will usually result in a translational oscillation of the sphere which will increase the value of the drag. Thus he offers a revised "standard drag" curve to account for the inaccuracies manifested by the experiments. This revised "standard drag" curve does not seem to be needed in the calculation of saltating particle trajectories due to the fact that the Reynolds number rarely exceeds 300 which is where Bailey's new curve begins to show variation from previous curves.

For ease of computation of the drag coefficient calculation, the method of Morsi and Alexander (1972) has been adapted and full details can be obtained in their paper.

The method Morsi and Alexander used is one where the curve of C_D vs. Reynolds number is empirically fitted (to experimental points) in the form of

$$C_D = \frac{K_1}{R} + \frac{K_2}{R^2} + K_3 \qquad (4.7)$$

The drag curve is broken into seven regions for the entire Reynolds number range. The length of each region is adjusted to negate any discrepancies at the end points. Stokes relation is used for Reynolds numbers less than one-tenth and a constant value of the drag coefficient of 0.4 is assumed for Reynolds numbers greater than 50,000.

The method for obtaining the relationship of the above equation is the same for each region. It has the advantage over numerical techniques due to the fact that there exists an analytical solution for a simplified one-dimensional equation of motion for a particle. If one-dimensional flow is assumed and the drag force is the only force on the particle the simplified equation of motion may be written as

$$m_p \frac{du_p}{dt} = C_D \frac{1}{2} \rho (u-u_p)^2 S_A \qquad (4.8)$$

where m_p is the mass of the particle given by

$$m_p = \frac{\pi}{6} D_p^3 \rho_p \qquad (4.9)$$

The above equation may be rewritten in the form of a Riccati equation, i.e.,

47

$$\frac{du_p}{dt} = \phi_1 - \phi_2 u_p + B_1 u_p^2 \qquad (4.10)$$

where

$$\phi_1 = \frac{3\mu k_1 u}{4\rho_p D_p^2} + \frac{3\mu^2 k_2}{4\rho_p D_p^3} + \frac{3k_3 \rho u^2}{4 D_p \rho_p} \qquad (4.11)$$

$$\phi_2 = \frac{3\mu k_2}{4\rho_p D_p^2} + \frac{3k_3 \rho u}{2\rho_p D_p} \qquad (4.12)$$

$$B_1 = \frac{3k_3 \rho}{4 D_p \rho_p} \qquad (4.13)$$

If u is constant an analytic solution exists, but if u is a variable the equation can be reduced to the Abel form that can only be solved analytically for special type velocity functions.

Morsi and Alexander (1972) show the method for analytic solutions of various cases and go on to solve the constant coefficients k_1, k_2, and k_3 for the seven regions of Reynolds number. In Appendix A the regions and values of the constant are given as found by Morsi and Alexander. The calculated values of C_D are always within 2% of the experimentally found values of C_D.

With knowledge of the characteristics of the drag coefficient the drag force term in the equation of motion may be developed. In a three-dimensional equation the drag force is

$$D = C_D \rho V_r^2 D_p^2 \pi / 8 \qquad (4.14)$$

where $\underline{V}_r$ is the relative velocity vector of the particle

$$\underline{V}_r = \underline{V} - \underline{V}_p \qquad (4.15)$$

where $\underline{V}$ is the stream velocity vector and $\underline{V}_p$ is the particle velocity vector, i.e.,

$$\underline{V} = U \underline{i} + V \underline{j} + W \underline{k} \qquad (4.16)$$

$$\underline{V}_p = U_p \underline{i} + V_p \underline{j} + W_p \underline{k} \qquad (4.17)$$

$$U_p = \dot{x} \qquad (4.17a)$$

$$V_p = \dot{y} \qquad (4.17b)$$

$$W_p = \dot{z} \qquad (4.17c)$$

$$\underline{V}_r = (U - \dot{x}) \underline{i} + (V - \dot{y}) \underline{j} + (W - \dot{z}) \underline{k} \qquad (4.18)$$

and

$$V_r = \sqrt{(U - \dot{x})^2 + (V - \dot{y})^2 + (W - \dot{z})^2} \qquad (4.19)$$

where

$$V_r = |\underline{V}_r| \qquad (4.20)$$

where $|\underline{V}_r|$ is the magnitude of the relative velocity vector.

The drag vector force may be considered as

$$\underline{D} = D_x \underline{i} + D_y \underline{j} + D_z \underline{k} \qquad (4.21)$$

where D_x, D_y, and D_z are the direction components of the drag force. The drag force by definition always acts in the direction of the relative velocity. Considering the situation in a two-dimensional case (omitting lateral motion of the particle) it can be easily seen that (see Figure 5)

$$D_x = \frac{U - \dot{x}}{V_r} D \text{ and } D_y = \frac{V - \dot{y}}{V_r} D \qquad (4.22)$$

where the magnitude of the normalized relative velocity components are $(U - \dot{x})/V_r$, $(V - \dot{y})/V_r$, and in the three-dimensional case $(W - \dot{z})/V_r$; thus the x, y, z components of drag force for the equation of motion are:

x-component: $V_r(U - \dot{x})C_D D_p^2\pi/8$

y-component: $V_r(V - \dot{y})C_D D_p^2\pi/8$

z-component: $V_r(W - \dot{z})C_D D_p^2\pi/8$

B. Effect of Slip Flow on Drag
Force and Coefficient

The Knudsen number is the ratio of the mean free path between molecular collisions to a characteristic length of the flow problem (particle radius). In continuum flow the Knudsen number tends to zero but the Knudsen number increases as the flow becomes rarefied (non-Maxwellian velocity distribution). Slip flow results from the rarefaction of the flow and when the Knudsen number is 0.1 or greater slip flow must be
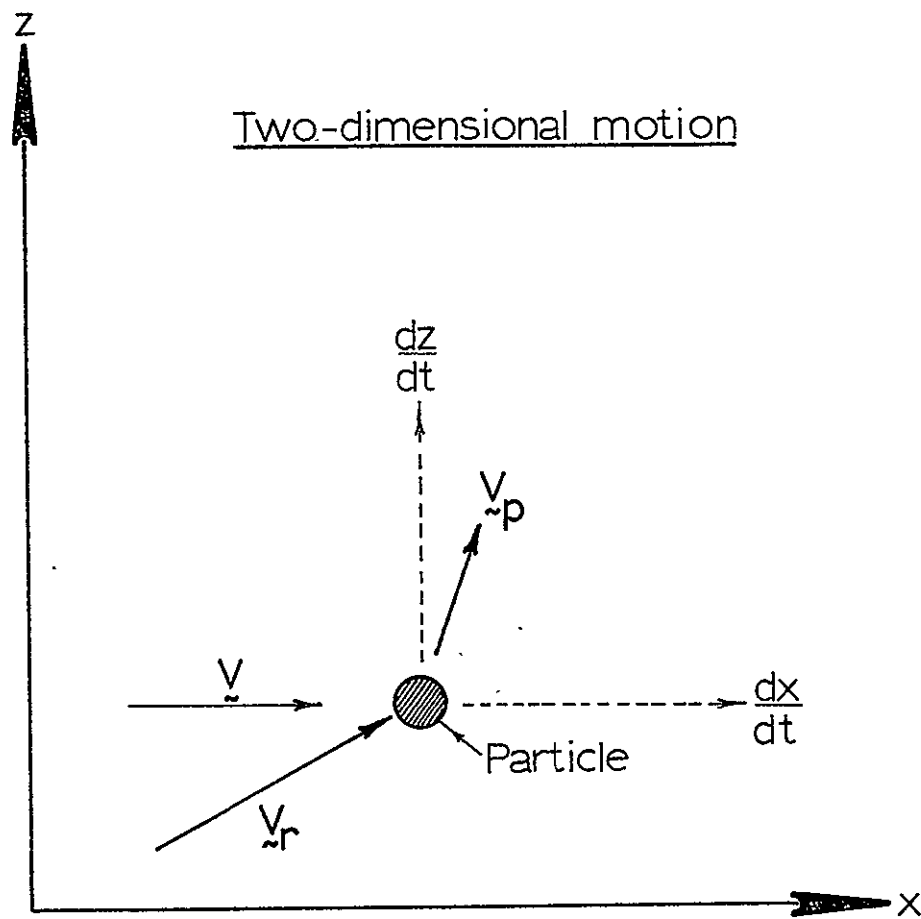
Figure 5. Particle velocities and relative flow velocities

considered in order to keep the calculations valid. In the limit of Knudsen number tending to infinity the flow is called free molecular. The intermediate region is known as transition flow for which very little theoretical work has been accomplished. The continuum and free molecular cases are well understood.

In the derivation of Stokes relation it is always assumed that there is no velocity discontinuity at the sphere's surface (continuum). The relative velocities of the fluid particle next to the surface of the sphere are zero. If there does exist a so-called "velocity slip" or velocity discontinuity at the surface of the sphere then slip flow exists for which Stokes solution is no longer valid. An approximate measure of the magnitude of the discontinuity is the product of the gradient of the velocity and the mean free path length of the gas molecule λ. This discontinuity becomes noticeable either when λ becomes comparable to a characteristic length of the flow problem or when the gradient of the velocity becomes unusually large (as is the case for a shock wave). It is often assumed that the tangential forces acting on the surface of the sphere are proportional to the velocity jump, as described by Fuchs (1964), the resistance of the fluid to the particle is given then by the relation

$$D = 3\pi\mu D_p (u-u_p) \left[\frac{2\eta + D_p\eta_e/2}{3\eta + D_p\eta_e/2} \right] \qquad (4.23)$$

where η_e is the coefficient of external force factor of proportionality. Denoting the ratio η/η_e as β, commonly known as the slip coefficient the equation transforms into

$$D = 6\pi\mu \; \frac{(u-u_p)D_p}{2} \left[\frac{1 + 4\beta/D_p}{1 + 6\beta/D_p} \right] \qquad (4.24)$$

In the limiting case η_e going to infinity the drag force returns to Stokes relation.

Epstein in 1924 developed a rigorous analysis of the tangential velocity at the spheres surface and found

$$\beta = 0.7004 \left[\frac{2}{\alpha} - \lambda \right] \qquad (4.25)$$

where α represents the fraction of gas molecules undergoing diffuse reflection at the surface and $(1 - \alpha)$ the fraction undergoing specular reflection.

For the case $D_p \ll \lambda$ for very small particles or for low pressure conditions the motion of particles can be assumed to be of a molecular nature. If it is assumed that the particle creates no currents and the normal Maxwellian distribution of velocity is unaltered, then the fluid resistance to the particle is a result of a greater momentum flux to the "front" side of the molecule than the "back" side. This is caused by

a greater number of molecules impinging on the front surface. The resistance is proportional to the disturbance in the flow field which is proportional to the particle diameter squared. Then from statistical mechanics (for the mass of particle much greater than the mass of gas) the resistance is expressed as

$$F_m = \frac{\pi}{3} \delta \, \eta_g m_g G_g D_p^2 (u - u_p) \qquad (4.26)$$

where η_g is the number of gas molecules/cm^3, G_g is the molecules mean velocity, $(u - u_p)$ is the relative velocity of the particle, and δ is the factor determined by specular reflection ($\delta = 1$) or diffuse reflection ($\delta = 13/9$) as recorded by Epstein (1924).

Again from statistical mechanics the mean free path is calculated by

$$\lambda = \mu/0.499 \eta_g m_g G_g \qquad (4.27)$$

then the fluid resistance is given by $(D_p \ll \lambda)$

$$F_m = \frac{3\pi\mu D_p^2 (u - u_p)}{2 \, (A + B)} \qquad (4.28)$$

Thus using the form of Equation 4.28 developed by Cunningham (1910) and applying Epstein's relation found in 1924 yields,

$$F_m = \frac{6\pi\mu D_p (u - u_p)}{2(1+A2\lambda/D_p)} \tag{4.29}$$

where $\qquad A = \beta/\lambda \tag{4.30}$

Since $\beta/r = A \dfrac{2\lambda}{D_p}$ is small and A is approximately unity then the above equation only holds for small λ/D_p.

Knudsen and Weber (1911) performed experiments on 0.389 cm radius glass spheres in reduced atmospheric pressure down to 0.14 dynes/cm^2 and developed a form of the slip correction equation for rarefied flow (noncontinuum) and subsequently, most of the later investigators retained the form of their equation, i.e.,

$$X = 1 + \frac{2\lambda}{D_p} [A + B \exp(-cD_p/2\lambda)] \tag{4.31}$$

where X is called the "Correction Factor" somewhat similar to the Cunningham factor. The correction factor divides the drag coefficient to yield the true result. Millikan in 1920 and 1923 published the results of 10 years of experimental work and his values of A and B agreed within 1% of that by Knudsen and Weber. Millikan's experiment involved letting oil drops fall through air. Millikan's data should probably be considered the most reliable. Mattauch (1925) experimented with oil drops in nitrogen and had a region of Knudsen numbers from 0.1 to 5.

All of the above experiments were reviewed in 1945 by
C. N. Davies who developed an average equation of all results.
This lies very close to Millikan's results which are believed
to be the most reliable. Figure 6 shows the comparison of the
correction factor X of Knudsen and Weber, Millikan, Mattauch
and C. N. Davies' averaged curve. The equation of C. N.
Davies is used to calculate the slip flow effect along with
the Chapman-Enskog calculation of mean free path. A compari-
son was made and there was virtually no difference between
Davies equation and Millikan's equations for X. C. N. Davies
equation for X is

$$X = 1 + \frac{2\lambda}{D_p} \; [1.257 + 0.4e^{-2.2D_p/\lambda}] \qquad (4.32)$$

The above equation properly fits the two limits of
$\lambda/D_p \to o$ and $\lambda/D_p \to \infty$.

In the hydrodynamic case of $D_p \gg \lambda$, the equation tends
to that of Cunningham's for flow very near the Stokes region;
and in the molecular case $\lambda \gg D_p$ tends to the free molecule
condition as described by Fuchs (1964).

C. Lift Force and Coefficient

In view of many recent papers the lift force must be
considered one of the pertinent dynamic forces that acts on
small spheres in simple shear flow. For saltating particles
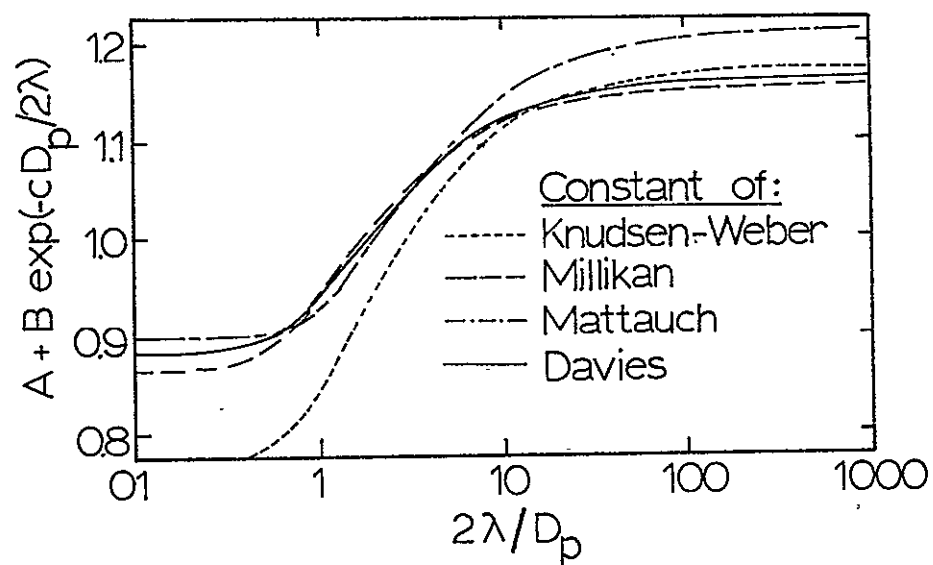
Figure 6. Slip correction for particle motion in gases (from Davies, 1945)

many investigators have shown that the existence of the lift force phenomenon (caused by the shearing flow) is necessary in order to initiate motion of the particles.

Jeffrey in 1929 was one of the first to suggest that a fixed surface particle experienced a lift force caused by an unbalanced pressure distribution on the particles surface. Rubey in 1937 describes the force that moves a particle on a stream bed as the pressure difference between the bottom and top of the sphere among other methods. Then White in 1940 reported that the lift force played a negligibly small role in the movement of particles by wind. This, the author believes was shown to be definitely false by several later papers.

In one of these papers by Einstein and El-Samni (1949) the fluid dynamic forces on individual protusions from a hydraulically rough wall submerged in water were measured.

The purpose of the paper was to study fluid dynamic forces acting upon particles in the surface layer of a sediment bed over which a turbulent fluid flow existed. They measured the average lift force exerted away from the wall on 0.225 feet hemispheres that were glued to the wall in a hexagonal pattern. A lift coefficient could then be calculated as a result of the pressure differences that existed. The lift coefficient was found to have a constant value of 0.178 if based on the velocity that was measured at a height

of 0.55 diameters of the sphere above the wall to which they were glued.

Chepil (1958) performed a series of experiments similar to that of Einstein and El-Samni. It was found that the ratio of lift to drag force on the roughness elements at the surface remained nearly a constant value of 85% for a wide range of hemisphere diameters and friction velocities. A comparison is then made between Einstein and El-Samni's results and Chepil's results under similar conditions. Chepil found an average C_L value of 0.068. He then went on to point out that Einstein and El-Samni's results were based on a pressure difference between the top and bottom of the hemisphere in contrast to his which used a more thorough pressure distribution. Chepil also found that the pressure difference was 2.85 times the lift that the hemisphere experienced, thus applying this correction to Einstein and El-Samni results yielded a C_L of 0.0624. This value is only slightly higher than Chepil's results, who credits the discrepancy to the difference in the geometry of the roughness elements array.

It may be of interest to note that in a recent paper by Willmarth and Enlow (1969) measurements were made on the fluctuating lift force acting on spheres at super-critical Reynolds numbers ($R \simeq 4 \times 10^5$) and a fluctuating lift coefficient of $\sqrt{\overline{C_L^2}} \simeq 0.06$ was found. The value of lift coefficient is nearly equal to Chepil and the modified Einstein and El-Samni measurements, but Willmarth and Enlow's

flow is laminar, while Chepil and Einstein and El-Samni's flow is fully turbulent, but both have relatively high Reynolds numbers.

Chepil (1959) in a later paper goes on to describe the effect of particle shape, particle density, angle of repose of the particle and closeness of packing of many particles as well as the impulses of fluid turbulence of the lift and drag forces experienced by the individual particles.

The discussion of the above material has been restricted to aerodynamically rough surfaces in contrast to a turbulent shear layer with a laminar highly viscous sublayer. The criteria or distinction between the two types of flow was first pointed out by Goldstein in 1938. He developed a friction Reynolds number (formed in the usual way) based on the friction velocity of the shear layer, the particle radius, and the kinematic viscosity of the flow. He cited a critical value of 3.5 below which the laminar sublayer exists and above which the flow is basically turbulent but in the process of transition. Schlichting later reported that this laminar-turbulent transition region exists to a friction Reynolds number of seventy, above which the flow is fully turbulent. Goldstein describes the viscous sublayer as a thin region having a high rate of shear which he believed was caused by the viscous stresses since the apparent Reynolds stress within the layer is small since the turbulent fluctuating velocity

components are negligible or nonexistent. Schlichting (1968) reports the layer as a laminar process where the viscous forces are much larger than the inertia force not allowing any turbulent fluctuations.

Kline (1966) reports the viscous sublayer to be a time-dependent streaky structure that migrates slowly outward from the wall, and highly three-dimensional. Kline accounts for the streaky motion as a result of regions next to each other with relative velocities between them. A fairly regular wave pattern is formed by these streaks in a transverse direction. Kline shows these transverse wave lengths to become shorter for adverse pressure gradients and longer for favorable pressure gradients. Kline et al. (1967) also observes that the unsteady three-dimensional streak flow of the sublayer as well as the turbulent boundary layer will disappear under a sufficiently favorable pressure gradient. This tends to support the claim that the viscous sublayer streaks are a phenomenon due only to the existence of turbulence above the sublayer. Kline's method of investigation was by use of visualization studies of dye and hydrogen bubbles of approxi- mately 0.0005 inch in diameter which were supported by hot-wire anemometer data.

Clark (1968) also conducted hot-wire anemometer tests that supported Kline's results that the sublayer has an active role in the production of turbulence.

Bradshaw (1967) claims that local dissipation of turbulence is more than the local production but this is only true in the viscous sublayer and not true in the remaining inner region where they are equal. He then states that shear stress production is a result of active motion produced in the inner layer. Bull (1967) reports a similar type phenomena in support of Bradshaw's theory.

Tritton (1967) takes an opposing stand that the streaks do not move outward thus causing a favorable effect for turbulent production. He deduces from measurements that the Reynolds stress makes a positive contribution at the wall and for streak flow to move away from or toward the wall would require a negative Reynolds stress contribution. According to Tritton in order to support the streak movement it would take a change in the signs of the correlation coefficient of the axial and transverse velocity fluctuation which he states do not exist in his measurements. He explains that the streaks move away from the wall (in Kline's experiments) because the dye was injected in the stream thus giving them a velocity away from the wall.

Thus, as shown by the opposing view presented, the viscous sublayer has some features that are still ambiguous and not uniformly accepted.

The above discussion of viscous laminar sublayers has presented some of the basic features and nature of a single

phase (same fluid material) flow. With the induction of a single particle in the viscous sublayer the flow now becomes a two-phase system. It is assumed that the presence of the particle does not change the basic characteristic flow field of the viscous sublayer.

In a recent paper Bagnold (1973) reported several important results on the nature of saltation and bed-loading. One of these results was that Francis (1973) had demonstrated that saltating of particles occurs in the absence of fluid turbulence in a laminar flow. This is an important result since in the absence of turbulence there exists no velocity components normal to the surface; thus if saltation occurs it must be predominantly due to the pressure distribution on the surface of the sphere, or a lifting force. Thus Bagnold and Francis have asserted the fact that the initiation of motion upward away from the surface is due to a lift force of the same order of magnitude as the drag force. Of course the existence of the lift force is short-lived as observation confirms the rapid decrease of vertical force.

Saffman (1965) derived an expression for lift on a sphere (computed to $O(R_x^{1/2})$) moving through a simple shear flow and found

$$L = 1.615\mu(u - u_p)D_p^2(S/\nu)^{1/2} \qquad (4.33)$$

where S is the magnitude of the velocity gradient.[1] The above equation has the restriction:

$$R_V \ll R_K^{1/2} \qquad (4.34a)$$

$$R_K \ll 1 \qquad (4.34b)$$

where R_V is the conventional Reynolds number based on sphere radius and relative fluid velocity $(u - u_p)$.

This relation can be utilized to analytically find an expression for the lift coefficient in a simple shear layer. For the case of the laminar sublayer the velocity profile may be written as

$$u = \frac{u_*^2 z}{\nu} \qquad (4.35)$$

and the laminar sublayer height if $z = 10\nu/u_*$, corresponding to a Reynolds friction number of 10 and gas velocity of $u = 10\ u_*$. S is shearing rate,

$$S = \frac{\partial u}{\partial z} = \frac{u_*^2}{\nu} \qquad (4.36)$$

---

[1] In Saffman's original paper the numerical coefficient was a factor of 4π large. This error was pointed out to Saffman as a result of lift calculations and experiments performed by Harper and Chang (1968); Saffman (1968) then re-derived the equations and found an error in the coefficient of 4π.

thus Saffman's lift formula for sphere in simple shear becomes

$$L = 1.615\mu(u - u_p)D_p^2 u_*/\nu \tag{4.37}$$

It is then assumed that the velocity of the particle in the initial stages of lift-off in the laminar sublayer is very small, and it is further assumed that the lift force only acts in the sublayer and possibly to some extent on the upward path of the particle trajectory, but is neglible in the downward part of the trajectory. Thus in the sublayer

$$u - u_p \cong u_*^2 z/\nu \tag{4.38}$$

or the lift is

$$L = 1.615\rho u_*^3 D_p^2 z/\nu \tag{4.39}$$

and the general lift coefficient for a spherical particle is

$$C_L = \frac{8L}{\pi\rho(u - u_p)^2 D_p^2} \tag{4.40}$$

therefore in a laminar sublayer C_L becomes

$$C_L = \frac{12.923}{\pi} \frac{\nu}{u_* z} = \frac{4.114}{R_f} \tag{4.41}$$

Saffman's lift expression can be formed into a general lift coefficient expression for any shear flow as

$$C_L = \frac{4.114\nu^{1/2}}{(u - u_p)} \frac{\partial u}{\partial z} \tag{4.42}$$

and is completely specified when the functional relations of u

and $(u - u_p)$ with z are known, and should be approximately

valid if it obeys the small Reynolds number restriction.

In the case of the aerodynamically rough surface (friction

Reynolds number greater than 3.5), the above expression can be

used with some validity. In the case of the rough surface

there still exists a very high shearing region very close to

the surface. This region of high shear rate is very thin and

is similar to the viscous sublayer with the exception that the

flow is turbulent. If the equation of mean velocity profile

for rough surfaces is substituted in the above general

expression for lift coefficient the result should be valid for

an average lift coefficient as long as the restrictions

$$R_V^2 \ll R_K \ll 1 \tag{4.43}$$

are not exceeded. Of course this represents a very thin

region that exists from the surface roughness height z_0 at

which the average velocity of the flow is zero to some finite

height prescribed by the combination of the shearing rate at

the surface, particle diameter, and kinematic viscosity of the

fluid. The velocity profile for turbulent flow is given by

$$\bar{u}(z) = \frac{u_*}{k} \log_e (z/z_0) \tag{4.44}$$

thus if the relative velocity is again to be assumed very small in comparison with the gas velocity

$$S = \frac{\partial u}{\partial z} = \frac{u_*}{Kz} \qquad (4.45)$$

and the C_L becomes

$$C_L = 3.186/[\log_e(z/z_0) R_f^{1/2}] \qquad (4.46)$$

or letting $z_0 = D_p/30$

$$C_L = 3.186/[\log_e(30z/D_p) R_f^{1/2}] \qquad (4.47)$$

With knowledge of the lift coefficient expression the lift force terms of the equation of motion can be explicitly developed. The lift force is

$$L = C_L \rho \pi D_p^2 V_r^2/8 \qquad (4.48)$$

again where V_r is the magnitude of the relative velocity vector (speed). The lift component of force acting upon the particle is in the positive normal direction of the relative velocity vector. The directional components of the lift force may be found by calculating the cross product of the gas velocity with the relative velocity and then taking that result and forming the cross product with the relative velocity again thus yielding the normal direction of the relative velocity vector in the direction of the lift vector. Then the directional relationship of each component can be found by

normalizing the vector expression to unity:

$$\underline{L} \;\|\; \underline{V}_r \;\times\; (\underline{V}_r \;\times\; \underline{V}) \tag{4.49}$$

where L is the proper lift velocity direction but not the

proper magnitude. Normalizing yields the proper direction and

magnitude of the lift vector:

$$\underline{L} = [L_x \;\underline{i} + L_y \;\underline{j} + L_z \;\underline{k}]L \tag{4.50}$$

where

$$L_x = \frac{[V_{r_y}(UV_{r_y} - VV_{r_x}) - V_{r_z}(WV_{r_x} - UV_{r_z})]}{\Delta L} \tag{4.51}$$

$$L_y = \frac{[V_{r_z}(VV_{r_z} - WV_{r_y}) - V_{r_x}(UV_{r_y} - VV_{r_x})]}{\Delta L} \tag{4.52}$$

$$L_z = \frac{[V_{r_x}(WV_{r_x} - UV_{r_z}) - V_{r_y}(VV_{r_z} - WV_{r_y})]}{\Delta L} \tag{4.53}$$

where

$$\Delta L = \{ [V_{r_y}(UV_{r_y} - VV_{r_x}) - V_{r_z}(WV_{r_x} - UV_{r_z})]^2$$

$$+ [V_{r_z}(VV_{r_z} - WV_{r_y}) - V_{r_x}(UV_{r_y} - VV_{r_x})]^2$$

$$+ [V_{r_x}(WV_{r_x} - UV_{r_z}) - V_{r_y}(VV_{r_z} - WV_{r_y})]^2 \}^{1/2} \tag{4.54}$$

thus components of lift in the three-dimensional equation are

x-component: $L_x C_L \rho V_r^2 D_p^2 \pi/8$

y-component: $L_y C_L \rho V_r^2 D_p^2 \pi/8$

z-component: $L_z C_L \rho V_r^2 D_p^2 \pi/8$

D. The Other Forces

Several other forces act on the particle, few of which
are of the same order of magnitude as the drag and lift forces;
thus by recognizing certain basic underlying assumptions of
the flow these minor forces can be shown to be of negligible
contributions. One force, however, that is of importance is
the potential field that acts on the sphere and in this case
is gravity.

A force of considerable importance in calculation of the
threshold speed at low atmospheric density is the interparticle
force; but once the particle has initiated motion the force is
of negligible effect in the calculation of the particle
trajectory.

The force caused by the overturning moment is, as the
interparticle force, important in the calculation of the
friction threshold speed (Iversen et al., 1975a) as discussed
in the previous section but not relevant to the particle
trajectory motion, and thus is neglected in the calculations.

The velocity gradient in shear flow causes the particle
to rotate. For low Reynolds number this rotation of the

particle causes a viscous interaction of the fluid surrounding the sphere. This is called fluid entrainment which effectively adds velocity to the one side of the sphere where the rotation direction is the same as the fluid velocity direction and retards the fluid velocity on the opposite side. This tends to move the particle in the direction of higher velocity, and is commonly known as the Magnus effect on spinning sphere (Goldstein, 1938). Rubinow and Keller (1961) derived the following relation for the lifting Magnus force on a rotating spherical particle as

$$\underline{L} = \frac{\pi}{8} D_p^3 \, \rho \, (\underline{\omega} \times (\underline{V} - \underline{V}_p)) [1 + O(R)] \qquad (4.55)$$

where $\underline{\omega}$ is the angular velocity vector of the rotating sphere; and the torque on the sphere as

$$L_t = -\pi \rho D_p^3 \, \underline{\omega} [1 + O(R)] \qquad (4.56)$$

which yields the equations of motion for the Magnus effect as

$$\frac{\pi}{6} \, \rho D_p^3 \, \frac{d(\underline{V}_r)}{dt} = -3\pi\mu D_p \, [1 + \frac{3}{8}R]\underline{V}_r + \frac{\pi}{8} \, D_p^3 \, \rho \, (\underline{\omega} \times \underline{V}_r) \qquad (4.57)$$

$$I \, \frac{d\underline{\omega}}{dt} = -\pi\mu D_p^3 \, \underline{\omega} \qquad (4.58)$$

where I is the moment of inertia of the sphere. At high Reynolds numbers the separation point is shifted by the rotation of the sphere, this causes a force in the opposite direction as reported by Hoglund in 1962. This force results

for the particles whose diameter is smaller than the character-
istic length of turbulent eddies or the thickness of a shear
layer (Soo and Tien, 1960).

The Magnus lift force is shown for a freely rotating
sphere $\omega = \frac{1}{2} \cdot \frac{du}{dy}$ by Saffman to be an order of magnitude less
than that caused by the lift force (resulting from shear flow
without particle rotation) unless the rotation speed is very
much greater than the rate of shear. In the case of saltating
particles that are initially at rest it is physically unlikely
that they would reach rotation rates very much greater than
the high shear rates of the lower most portion of a turbulent
boundary layer whether or not a laminar sublayer exists. Thus
in the trajectory calculations of spherical particle the
effect of the Magnus phenomenon has been neglected.

Another term is the apparent mass associated with a
sphere moving through a fluid. The fluid medium exerts a
resistance against this co-called "apparent mass" as well as
the sphere itself. The apparent mass of a body of revolution
may be expressed as

$$m_a = K' \, \pi R^3 \rho \qquad (4.59)$$

where R is the radius of revolution and K' is a constant
determined by the shape of the body, in the case of a solid
sphere $K' = 2/3$. Thus the force for a mass constant sphere is
given (of negligible magnitude in this case)

$$F_{am} = m_a \frac{dV_r}{dt} = \frac{\pi}{12} D_p^3 \rho \frac{dV_r}{dt} \qquad (4.60)$$

Next the pressure gradient force is considered. The pressure gradient $\partial p/\partial r$ is shown in Figure 7 for a particle of diameter D_p then

$$dF_{pg} = -\frac{D_p}{2} \cos\theta \left(\frac{\partial p}{\partial r}\right) \cdot \pi D_p \sin\theta \frac{D_p}{2} d\theta \cos\theta \qquad (4.61)$$

or

$$F_{pg} = -\frac{\partial p}{\partial r} \frac{\pi D_p^3}{4} \int_0^\pi \cos^2\theta \sin\theta \, d\theta \qquad (4.62)$$

The pressure gradient force after integration is

$$F_{pg} = \frac{-\partial p}{\partial r} \frac{4\pi D_p^3}{24} \qquad (4.63)$$

where p is the pressure (a scalar quantity) and r is the position vector of the particle. In the case of the planetary boundary layer it is assumed that planar homogeneity exists as well as a constant pressure with height through the inner layer of the boundary layer, therefore the pressure gradient force need not be considered.

The Basset (1961) force accounts for the effects of the deviation in the flow pattern from steady state, or constitutes an instantaneous flow resistance of the particle. It was derived by Basset in 1892 as
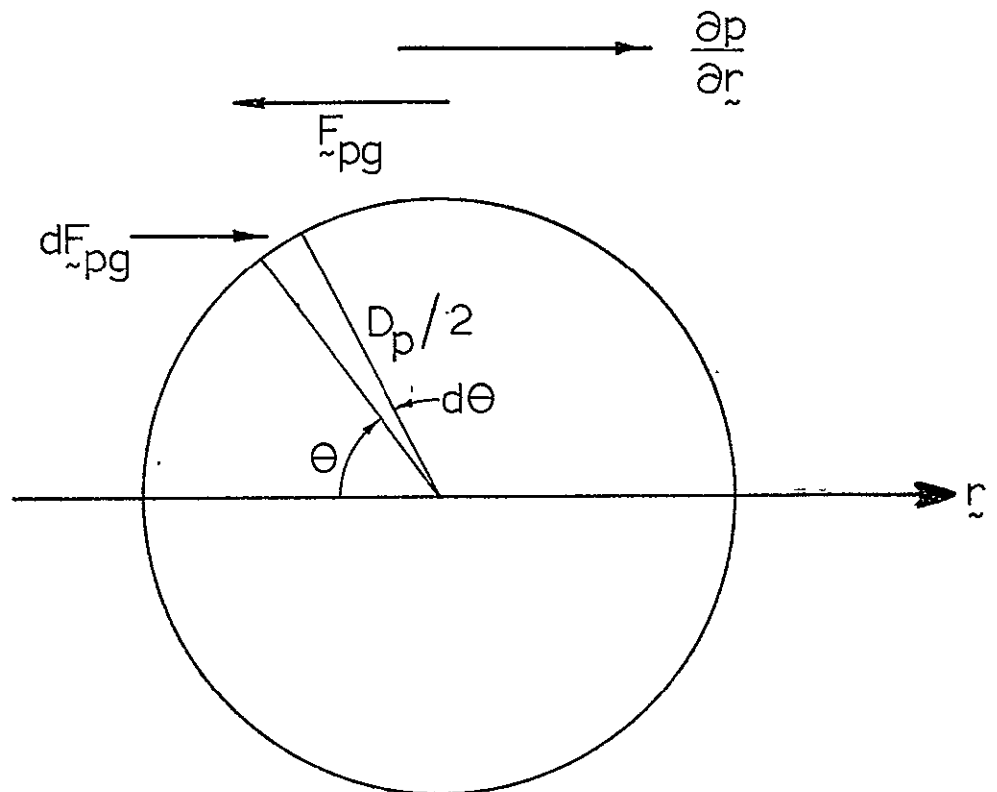
Figure 7.   Force on a sphere due to a pressure gradient
            (from Soo, 1967)

$$F_B = \frac{3}{2} D_p^2 \sqrt{\pi\rho\mu} \int_{t_o}^{t} \cdot \frac{\frac{dV_r}{d\tau} \, d\tau}{\sqrt{t-\tau}} \tag{4.64}$$

where t_o is the initial time when particle motion is considered and t is the final and instantaneous time. When the solid particle is accelerated at a high rate the Basset term becomes substantial as the observed drag force becomes several times the steady state drag force and the drag coefficient increases drastically.

The force terms caused by the pressure gradient effect, apparent mass, and the Basset force are prevalent only if the density of the fluid is equivalent to or greater than the density of the particle. In normal application of saltating motion in the earth's and Martian atmospheres these effects are small in comparison to that of lift, drag, and gravity and thus are neglected.

The effect of the temperature gradient need not be considered when the assumption of a constant temperature throughout the turbulent boundary layer has been made and it is assumed here. It is also assumed that no concentration gradients or radiation gradients exist.

In Appendix B the resultant equations of motion are given for the two-dimensional and three-dimensional cases as well as the nondimensional equations for particle trajectory motion.

V. FLOW AROUND A CRATER

The experimental determination of a three-dimensional turbulent boundary layer (shear) flow field in the presence of a perturbation element is one of the most formidable problems in current fluid mechanics research. The development of an analytical theory is also quite difficult since the effects of the strong viscous interaction in the neighborhood of the perturbation must be accounted for in three dimensions. Consequently there has been little progress in either the theoretical development or the experimental investigation.

A. Characteristics of the Flow Field

The flow around an idealized impact crater may be considered to be a good example of the above situation. Basically there are two types of disturbances that exist in the flow field. One is with the presence of a so-called "large scale" disturbance element which is typically of a larger scale than the boundary layer height and the second is a "small scale" disturbance element. In the case of the "small scale", the disturbance of the flow field is contained within the boundary layer. The main difference between the large protuberance and a small one (relative to the boundary layer thickness) is that the small scale disturbance has only a local effect on the pressure gradient. In this case of flow

over a crater the disturbance may be considered small scale,
and thus as Sedney (1973) describes the flow problem, in two
parts, one in the immediate protuberance neighborhood and the
other in the flow downstream.

In order to have a good conceptual understanding of
three-dimensionally disturbed flows there are several common
characteristics to all flows whether or not the boundary
layer is laminar or turbulent and regardless of the dimensions
or geometry of the protuberance element and speed of the flow.
In most cases the law of the wall for a boundary layer flow
will break in the vicinity of the protuberance, but later
downstream the laws will be valid when the effects of the
disturbance have diminished. In the region of the disturbance
the flow will experience streamwise vorticity (crossflow).
Immediately upstream of the disturbing element one or more
vortices are induced. The primary vortex then stretches
around the front of the disturbance (crater) and is termed a
horseshoe-shaped vortex. The horseshoe vortex can be traced
back to the secondary flow in the boundary layer upstream of
the disturbance. A secondary set of vortices in an opposite
sense of the primary pair is believed to exist on the outer
side of the axial centerline next to the primary set. Another
set of vorticies exists right behind the disturbing element
that are closely spaced vortex filaments originating from
spiral filaments which rise vertically behind the element.

The height of the filaments is approximately the same height as the disturbance element, but in contrast the horseshoe vortex is located closer to the surface. The sense of rotation of the horseshoe vortex is clockwise as looking downstream from in front (upstream) of the element at the left hand side vortex which extends axially downstream. Gregory and Walker (1956) were the first to explore this type of phenomenon. These vorticies affect the velocity profiles of the flow by a redistribution of the momentum immediately downstream of the element. The spanwise velocity profile in such cases was studied by both Tani et al. (1962) and Gregory and Walker. In the protuberance situation of three-dimensional flow in a boundary layer, vorticity stretching, concentration of vorticity upstream and downstream, and viscous effects must all be considered. Figure 3 displays a drawing of a horseshoe vortex system around an idealized crater model (Greeley, 1974).

Tani (1968) reports on examples of sudden perturbations given to a turbulent boundary layer such as roughness elements, suction, or injections. He concludes that recovery to equilibrium is very rapid near the wall but rather slow in the outer region of the boundary layer.

Although data are very limited on three-dimensional flow around a disturbance there are some experimental results available that support the existence of the vortex systems. From the work of A. Hiderks, Prandtl (1952) presents pictures

of flow around a disturbance exhibiting the horseshoe vortex and two symmetrical spirals immediately downstream of the disturbance. Benson (1966) also pictorially shows the vortex system's existence for a hemispherical protuberance element.

In conclusion to the brief introduction of flow about a disturbance it can be said that the resulting flow fields are complex but exhibit characteristic vortex patterns that are not unique to the flow conditions but are widely observed for many different flows. A very perceptive statement is found in Sedney's (1973) paper, "The three-dimensional perturbations found in experimental results are so complex in the neighborhood of the protuberance that it is unlikely that an analysis can be developed that is capable of describing that part of the flow field. There is hope that progress can be made towards analyzing the downstream flow field".

This statement is found to be true by the present author from experimental investigations of flow around an idealized crater model.

B. Experimental Results

The main object of the experimental investigation of the three-dimensional flow field was to gain insight into the basic nature of the complex flow. A total description of the flow field was not sought but rather an in-depth study of the velocity distribution of the downstream flow for the reasons

WIND TUNNEL MODEL CRATER
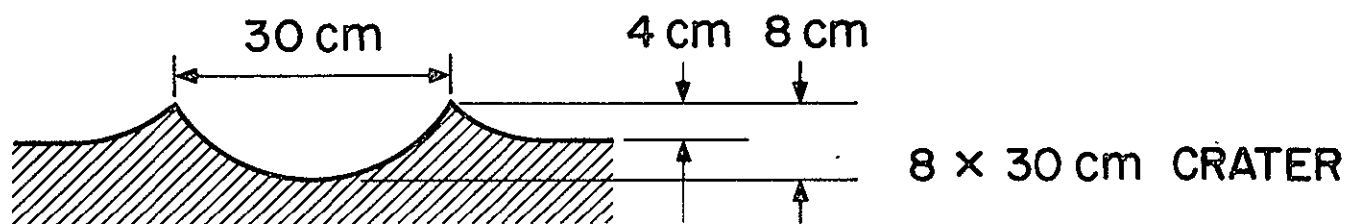
Figure 8. Wind tunnel model crater

mentioned above by Sedney (1973). With a complete knowledge of the downstream flow conditions a conceptual analysis of the intricate flow field is more readily obtainable.

Two series of wind tunnel tests were performed in Iowa State University's wind tunnel. The tests were conducted in an open-circuit environmental wind tunnel which has an adjustable ceiling in order to establish a zero pressure gradient. The test section is 6.5 meters long with a 1.5 square meter test section.

The idealized model of the impact crater is shown in Figure 8. The model crater has a rim diameter of 30 cm and a surface to rim height of 4 cm. The height from the deepest point inside the crater (the center) to the rim is 8 cm. The overall diameter of the model crater configuration is 50 cm.

The model crater was mounted on the axial centerline of the floor surface approximately 5 meters downstream from the entrance of the test section. This enabled the flow to develop as a naturally fully turbulent boundary layer in which the model was immersed.

1. Pitot probe experiments

The first series of experiments conducted used a vertical airfoiled-shaped probe. Pitot probes were secured in the center of the transverse width of the metal airfoil, thus aligning the axial direction of the probes with the freestream flow direction. This insured an exact measurement of the

axial component of the pressure distribution in the crater

flow field. The probes were mounted on the airfoil to given

equal values of the differences of the logarithm of the height

above the surface for any two consecutive probes. This spaced

technique is known as equal logarithmic spacing and is con-

venient since the pressure and velocity profiles generally

follow the logarithmic laws as earlier mentioned. This

convenience manifests itself by displaying equal spacing in a

semi-logarithmic plot of a height versus speed curve which

will be used later.

The vertical airfoil probe was then secured to a cross

bar made of metal. This crossbar was mounted approximately

one foot from the ceiling (so as not to disturb the flow on

the floor below) on two metal grooved racks. The horizontal

crossbar could then be moved in an axial direction. The

vertical airfoil probes could be moved in the transverse

direction. There were 24 pitot probes mounted in the vertical

airfoil ranging from a minimum height above the floor's

surface of 0.160 inches to a maximum height of 35.8 inches

above the surface as shown in Table 2. This enabled the pitot

probe system to measure the flow field three-dimensionally at

any axial or transverse position and at 24 different height

locations; the majority being close to the floor's surface

because of the logarithmic spacing of the individual probes.

Table 2. Experimental pitot probe locations

Position	Height (in.)	Log height
1	0.160	-1.83243
2	0.261	-1.58876
3	0.332	-1.10140
4	0.424	-0.85773
5	0.541	-0.61405
6	0.690	-0.37037
7	0.881	-0.12670
8	1.124	0.11698
9	1.434	0.36067
10	1.830	0.60433
11	2.335	0.84801
12	2.979	1.09169
13	3.801	1.33536
14	4.850	1.57904
15	5.635	1.72900
16	6.945	1.93802
17	8.550	2.14593
18	10.53	2.35423
19	12.915	2.55839
20	15.860	2.76380
21	19.440	2.96733
22	23.830	3.17095
23	29.210	3.37451
24	35.790	3.57767

The pitot probes were approximately 5 cm long with an outside diameter of 1 mm and an inside diameter of 0.75 mm. The pressure tubes that were attached to the rear of the pitot tubes were polyurethane plastic tubing with an outside diameter of 2 mm and an inside diameter of 1 mm. The plastic tubing was carefully secured over the back end of the pitot tubes and then nearly laid against the side of the vertical airfoil section and secured then by fiberglass tape so not to disturb the flow field any more than was necessary. The plastic pressure tubes were run along the vertical probe to the horizontal crossbar and over to the metal grooved track along the side of the wind tunnel. They were then run through a hole in the surface of the adjustable wind tunnel ceiling. The hole was then patched with plastic wood to reduce any adverse effect on the wind tunnel flow. The tubes were then extended to a twenty-six port manometer board. Twenty-four ports were secured to the plastic pressure tubing and one port to a static port that was mounted in the wind tunnel in the vicinity in which the pressure measurements were to be made. The other port was left open to the atmosphere as a reference position. The maximum length of the movable fluid in the manometer board during the testing was approximately 60 cm. The manometer board tubes were made from 1/4 inch diameter glass tubes with an inside diameter of approximately 5/32 of an inch. The manometer board was inclined from the horizontal

upwards at an angle of five degrees. The fluid in the mano-
meter board was water of a special solution to retain good
meniscus shape.

All tests were conducted at an air speed of 75 ft/sec
with an average deviation of ±2-3 ft/sec caused by different
atmospheric conditions. The vertical probe was positioned in
477 different locations where 24 different vertical height
pressure readings were taken. A rectangular two-dimensional
grid network was formed for one side of the axial centerline
assuming the flow around the crater was symmetric. The
measurements began at a position of ten inches axially down-
stream on the centerline from the center of the crater model
and extended downstream 12 inches giving 13 grid points with
equal spacing of one inch. The measurements made in the
transverse direction started at the axial centerline and
extended outward 17.5 inches giving 36 grid points of equal
spacing between points of 1/2 inch. In addition there were
nine separate measurements made on the transverse centerline
starting at a distance of ten inches out from the center of
the crater and extending to 13.5 inches out, again having
equal spacing between grid network points of 1/2 inch. Thus
the total number of two-dimensional probe locations was 477
yielding 11,448 individual pressure points in the flow field.
The majority of these measurements were made downstream of the
crater model.

The method of data reduction was to photograph the manometer board during the test and later to reduce the data from slides made of the photographs. This is believed to be the most valid method of data reduction since it captures the instantaneous location of all the meniscus positions and thus eliminates atmospheric and turbulent fluctuations that would occur if the measurements of all 24 probes were taken individually while the test was being conducted. Most of the fluctuation amplitude was damped by the long length of pressure probe lines. The manometer board was not photographed for each location until certain equilibrium was obtained among the meniscus tubes. The minimum time for this to occur was nearly five minutes but photographs were not taken until eight minutes to insure that equilibrium of the pressure tubes had been reached.

The reduced data were normalized with respect to freestream to eliminate minor fluctuations caused by changing levels of turbulence in the atmosphere and minor variations of the freestream velocity. The data appear to be well behaved from this simple process. Thus all quantities (pressure, velocity, etc.) were equal to unity at freestream conditions and the mean velocity is zero at the floor's surface.

The data obtained from the measurements were programmed on Iowa State University's IBM 360/67 computer which has a simplotter graphics device capable of three-dimensional plots,

constant, line contour plots and two-dimensional plots. All 477 two-dimensional surface grid network points were plotted (height vs. velocity) from the 23 individual height pressure measurements associated with each position.

Figure 9 displays the coordinate system that will be used in reference to the model crater and later in the numerical study. The coordinate system used for the model crater is right-handed orthogonal with the height above the floor's surface as the positive z direction. The positive y coordinate is in the downstream axial direction. The positive x coordinate is in the transverse (lateral) direction. The origin of the coordinate system is located on the vertical centerline of the crater at a height of 4 cm above the crater's floor at the mean level of the wind tunnel floor.

Figure 10 shows a plot of the height z in inches above the surface vs. the dimensionless magnitude of the axial velocity component V (normalized by freestream speed). Four different experimental sets of data are displayed as well as the experimental curve of the undisturbed two-dimensional velocity profile for the turbulent boundary layer. The experimental undisturbed boundary layer thickness δ was found to be 3.5 in. The model crater extended 45% into the undisturbed turbulent boundary layer. The four sets of data are individually taken along the constant position of y = 10 in. (immediately downstream of the crater) for x = 0,3,6, and 9.

Top view

Side view
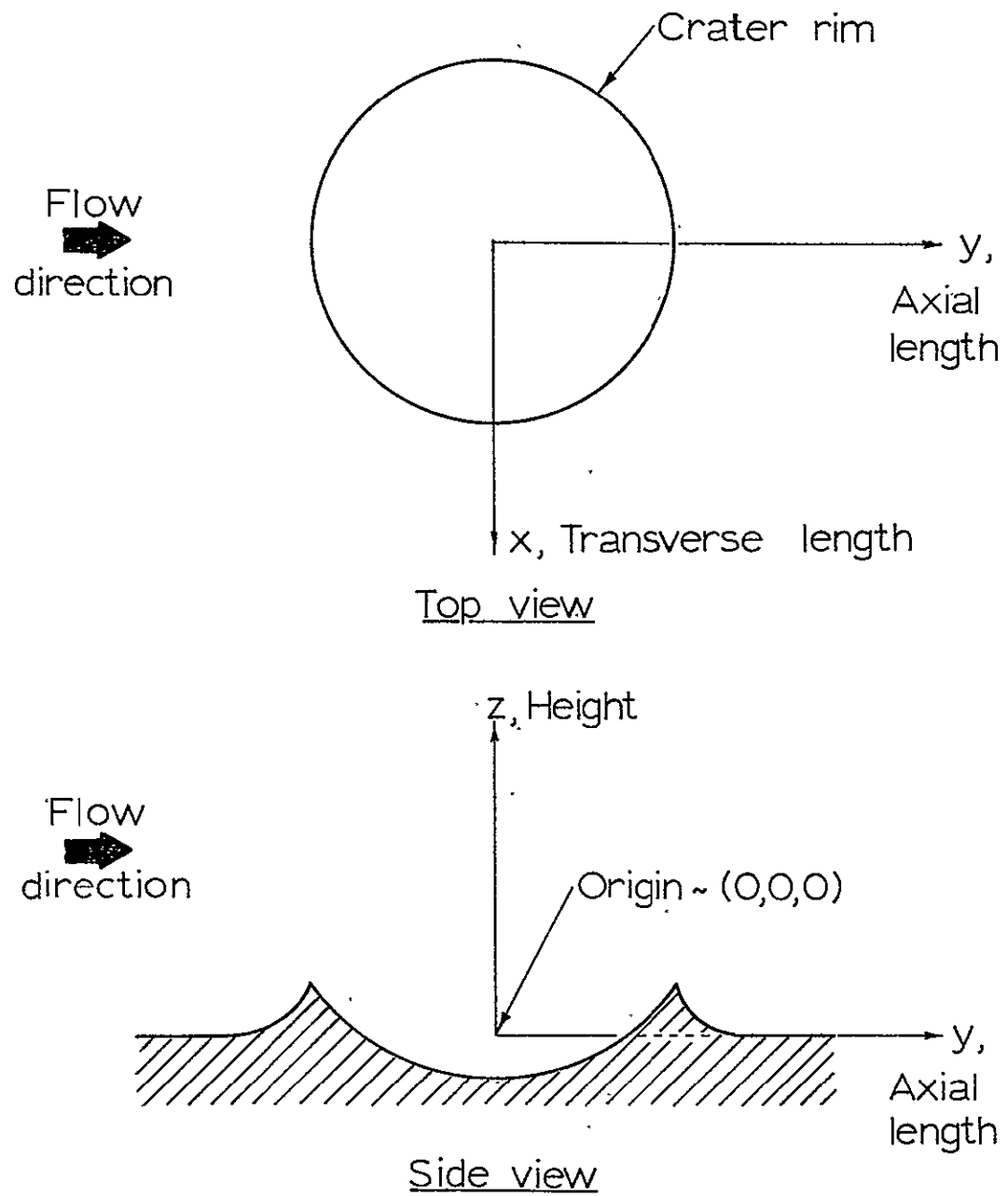
Figure 9. Model crater coordinate system

C-2
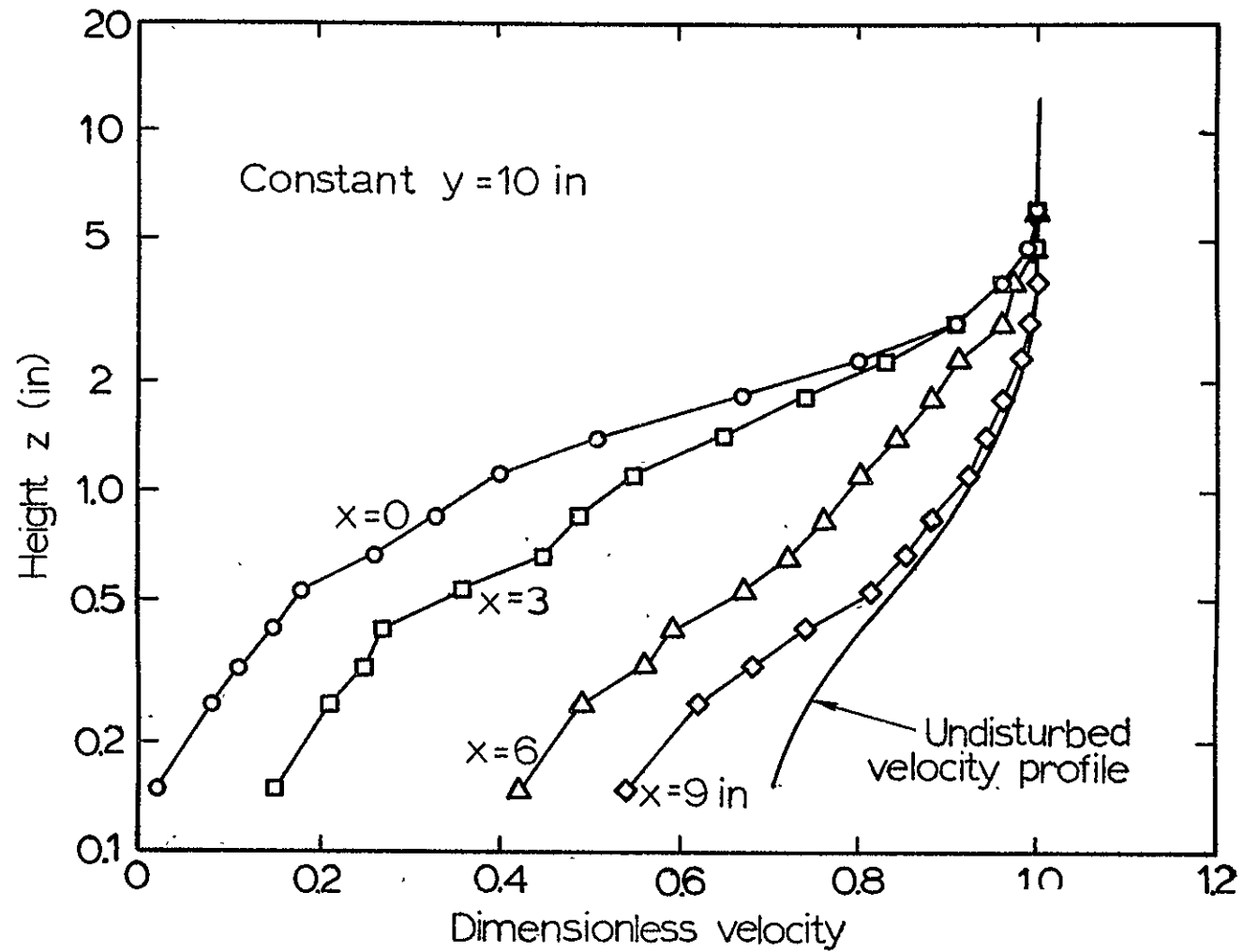
Figure 10. Crater wake vertical velocity profiles for y = 10 in.

in.   At the position x = 0 in. there is an unusually large velocity defect, almost one, very near the surface. There is a rapid increase in velocity with increase in height. At the lower end of the data points there appears to be a linear relation to log z with the dimensionless velocity and there also appears to be a similar relation for the large values of height and velocity. This is contrary to the single slope prediction of the undisturbed turbulent boundary layer. The slope of the linear line is equal to $0.4/u_*$ from which the shear stress τ can be deduced for the case of a zero pressure gradient. For the x = 0 curve this relation would not seem to be valid since it would have two slopes to choose from. This bi-linear relation also shows the possible nonequilibrium effect of the axial pressure gradient which would also violate the relation.

As the x position is increased the velocity profile slowly approaches the shape of the undisturbed flow. As the downstream coordinate y is increased for similar plots the velocity defect becomes smaller and the undisturbed velocity profile is approached more rapidly with increasing transverse distance from the wake centerline. A very rapid acceleration of the flow occurs over a relatively short distance. At a value of x = 12 in. only 2 inches further downstream, the value of the dimensionless velocity at z = 0.15 in. has increased from 0.024 to 0.52. As the distance downstream is

increased the velocity profile off of the wake centerline has a gradual transition from the characteristic turbulent boundary layer profile to a general type wake velocity profile and then returns to the undisturbed profile far downstream.

Figure 11 displays the height vs. dimensionless time for the case of a constant value of $x = 0$ in. for four different downstream positions, $y = 10$, 11, 12, and 20 in. Along the axial centerline the axial component of velocity increases very rapidly with downstream distance near the surface. This is specifically highlighted by the drastic increase in velocity from the $y = 11$ to $y = 12$ in. position. Here the dimensionless axial component of velocity increases in the downstream axial direction. One interesting item is the shape of the velocity profile. As the distance downstream is increased the profile exhibits the characteristic shape of a laminar flow around a hemisphere with low turbulence levels with the exception of a velocity reinforcement downstream. The velocity reinforcement is a phenomenon wherein the wake speed near the surface is actually greater than the speed associated with the undisturbed flow at a similar height. As reported by Roberson and Chen (1970) and Rainbolt (1968) the strength and position of occurrence of the velocity reinforce-ment is highly dependent on the level of turbulence in the flow. For high levels of turbulence the velocity reinforcement if it occurs at all occurs sooner and is weaker than flow with
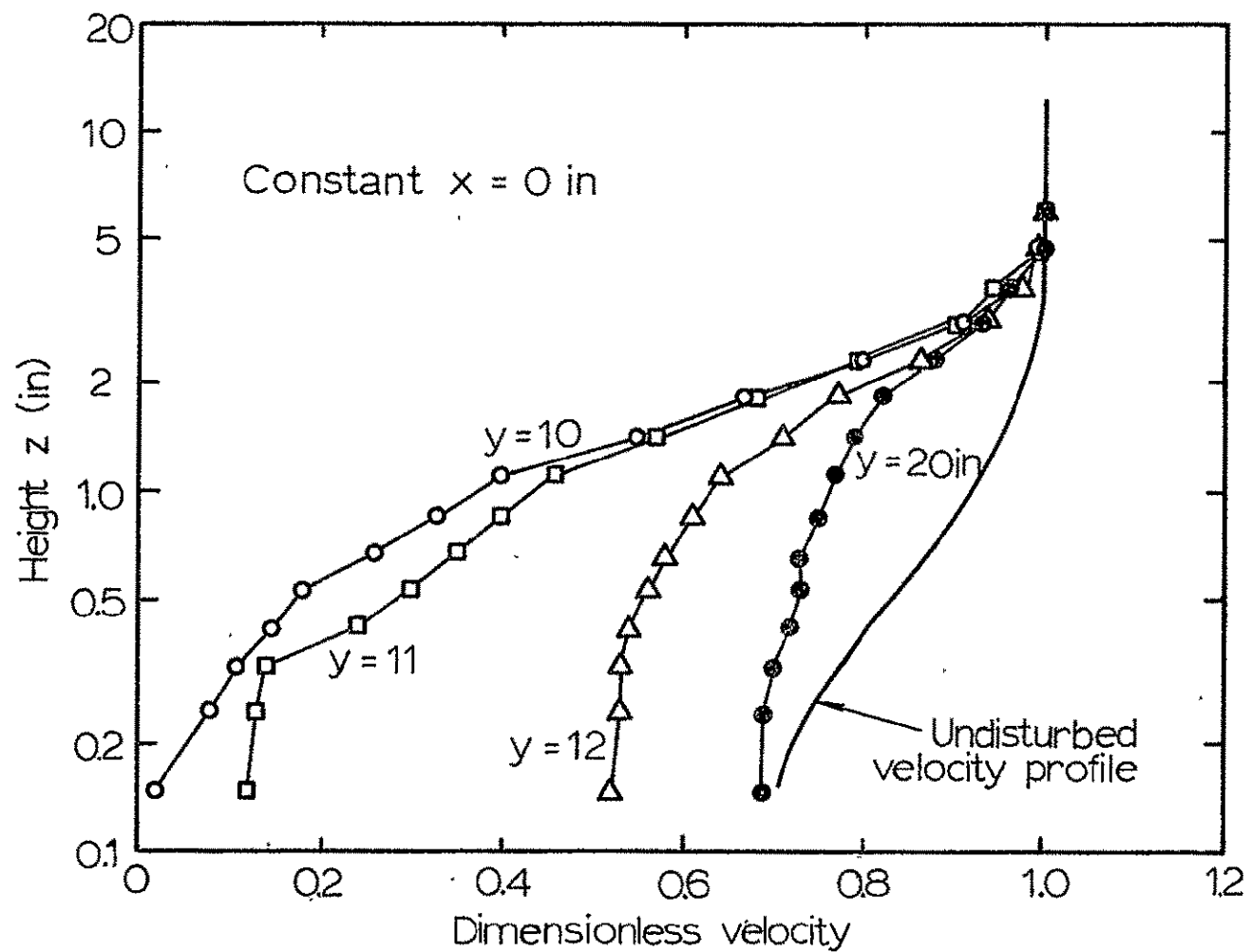
Figure 11. Crater wake vertical velocity profiles for x = 0 in.

less turbulence.

Figures 12-15 show plots of the dimensionless axial velocity component vs. the positive transverse length x at four different values of height z = 0.15, 0.424, 0.881 and 1.47 in. In each figure four different downstream values of y are presented, y = 10, 11, 12, and 20 in. as well as the corresponding value of dimensionless velocity associated with an undisturbed turbulent boundary layer at the same height. All points in each figure at a constant height were measured by a single pitot tube and pressure tubing and thus any discrepancies that would be caused by use of different pitot probes are eliminated. Figure 12 shows the greatest relative velocity defect from that predicted by freestream. This seems plausible since it has the lowest value of height above the surface z = 0.15 in. A very rapid increase in the velocity defect occurs over a relatively short distance (2 in.) and then a slower gradual increase to stream conditions. Almost identical trends can be seen in the corresponding curves of Figures 12-15, with changes in amplitude. An apparently unique trend can be observed in all four figures at a position of y = 11 in. This trend shows a lower centerline velocity (x = 0 in.) and then a velocity spike at roughly x = 0.5 in. and then a return to the averaged increasing velocity defect curve. This velocity spike occurs at only the lower heights in the measurements and since the phenomenon was measured with
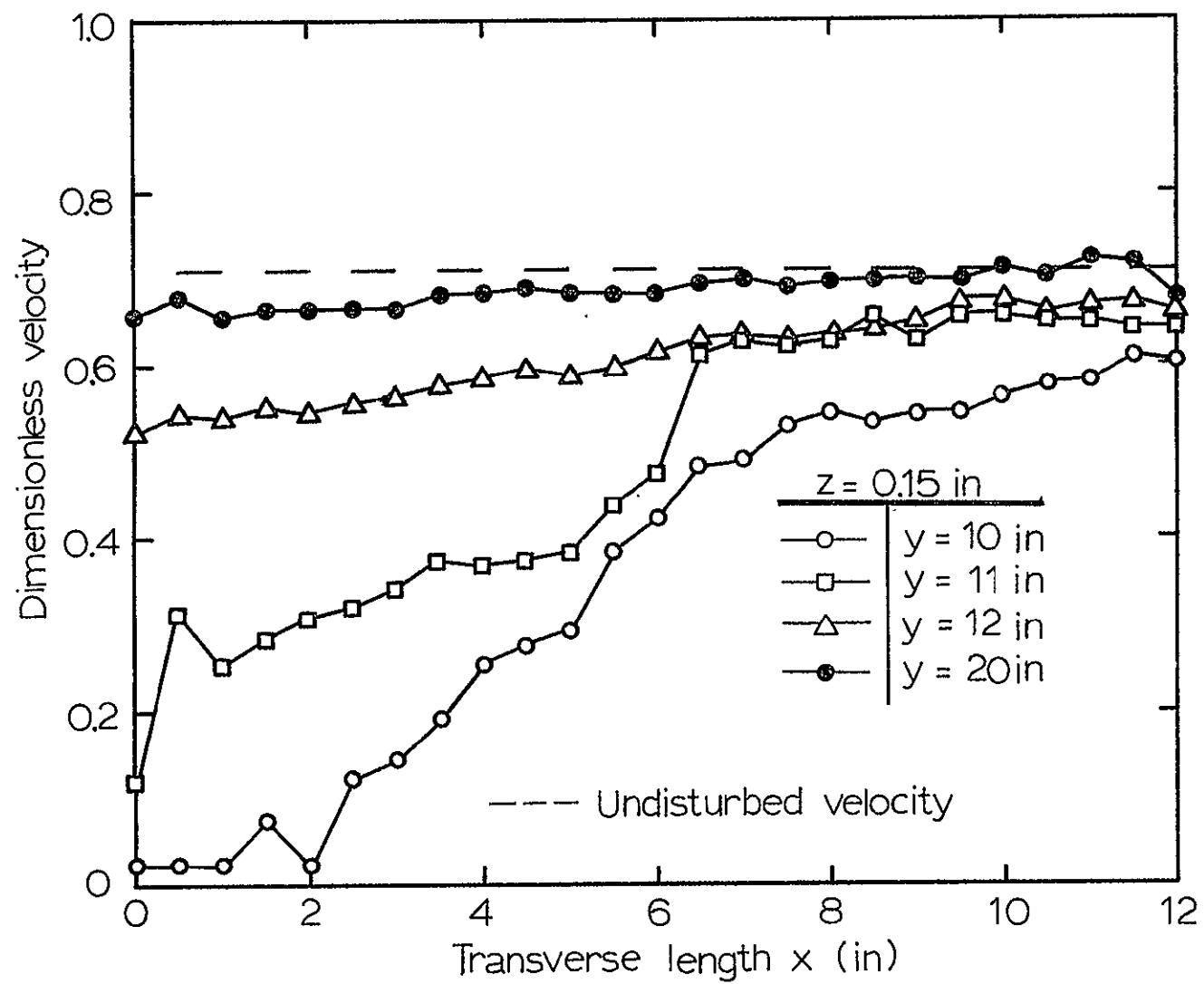
Figure 12. Crater wake lateral velocity profiles for z = 0.15 in.
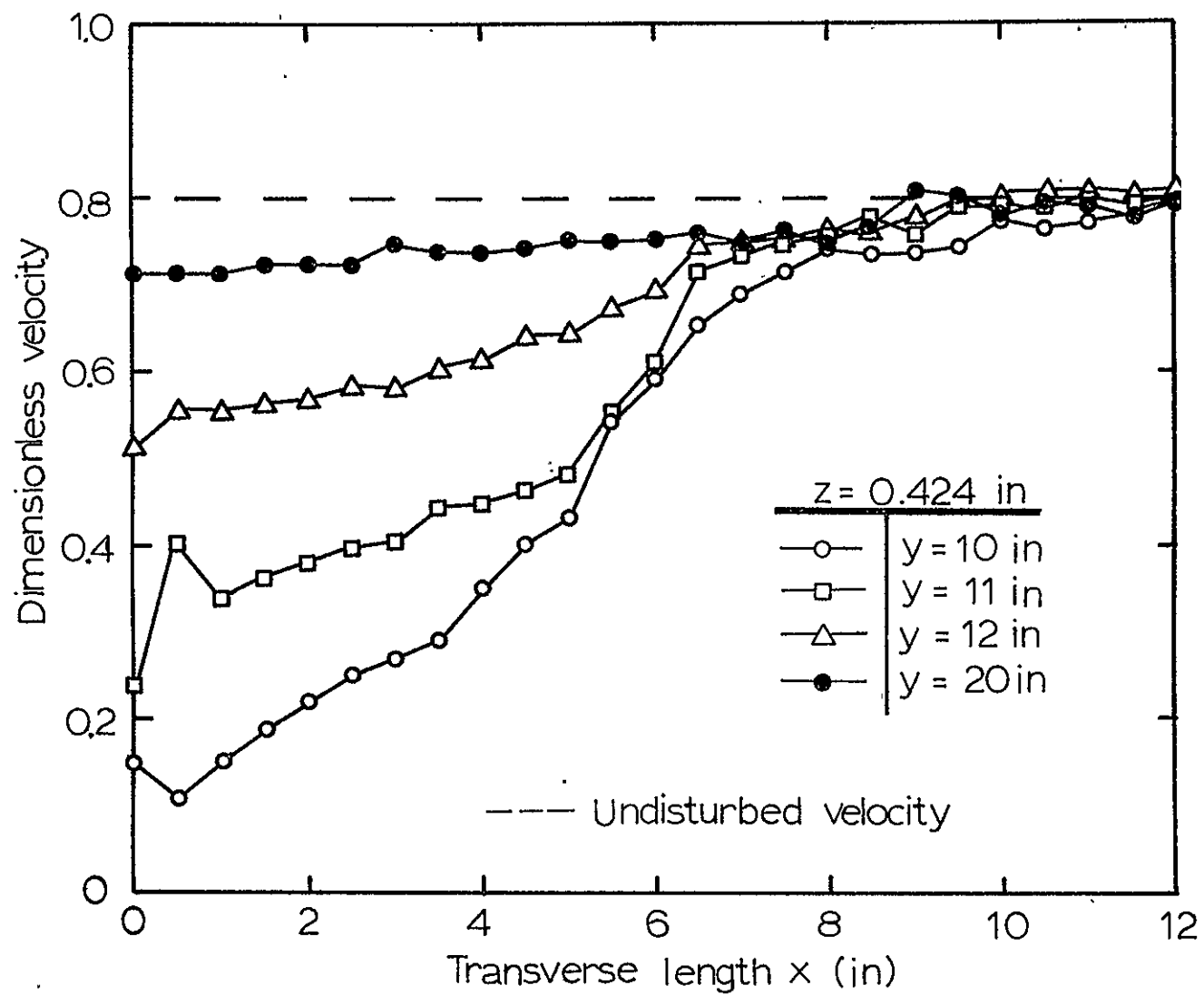
Figure 13.   Crater wake lateral velocity profiles for z = 0.424 in.
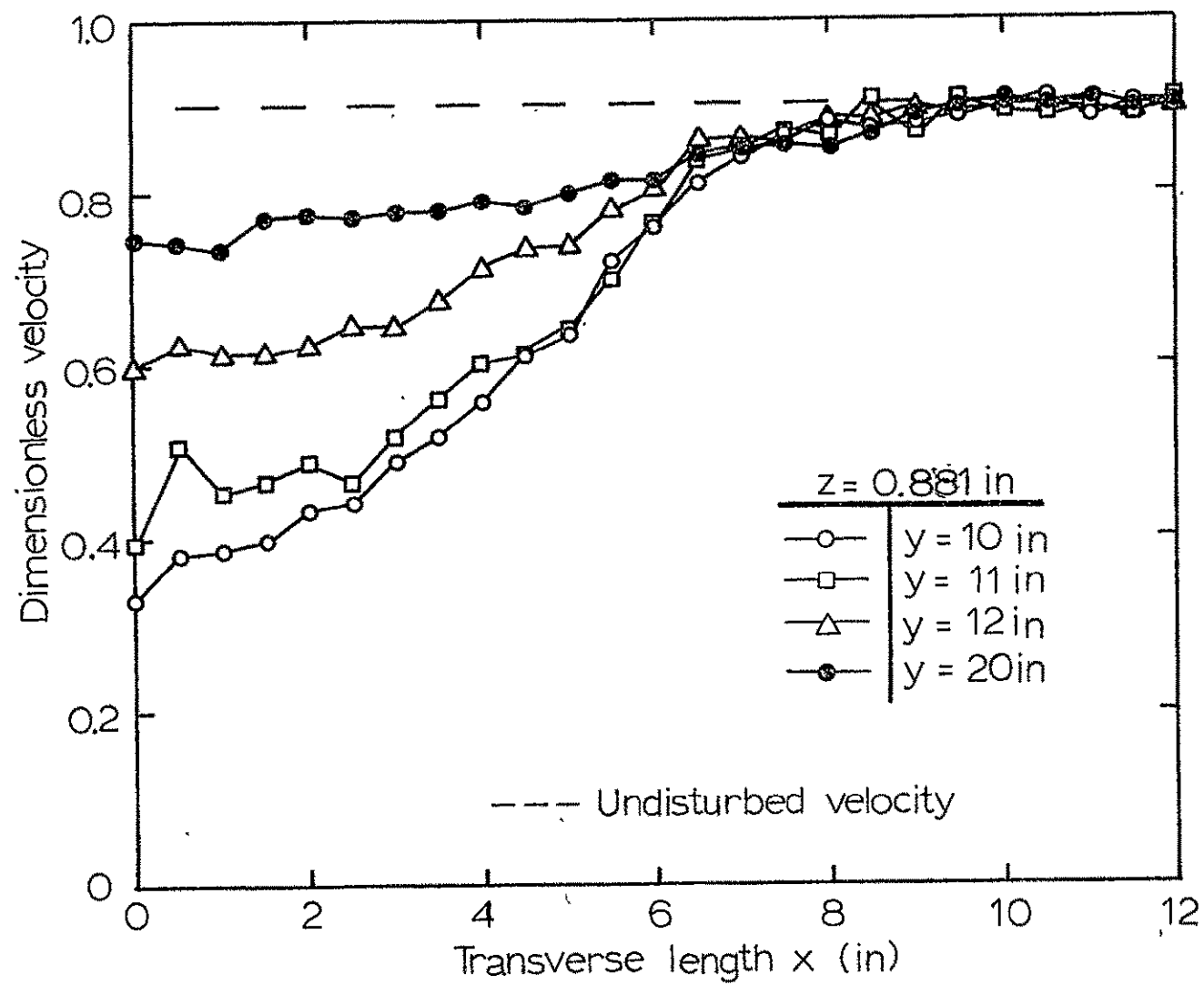
Figure 14. Crater wake lateral velocity profiles for z = 0.881 in.
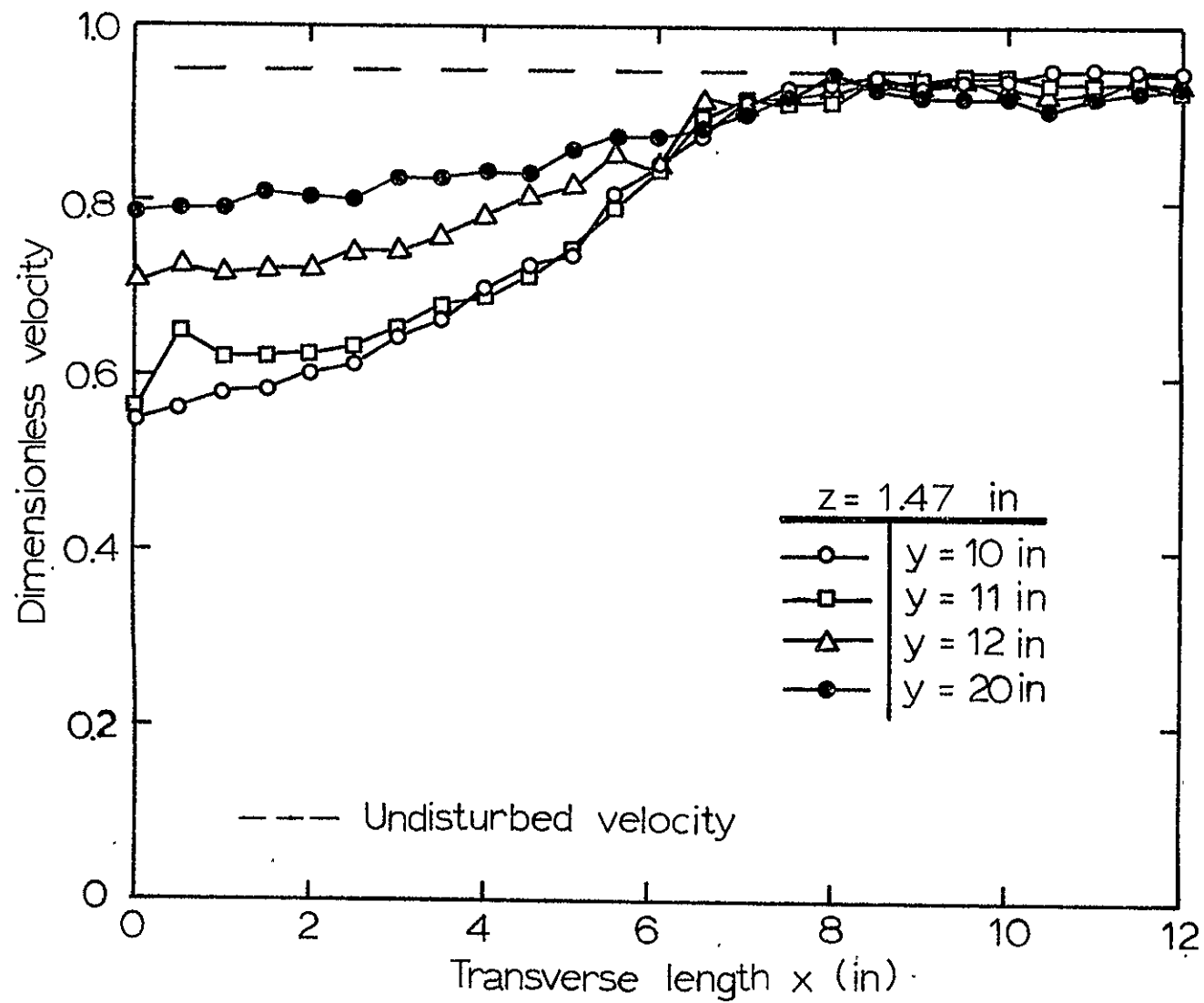
Figure 15. Crater wake lateral velocity profiles for z = 1.47 in.

different pitot probes it does not seem to be anomalous. If the flow is assumed to be symmetrical around the crater model then mirror images of velocity profiles would exist on the negative x side of the centerline. The resultant imagery of the velocity spike then matches the axial velocity profile of a horseshoe vortex system in laminar flow (Gregory and Walker, 1951). Although the flow in this case is turbulent a qualitative comparison can be made. The effect of turbulence on the horseshoe vortex makes it very difficult to obtain an instantaneous measurement of the flow with use of pitot tubes since they have the effect of time averaging the flow. In order to accurately observe such a vortex system the entire flow field must be instantaneously known, however such a task is not plausible from an experimental viewpoint. The meandering of the vortex cores makes measurements of the vortex properties impossible because of the time averaging effect. The geometry of the model crater to vortex system possibly makes the movement of the vortex small in the vicinity immediately behind the crater where the velocity spike is located. Although exact evidence of a vortex cannot be made from this analysis, the existence of some type of crossflow is shown. At a transverse length of 6 in. or greater away from the axial centerline the flow is within 90% of the undisturbed boundary layer velocity with the exception of Figure 12 where the velocity defect reaches out further transversely. As the

height is increased for the range of transverse direction to
6 in. the disturbance of the flow downstream is greater than
at lower heights (relative to undisturbed boundary layer
velocity at that height). This implies that turbulent mixing
is greater downstream in the flow near the centerline. This
region of greater mixing extends to a height of approximately
the same as the disturbing element (crater). This doesn't
seem unnatural as this also is characteristic of a wake.

A constant velocity contour plot for a two-dimensional
plane may be made with knowledge of the many velocity data
points within the plane. Figure 16 is such a plot. The plot
shows curves of constant dimensionless velocity (ratio of
axial component to freestream value of velocity) for the
height vs. the transverse direction of the plane y = 10 in.

A contour line represents an interpolated position for a
constant value of velocity. In Figure 16 an increment of
0.02 exists between contour lines. The values of several
contour lines are denoted in this figure and also in the
following figures involving contour plots (thus enabling the
value of the dimensionless velocity ratio to be known within
two percent anywhere in the contour plane).

Upon examining the contour plot of Figure 16 it is
evident that essentially for x greater than 8 in. the flow
profile is logarithmic but has a much slower speed near the
surface than that of undisturbed corresponding flow (Figure
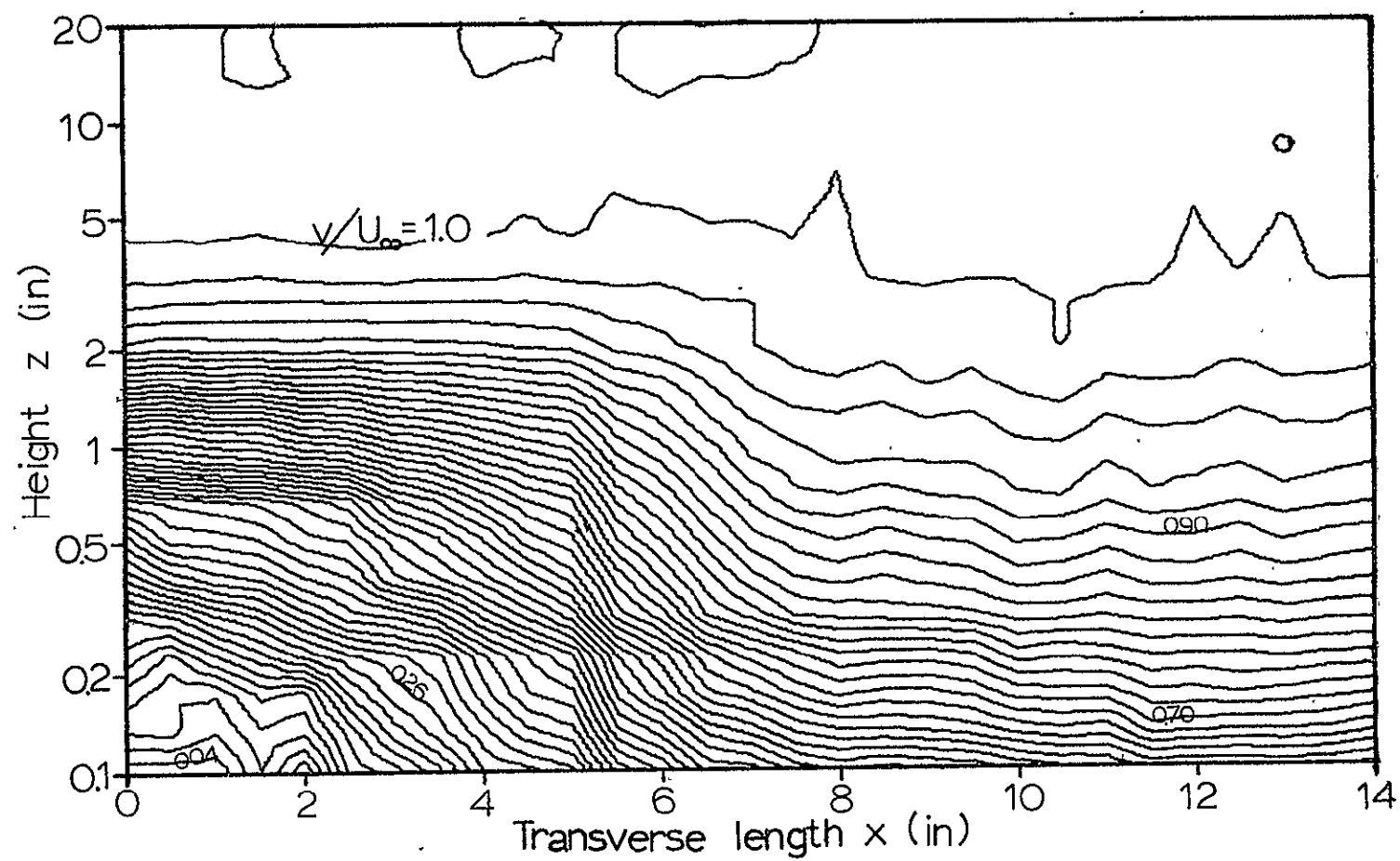
Figure 16. Crater wake lateral isotachs for y = 13 in.

17) for transverse distances greater than 8 in. Shear rates much greater than those associated with undisturbed flow exist for a range of height from 0.6 in. to 2.0 in. and extend transversely outward to approximately 6 in. (crater rim radius). It may also be noted that there exist regions of very small velocity for a transverse range from the centerline (x = 0 in.) to x = 2.0 in. at heights less than 0.2 in. This seems to show the existence of the stagnant air region believed to exist immediately downstream of the crater (Greeley, 1974).

Figure 17 shows an identical contour plot of Figure 16 with the exception that the plane is taken at an axial distance of y = 20 in downstream instead of y = 10. A comparison of these two plots shows much higher velocities near the surface and a drastically slower change of velocity with height at the x-z plane position of y = 20 than that of y = 10 in. A more regular pattern is formed in the y = 20 in. case that shows the flow is closer to equilibrium than the y = 10 in. case. Also in Figure 17 there are characteristics of wake flow near the axial centerline (x = 0 in.) at heights less than 1 in., e.g., the flow shows only a 6% increase on the axial center-line from a height of 0.1 in. to 0.6 in.

At positive transverse lengths greater than 7 in. in the flow the velocity profile is very nearly that of an undisturbed flow. The velocity measurement of the pitot tube nearest the
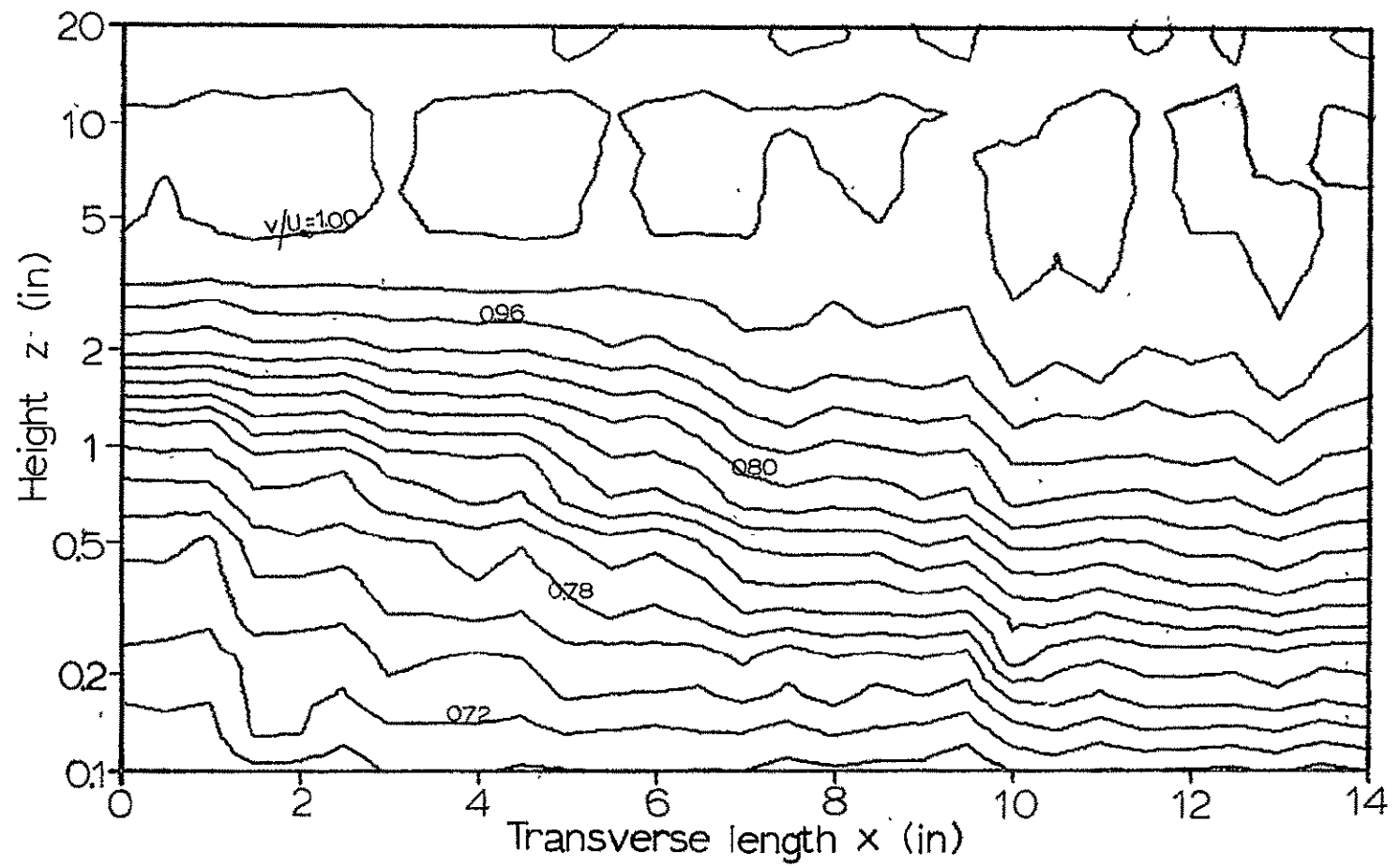
Figure 17. Crater wake lateral isotachs for y = 20 in.

wall was never less than 68% of the freestream velocity or the flow again has obtained a high shear rate in the first 0.1 in. of height above the wall surface.

The contour plots displayed in Figures 18 and 19 are of the y-z planes which are perpendicular to the x-z planes featured in Figures 16 and 17. Figure 18 exhibits the contours of constant velocity along the axial centerline (x = 0 in.) from y = 10 in. (located just behind the crater model) to y = 22 in. The plots show an extremely high acceleration of the flow along the axial centerline from y = 11 in. to y = 12 in. (also see Figure 10). The speed of the flow measurement at the lowest height above the floor (z = 0.15 in.) increases from 12% to 54% of freestream speed in 1 inch, then increases rather slowly with increasing distance downstream. Again the flow at a height of 0.7 in. to 1.2 in. has a higher velocity gradient from y = 10 in. to y = 12 in. than the remaining downstream flow demonstrates. Figure 19 is similar to Figure 18 except that the position of the y-z plane is not at the axial centerline but instead at a position of x = 17 in. This contour shows very little influence on the flow caused by the presence of the crater. Sedney (1973) also noted that the disruption of flow caused by a "small" scale disturbance is most noticeable in the local neighborhood of the disturbing element and does not greatly effect the flow outside the immediate downstream vicinity of the roughness
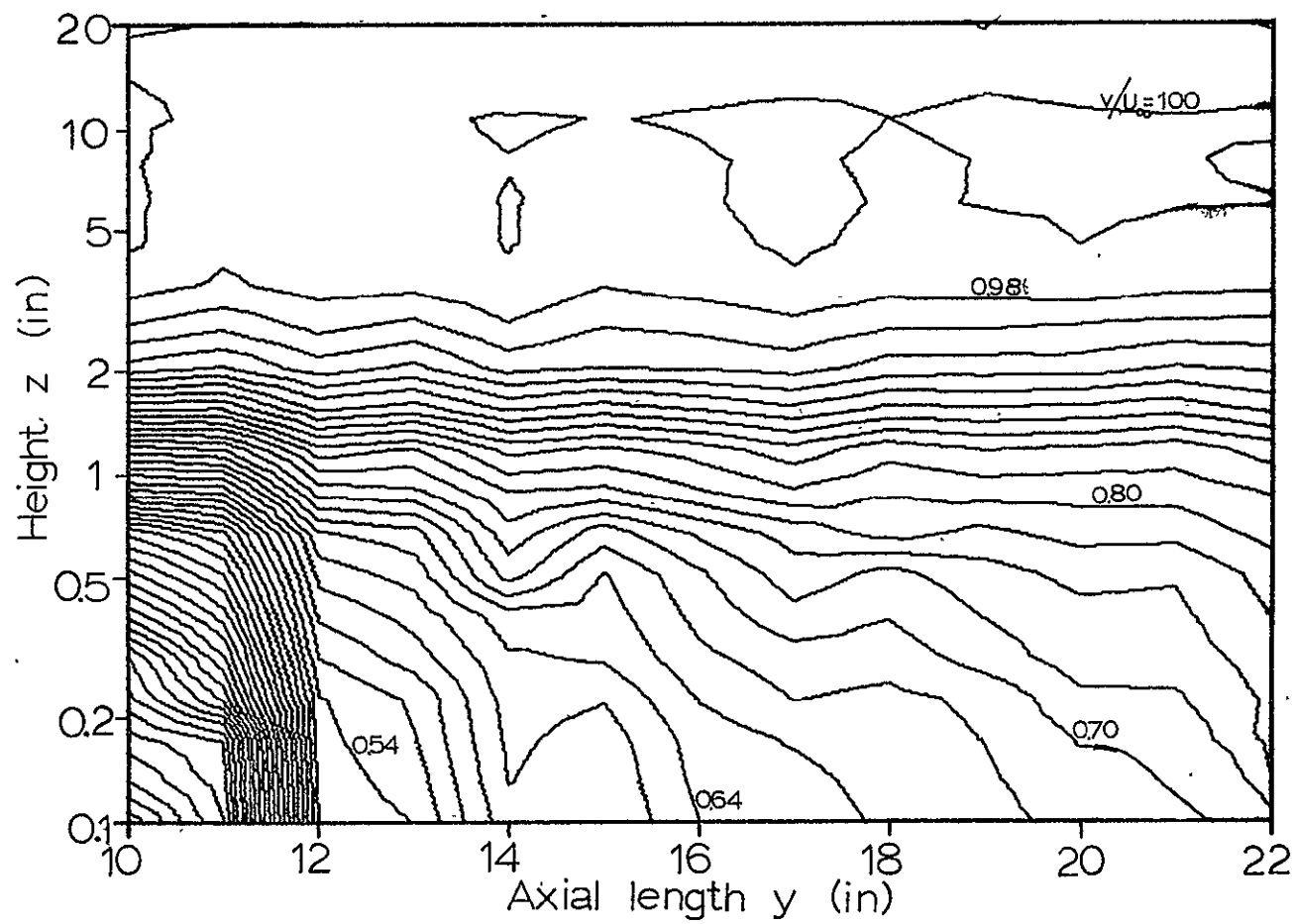
Figure 18. Crater wake longitudinal isotachs for x = 0 in.
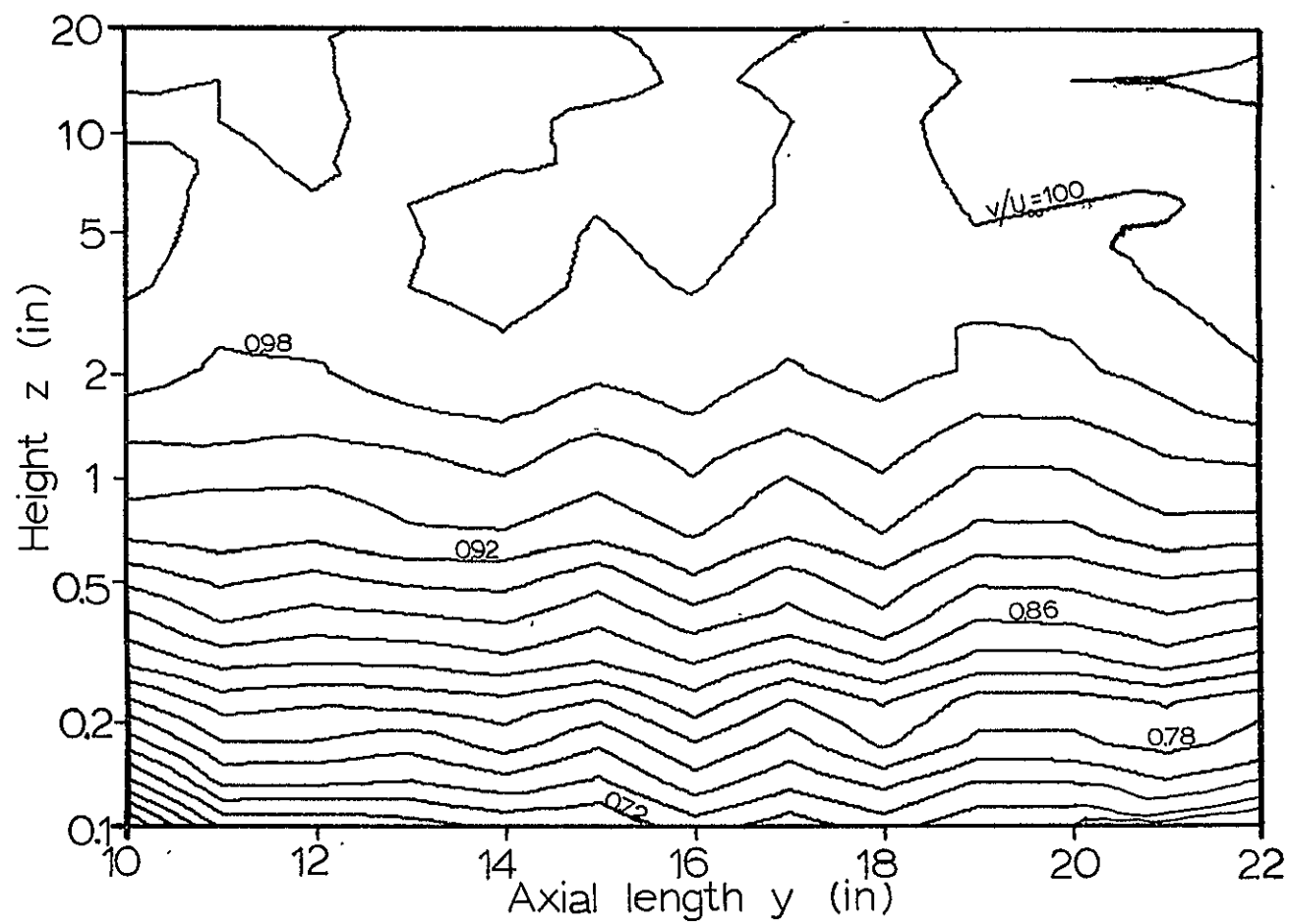
Figure 19. Crater wake longitudinal isotachs for x = 17 in.

1·02

element.

The data that form two-dimensional contour plots may also
be presented in a three-dimensional plot. Great insight of
characteristic trends can be accomplished by observing three-
dimensional plots. Figure 20 shows a three-dimensional plot
of dimensionless velocity vs. logarithmic height vs. axial
distance. The logarithmic height scale is similar to that of
the contour plots in Figures 16-19. This is again used to take
advantage of the logarithmic velocity profile of the turbulent
boundary layer and also used to obtain relatively more data
points in the lower heights where the velocity changes are
greatest. Figure 20 is a three-dimensional display of the
same data used to produce the contour plot of Figure 19. It
again is along the axial centerline (x = 0 in.) and extends
downstream from y = 10 in. to y = 22 in. The coordinates of
the four base points (A, B, C, D) of the three-dimensional dis-
play are also given in the figure. Base point A (hidden in
this particular picture) serves as the 'local' origin for the
figure. The axial increments shown are in units of 1 inch and
the height increments are in equal logarithmic height incre-
ments. Several discrete values associated with grid network
points are displayed to give proper perspective to the figure.
A close observation of this plot shows the same data displayed
in Figure 19 only in a different fashion. The dramatic
velocity increase can be easily observed in this plot. A

remarkable overall picture of the flowfield can be seen, with the net conclusion that the velocity defect caused by the crater is most apparent only in the first few inches immediately downstream.

A further comparison can be made between Figures 20 and 21. Figure 21 displays the data three-dimensionally that was used to produce Figure 18. Again comparison between Figures 18 and 21 will show exact corresponding trends. The location of the y-z plane shown in Figure 21 is 17 inches off the axial centerline. Although this is only approximately 1.5 crater diameters outside of the axial centerline, the flow remains nearly undisturbed except for a small velocity defect immediately downstream of the crater. Again the y-z plane is located relative to the crater coordinates system by surface corner points A, B, C, and D.

Figures 22 and 24 are corresponding three-dimensional plots of the contour plots in Figures 16 and 17, respectively. These plots are of the dimensionless velocity vs. the logarithm of the height vs. the transverse length x for x-z planes at constant values of y = 11 and 13 in. respectively. Figure 23 shows an immediate position of y = 12 in. The large velocity defect caused by the presence of the crater can be observed. There is a rapid increase in velocity with height and transverse length. Again several discrete grid network values are displayed to reveal the perspective of the figures. The
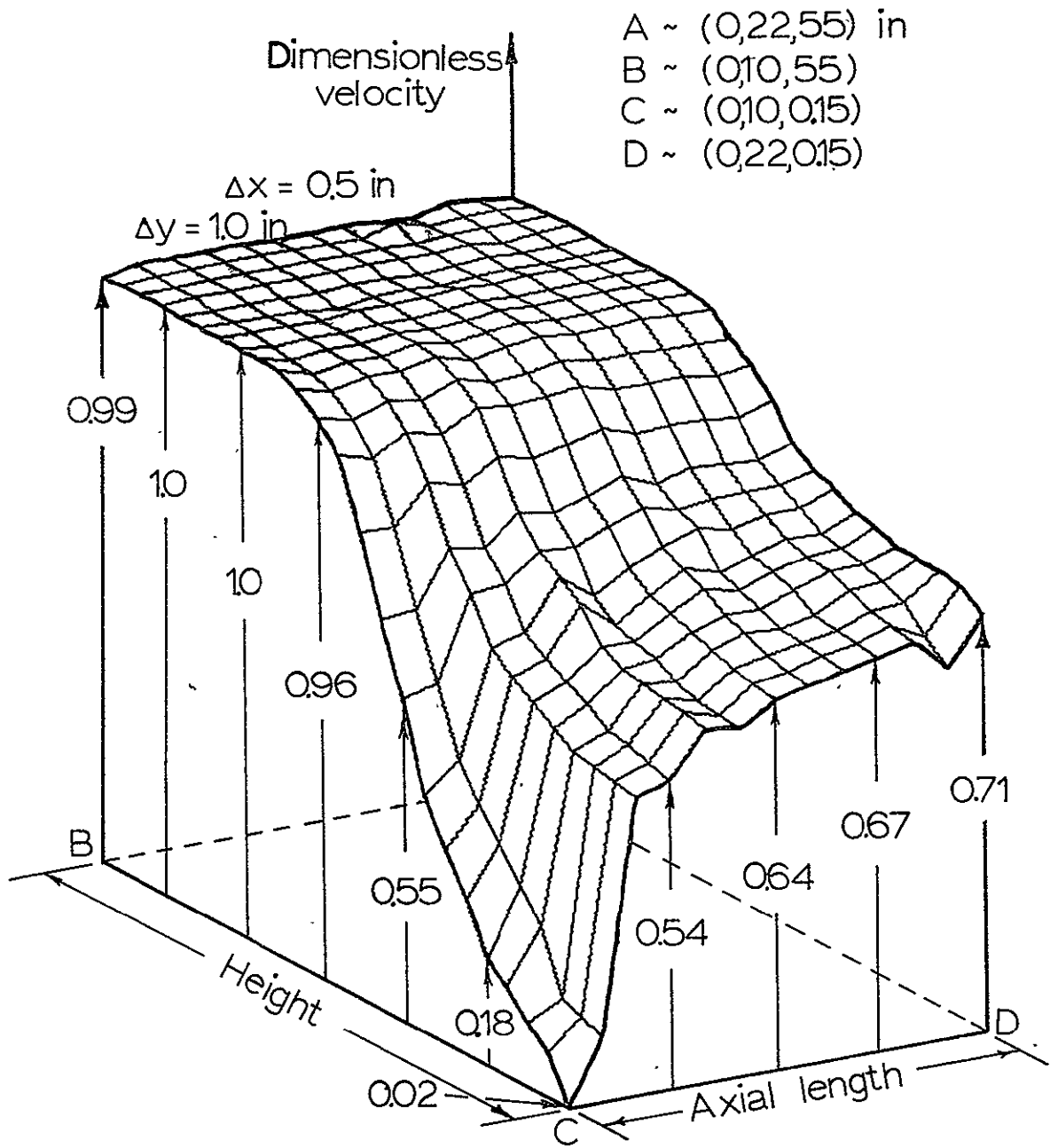
Figure 20. Crater wake velocity surfaces for x = 0 in.
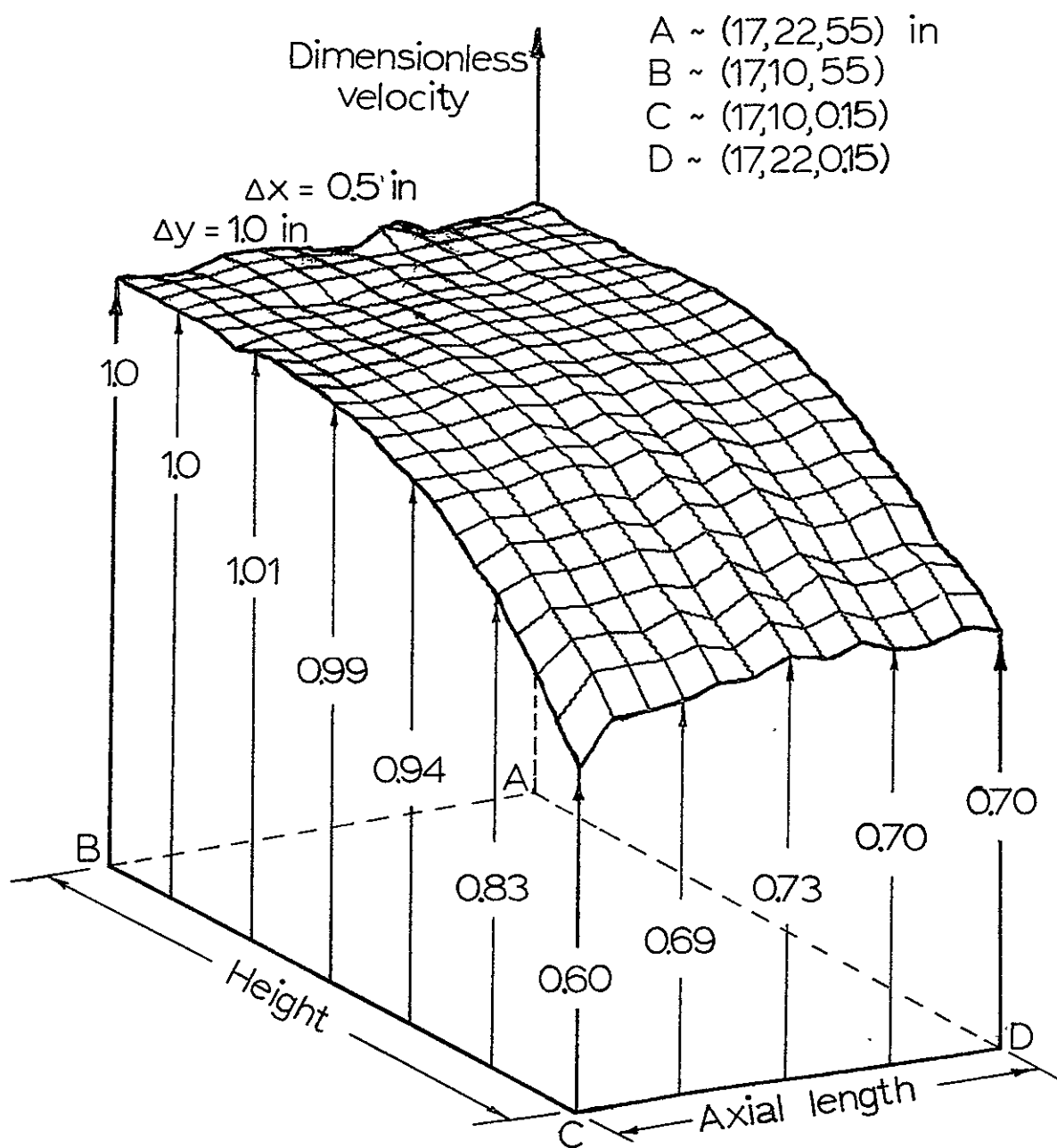
Figure 21. Crater wake velocity surfaces for x = 17 in.
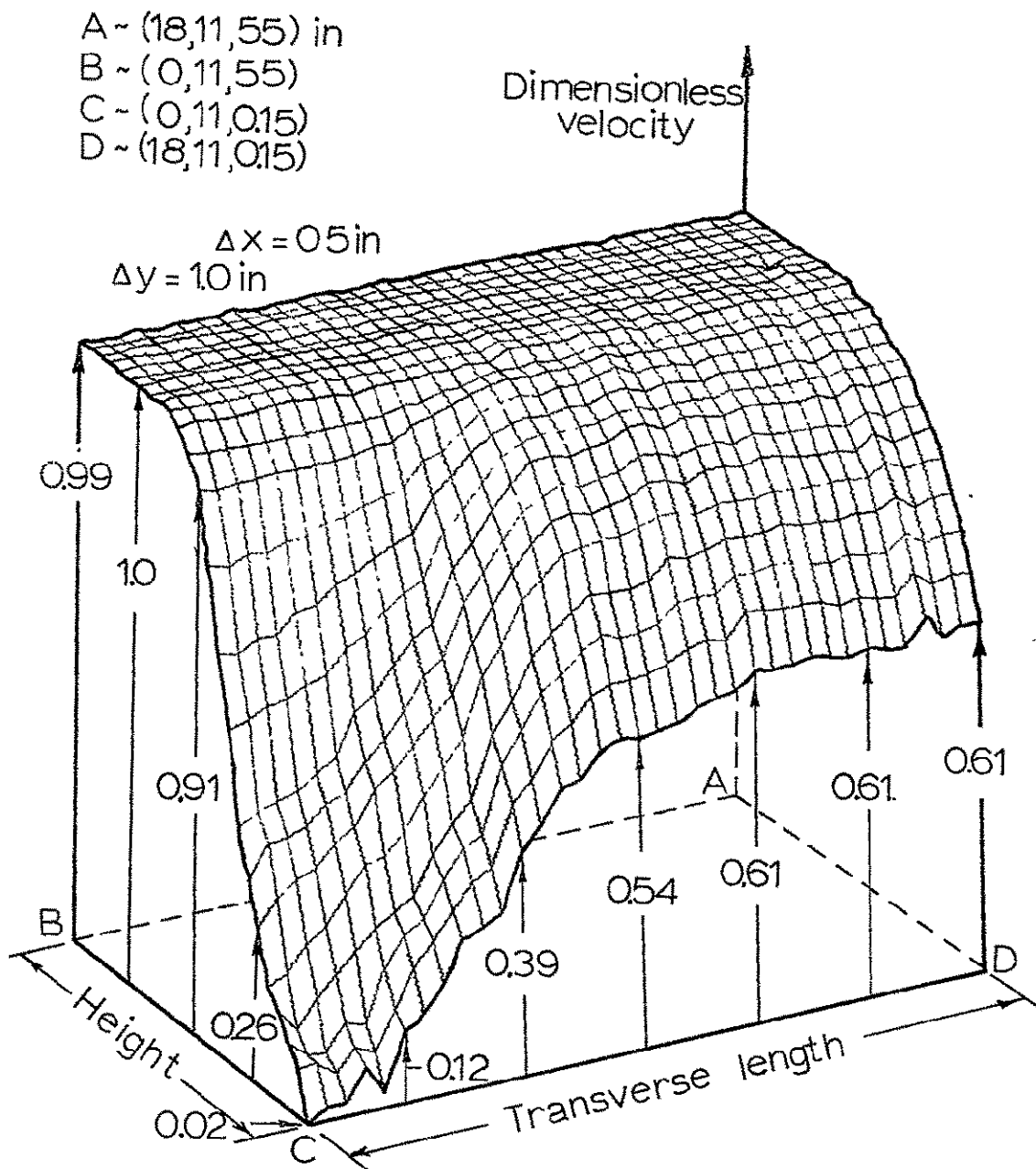
Figure 22. Crater wake velocity surfaces for y = 11 in.

A ~ (18,12,55) in
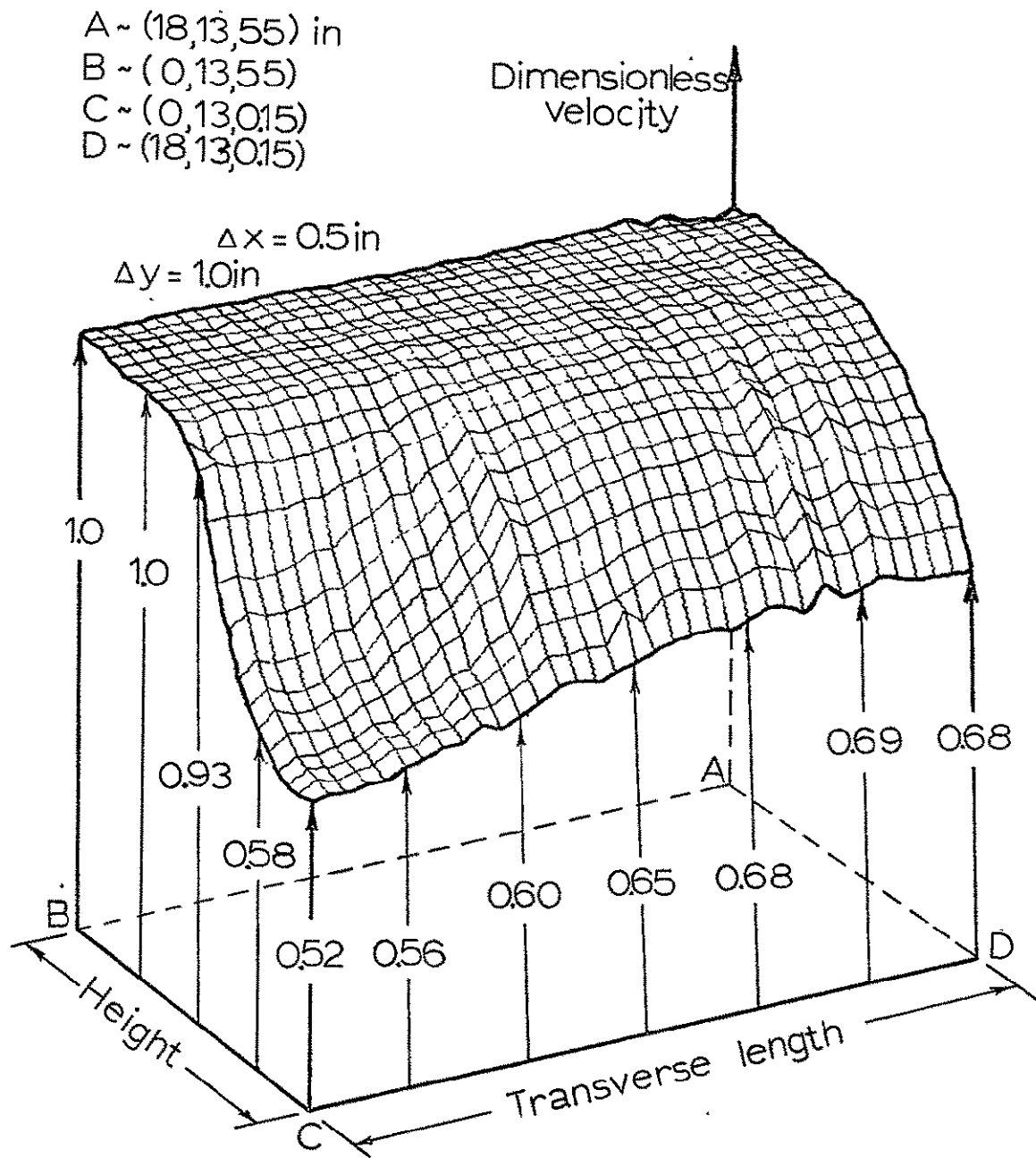B ~ (0,12,55)
C ~ (0,12,0.15)
D ~ (18,12,0.15)
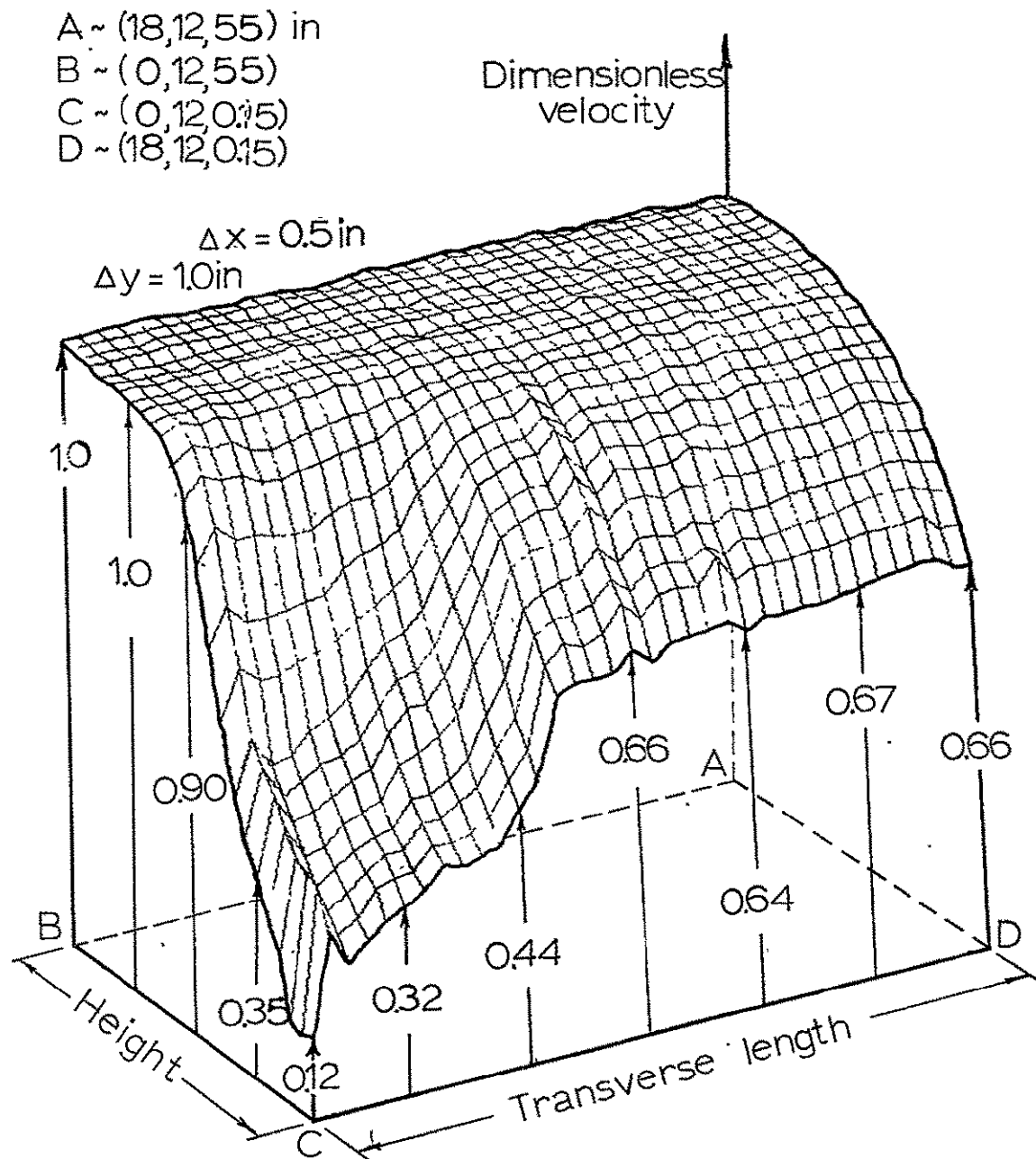
Figure 23. Crater wake velocity surfaces for y = 12 in.

A ~ (18,13,55) in
B ~ (0,13,55)
C ~ (0,13,0.15)
D ~ (18,13,0.15)

$\Delta x = 0.5$ in
$\Delta y = 1.0$ in

Dimensionless velocity

1.0

1.0

0.93

0.58

0.52   0.56

0.60   0.65   0.68

0.69   0.68

A

B

C

D

Height

Transverse length

Figure 24. Crater wake velocity surfaces for y = 13 in.

height increments are the same as in Figures 20 and 21 and the
transverse increment is 1/2 in. An immediate velocity defect
can be observed in Figure 23 and a very small velocity
influence can be noted in Figure 24. By comparing the three
Figures 22, 23 and 24 which occur only over a 2 in. axial
distance (y = 10 in. to y = 12 in.) an overall detailed picture
of the flowfield changes both axially and transversely can be
made. It might also be noted that three-dimensional plots of
similar nature to the above figures, only positioned further
downstream, reveal no significant change over the figure
presented in Figure 24. The overall velocity defect can be
observed by a comparison of Figures 16-24.

When the axial pressure and axial velocity profiles are
known in the three-dimensional downstream flowfield of the
crater a surface shear stress can be calculated from empirical
expressions.

The empirical expression used to calculate the surface
shear stress is one developed by Truckenbrodt (1955) for two-
dimensional boundary layer flow at zero pressure gradient.

$$\tau = \rho u_\infty^2 \; \frac{0.394 \; H^{-3.23}}{\left[\frac{u_\infty \theta}{\nu}\right]^{0.268}} \tag{5.1}$$

where H is the shape factor defined as δ^*/θ, δ^* is the boundary
layer displacement thickness and θ is the boundary layer
momentum thickness defined in the usual manner.

Although the first couple of inches of the measured velocity field may not be in a zero pressure gradient flow, and the flow is not two-dimensional, some insight can be gained about the surface shear stress distribution by examining calculated stresses and the trends they exhibit. Each of the 477 velocity profiles measured were numerically integrated to calculate the local displacement and local momentum thicknesses. With knowledge of the individual values of displacement and momentum thicknesses the surface shear stress can be calculated from Truckenbrodt's empirical relation from which the local value of the friction velocity $u_{*\ell}$ may be determined. Figure 25 shows a contour plot of the constant ratio of local friction speed to the friction speed associated with undisturbed flow under identical conditions for the axial distance downstream y vs. the transverse length x. The constant contour lines are in increments of 0.10 of the dimensionless friction speed ratio $u_{*\ell}/u_*$.

Upon examination the contour lines of Figure 25 show a region of high surface shear stress (friction velocity) that lies immediately downstream and in the wake of the crater. The region of high friction velocity (predicted by Equation 5.1) unfortunately may be invalid but the trends displayed by it seem to be correct. A comparison may be made with experimental data taken by Udovich (1973). Udovich performed a series of tests on the turbulent boundary layer flow around a
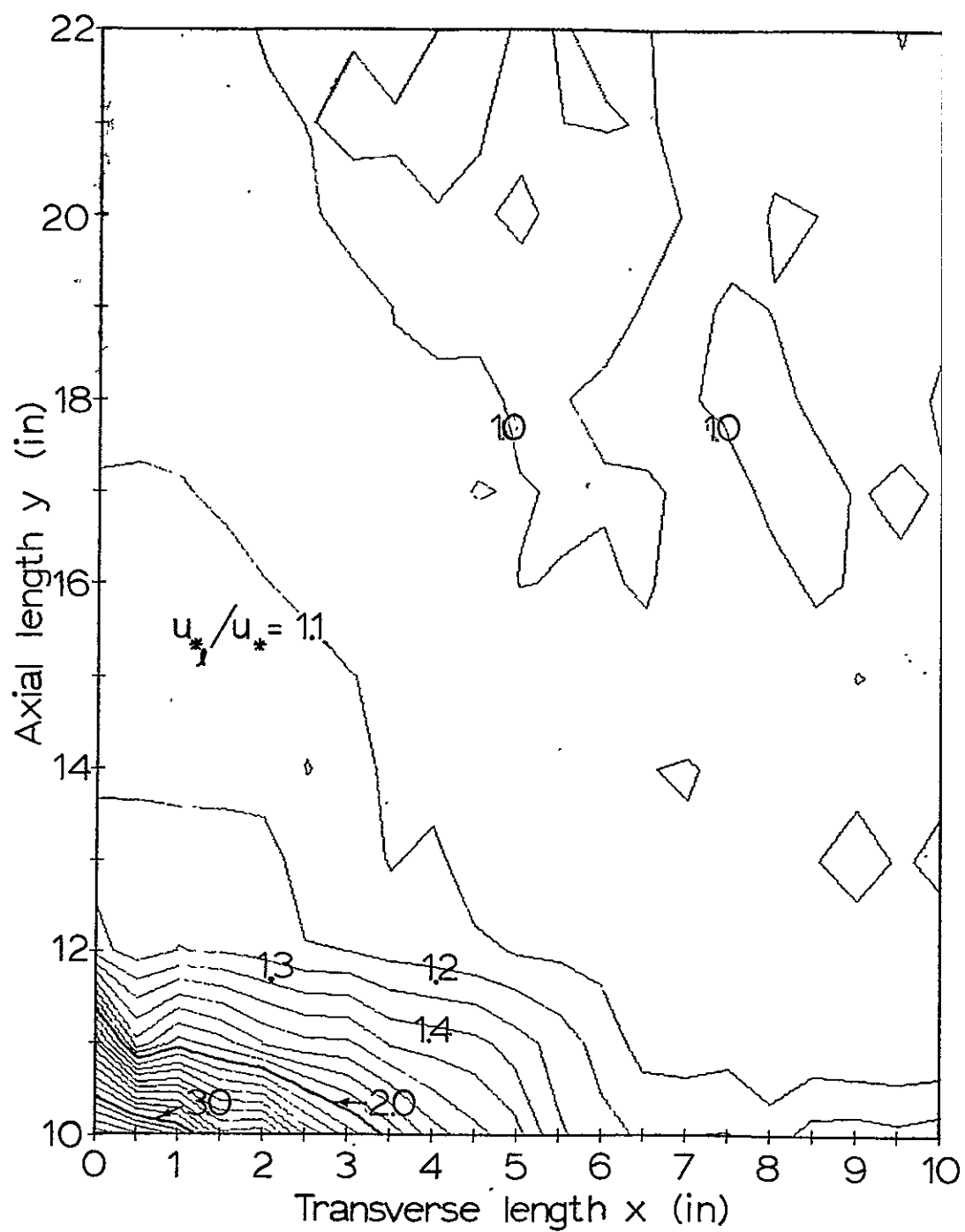
Figure 25.   Crater wake surface friction speed contours
(Truckenbrodt formulation)

singular idealized crater model. The crater had a 5 in. rim
diameter and a 7 in. overall diameter. The tests conducted
were to place a 1.5 cm circular patch of erodible material at
only one location in the crater flow field per test. The
freestream was then increased from a low value to a freestream
velocity that was sufficient to move the material within the
circular patch. Forty-five various positions were measured
twice and recorded. It is assumed that the local freestream
speed is proportional to the local friction speed. Then the
ratio of freestream speed necessary to move material in the
absence of the crater ,to that necessary to move material in
the presence of the crater is equal to the ratio of local
shear stress to the local shear stress in the absence of the
crater, i.e.

$$\frac{u_{*_\ell}}{u_{*_{un}}} = \frac{V_{\infty_{un}}}{V_{\infty_\ell}} \tag{5.2}$$

Figure 26 displays the results of Udovich's data if the flow
field is assumed to be symmetric and the mirror image posi-
tions on opposite sides of the axial centerline are averaged.
It is noted that there exists a large amount of scatter for
each data point. Figure 26 uses the same coordinate system as
Figure 25 with the exception that it is nondimensionalized by
the crater rim diameter. The dashed line represents the
experimental results determined on the curved slope of the
raised rim diameter. The shaded area of Figure 26 represents
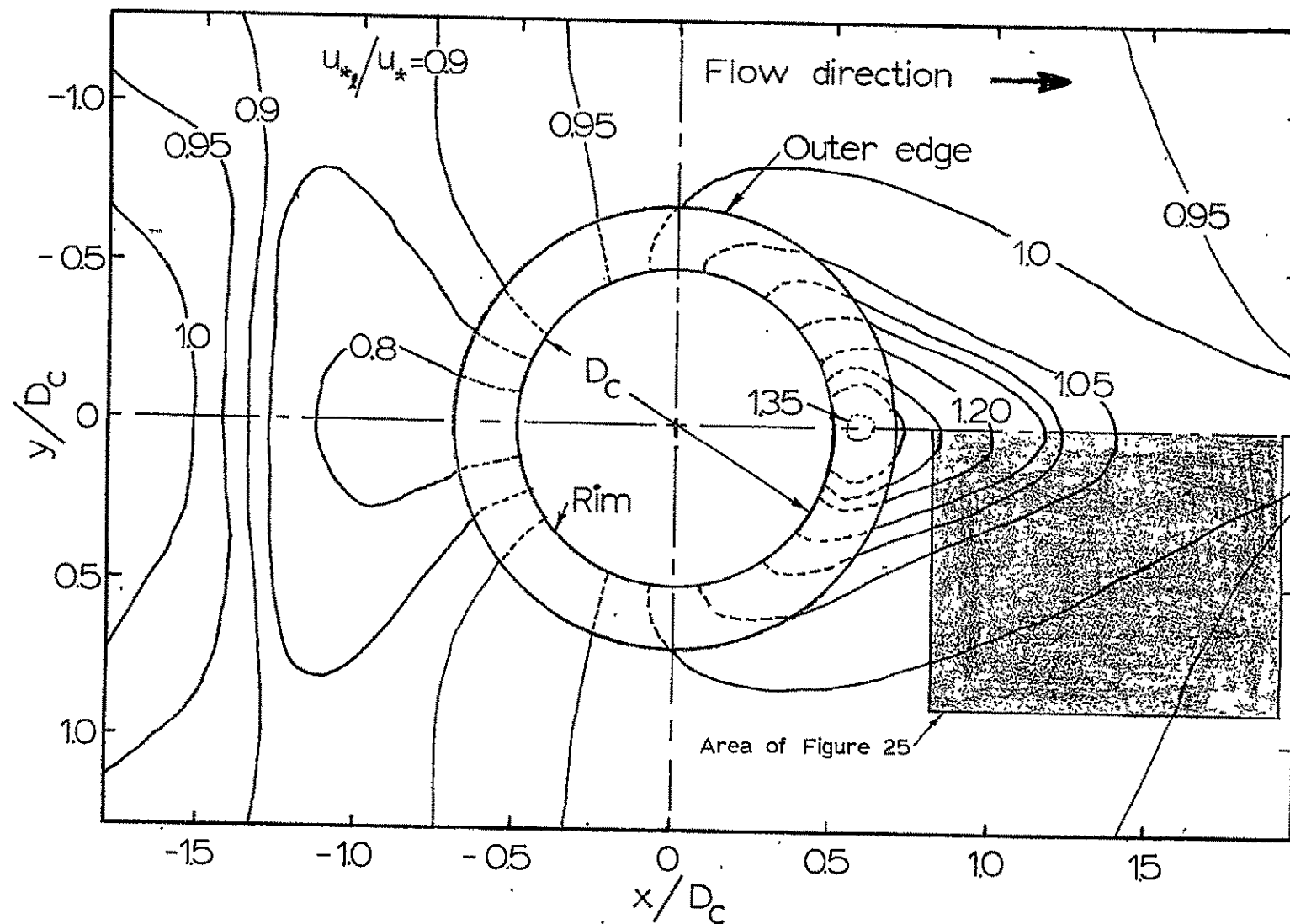
Figure 26. Crater wake surface friction speed contours (Udovich data)

the same area presented in Figure 25 if each are compared on
a dimensionless basis. A comparison between the shaded sec-
tion of Figure 26 and Figure 25 shows similar qualitative
trends for the ratio of friction speeds but quite a difference
in values of magnitude. For the regions of high surface shear
stress the true value of the friction speed ratio should be
somewhere between the two values given in the two figures,
since Udovich's experimental technique has a tendency to
underestimate the true value of the local friction speed and
Truckenbrodt's empirical results tend to slightly overestimate
the local friction speed. The numerical results obtained from
Truckenbrodt's relation should be assumed to be more accurate
than the data of Udovich. This may possibly explain the large
differences in the ratios of $u_{*\ell}/u_*$ of Figures 25 and 26.
The value of the friction speed ratio may also be a function
of the Reynolds number if it is below the critical value. For
Udovich's experiments the value of Reynolds number is just
below the critical value; however, the value of Reynolds
number for the experiments performed in Figure 25 was above
the critical value. This too could possibly account for some
of the differences.

2. Hot-film experiments

The second series of experiments conducted on flow around
the model crater were made with the aid of a hot film velocity
measuring device. A Thermo-Systems Inc. model 1080 total

velocity vector anemometer and model 1126 calibration system were used to measure the three-dimensional velocity vector. The system 1080 measures the velocity magnitude and direction over the full 360° solid angle flow fields. The device is capable of measuring speeds up to 300 ft/sec at one atmosphere of air and claims an accuracy of ± 3% of the magnitude of each direction ± 0.1% in total magnitude. It further claims two independent directional angle measurements each with 3° over the complete solid angle (4π Steradians). The temperature range is from 0°F to 200°F with capabilities of measuring the temperature within ± 2°F. The standard time constant of the electric circuitry is 20 milliseconds at 60 ft/sec at standard conditions although this can be altered by use of an active filter. The frequency response is one kilohertz direct current.

The system includes a streamlined probe which houses the orthogonal triad of hot film sensors, a 15 foot power cable, a power control circuit, a supplementary active filter, and also the pneumatic calibrating system. The three orthogonal sensors are single-ended rods which have a diameter of 0.006 in (0.15 mm) and length of 0.08 in (.2 mm). Each sensor rod is composed of a quartz rod with a thin conducting film made of platinum 0.0002 in thickness covered by a patented quartz coating. The data output of each measurement consists of six analog voltage signals, each of which has a possible range of 0-20 volts. The

output can either be measured by a digital voltmeter or displayed on an oscilloscope. The data can also be stored on a tape recorder or oscillograph.

The method used in these experiments was to use an active filter with a time constant setting of 30 seconds for each of the six voltage signals. It was necessary to time average each signal since the entire flow field could not be measured simultaneously and in order to compare results an average value was needed. Time averaging has the tendency to wipe out details of the vortex systems caused by meandering of the vorticies. However, large scale trends relative to the boundary layer thickness should still be observed.

The model 1080 probe was mounted on the vertical airfoil probe in similar fashion to the earlier described test. The cable leading from the rear of the probe was carefully secured above the surface downstream to the side of the wall and through the corner of the wind tunnel wall and floor to the control panel.

Experiments were made at two different transverse planes with four height measurements in each plane, 3/4, 1-1/2, 2-1/2, and 3 inches. These measurements were made in order to determine the lateral, vertical and axial speed components. The axial lengths downstream were $y = 12$ in. and $y = 18$ inches for the two transverse planes which were measured. Thirteen transverse positions were measured at each height and each

plane yielding a total of 104 individual positions of three-dimensional velocity measurements. Each measurement took approximately 45 minutes to make. Before each session of testing the model 1080 system was calibrated and adjusted if necessary to identical settings for all measurements made. The freestream speed was approximately 50 ft/sec ± 2 fps/sec in order to obtain greatest accuracy as described in the Thermo-Systems Inc. Instruction manual (1970). The data were recorded and reduced according to data reduction procedure as found in the Instruction manual. A data reduction technique described by Teilman et al. (1971) as a so-called 'improved' technique was also used for various positions and no significant difference existed.

Figure 27 shows a plot of height vs. transverse length for an axial location of $y = 12$ in. adjusted to symmetric flow. At each position where a measurement was made a dimensionless velocity vector is plotted for the crossflow components w and u. The velocity vector is made dimensionless by dividing the crossflow magnitude by friction speed associated with free-stream flow. Several values of the crossflow velocity ratio are given to show relative magnitudes. Within a transverse length of 6 inches there appears to be a general turning of the crossflow inward and also upward. This appears to be a plausible result since the location of the z-x plane is at $y = 12$ in. whereas the flow was earlier shown to be in a high
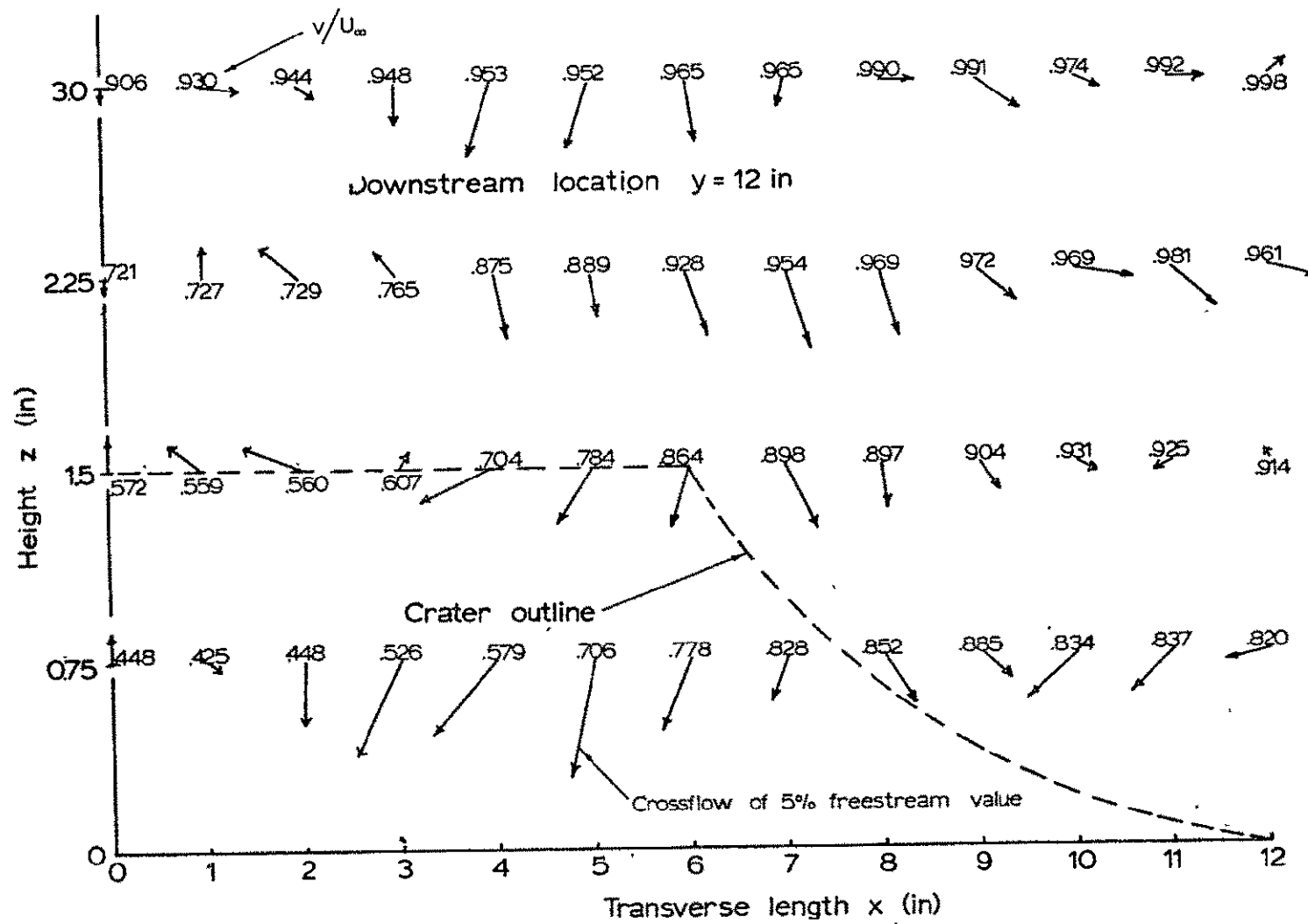
Figure 27.   Crater wake crossflow velocity vectors for y = 12 in.

velocity gradient region. The flow must return inward downstream in order to form the high velocity of the wake region downstream of the low-speed region formed immediately downstream of the crater. The absolute time-averaged magnitude of the crossflow at any position measured did not exceed 7% of the total magnitude of the velocity vector. The magnitude (strength) of the crossflow would of course depend upon the geometry of the disturbing element that gives rise to the formulation of the vortex (crossflow) system. The smaller scale effects of the vortex system would not be expected to be observed in this type of time averaged measurement due to meandering of the vortex cores.

VI. NUMERICAL SOLUTIONS

The equations of motion for a spherical particle under various given conditions were solved by a numerical computing technique which employs the use of a scientific subroutine package called node. Node calls six other subroutines, three of which must be supplied by the user. The solution of first order ordinary differential equations with initial conditions is obtained by using the predictor-corrector equations of R. L. Crane (1962). These equations have a wide range of stability. The necessary back points are initially calculated with the Runge-Kutta-Gill single-step method. The corrector procedure is not iterated. Node has the ability to automatically check the solution's accuracy at each step and change the stepsize to meet the specified accuracy of the user if it exceeds the error limit. It also will double the stepsize (provided accuracy is met) in order to reduce computing time. Copies of the computer program used for the solution of the particle trajectory equations of motion may be obtained at the Department of Aerospace Engineering, Iowa State University, Ames, Iowa, 50010, with reference made to this study.

All particle calculations have several common elements involved in the numerical solution. Table 3 displays the values of the constants of the acceleration of gravity, coefficient of the kinematic viscosity, and the density for

Table 3. Calculation variables

Variable	Earth	Mars
$g \, (\text{ft/sec}^2)$	32.1725	12.5679
$\nu \, (\text{ft}^2/\text{sec}^2)$	1.5×10^{-4}	116.786×10^{-4}
$\rho \, (\text{slugs/ft}^3)$	2.25×10^{-3}	2.00×10^{-5}
$\rho_p \, (\text{slugs/ft}^3)$	3, 5, and 7	3, 5, and 7
$u_* \, (\text{fps})$	1,2,3, and 4	10,15,20,and 25
$D_p \, (\text{microns})$	50 - 1050	50 - 1050

both Earth and Mars. Also shown in the table are the various

ranges of particle density ρ_p, friction velocity u_*, and

particle diameter D_p for which particle motion was calculated.

The numerical computing scheme specified four place accuracy.

Most particle trajectory calculations were initiated with

a value of height one-half diameter above a plane surface.

Since a particle's geometric relation to an actual surface

composed of like particles is not unique but rather is one of

a random distribution of heights, the calculation is assumed

to represent an average particle trajectory. Several

different initial values of height were calculated with many different types of lifting functions (all functions of height z). These calculations exhibit a very nearly constant particle motion for initial values of height of three-tenths to seven-tenths of the particle diameter. Above and below these values, particle motion was drastically curtailed. A possible explanation of this is that in the case of initial values of height less than 0.3 the air speed is much less than that of the higher heights and thus the lift force is much smaller. In the case of initial values greater than 0.7, since the lift coefficient C_L is a function of height and becomes very small at larger heights, again the lift force is small.

All values of drag coefficient C_D are calculated from the equation listed in Appendix A. For the case of the rarefied atmosphere on Mars a correction factor based on C. N. Davies (1945) equation is applied to the equations of motion for a value of mean free path, $\lambda = 13$ microns. The mean free path of the Martian atmosphere was calculated from Equation 4.27 assuming an atmospheric surface pressure of 5 mm of mercury. All particles were assumed to be point masses located at the center of the particle.

The coordinate system used for two-dimensional particle trajectories is one for which the positive z-direction, measured from the mean level of the surface, is upward away

from the surface. The x-direction is aligned in the downstream direction of the boundary layer flow. For the case of three-dimensional simulation of flow around a crater the coordinate system is that described in Section V with corresponding Figure 9.

Figure 28 shows a plot of the particle friction Reynolds number versus size of the particle diameter for Earth and Mars cases. The solid lines denote the Earth case for the different values of friction speed u_{*_∞} and the dashed lines represent Mars. As can be observed from this figure all cases of the calculations for Mars lie in the regime of a turbulent boundary layer with the existence of a laminar sublayer. The majority of the Earth cases calculated lie in the transition region with the exception of the smaller diameters for each friction speed for which a laminar sublayer would exist. The changing of particle density ρ_p does not affect the curves of Figure 28.

A. Two-Dimensional Calculation of a Particle's Trajectory Under Earth Surface Conditions

The numerical solution solves the motion of a single particle under various given conditions. The initial conditions calculated were: i.) particle densities of ρ_p = 3, 5, and 7 slugs/ft^3, ii.) friction speed u_* = 4, 3, 2, and 1 fps., and iii.) a particle diameter range from 50 - 1050 microns in equal increments of 100 microns. This represents
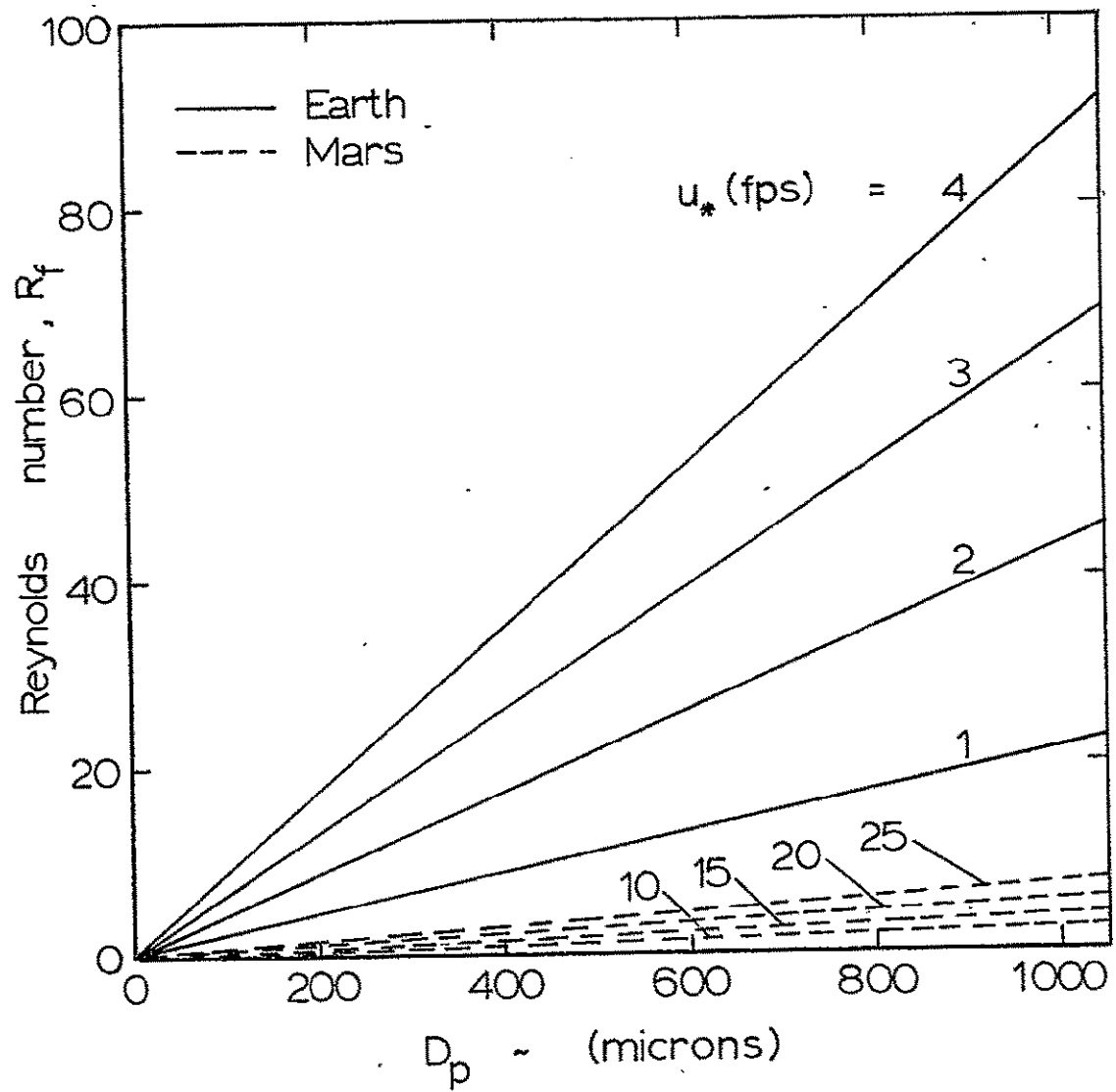
Figure 28. Friction Reynolds numbers for sample calculation for Earth and Mars

165 separate cases calculated for each of several different

representations of lift force as well as the case of no lift

force with only a given initial upward velocity component.

Functions of the lift force were developed for both the case

of a turbulent boundary with no viscous laminar sublayer and

with one that has a laminar sublayer.

1. Case of no lift force

The dimensionless equations of motion were numerically

solved for an initial upward speed equal in magnitude to the

friction velocity, i.e.,

$$w_p = \dot{z} = u_* \tag{6.1}$$

No lift force was present in these calculations and particle

motion is due solely to the initial prescribed vertical

velocity. For the turbulent boundary layer flow both the case

of a laminar sublayer present and the case with no laminar

sublayer existing were calculated. Figure 29 records the plot

of the value of maximum height (in millimeters) obtained

during the particle's trajectory versus the particle diameter

size D_p for friction speed $u_* = 4$, 3, 2, and 1 fps. Both

types of turbulent boundary layer flow are presented. The

solid line represents the case of a fully turbulent boundary

layer while the dashed line represents the situation of a

laminar sublayer present in the flow. This plot is for a

constant particle density of $\rho_p = 5$ (slugs/cubic ft) (the
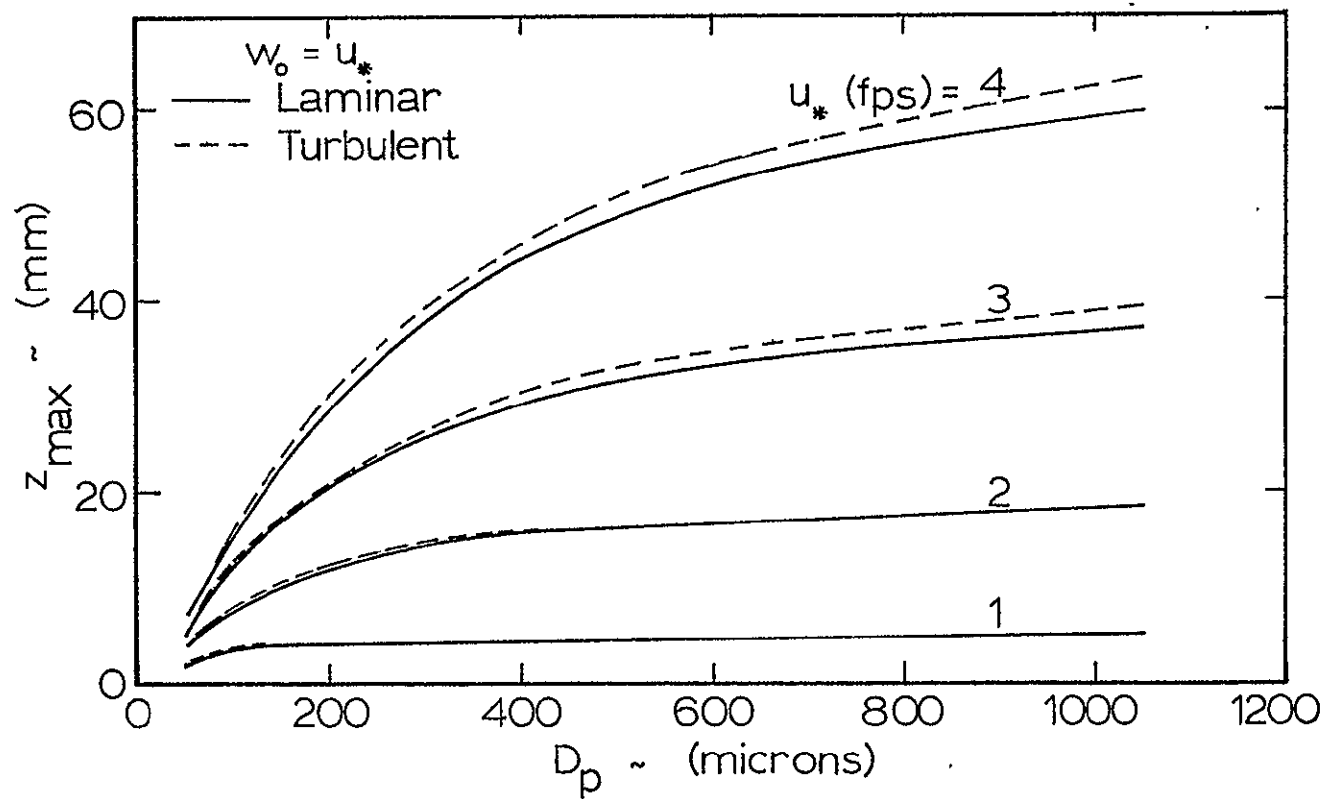
Figure 29. Maximum trajectory height for Earth, no lift, $w_o = u_*$

average density of typical sand particles). The trends with respect to u_* exhibited by particles of density $\rho_p = 3, 7$ are similar although the maximum heights are lower for lighter particles and higher for the denser materials. A typical example is a friction speed $u_* = 3$ fps for the fully turbulent boundary layer flow for a 450 micron diameter particle for which the maximum trajectory heights obtained by the different particle densities $\rho_p = 3, 5, 7$ were 27.8, 31.8, and 34.2 mm, respectively. Since the initial momentum given to the particle increases with increasing particle density, consequently the maximum height obtained in the trajectory is increased. This trend does not jibe with observation. The case of fully turbulent boundary layer flow yields a higher maximum height than that of a laminar sublayer flow for larger particles. This effect rapidly diminishes with decreasing friction speeds as exhibited by the coalescing of the curves for $u_* = 1$ and 2 fps. An apparent trend is that for a constant u_* and increasing particle size the maximum height of the trajectory approaches a constant value. This trend is basically wrong since the trajectory's maximum height must at some point begin to decrease with increasing size. At some uniquely defined D_p the constant friction speed will be equal to that of the threshold for which particles larger than this physically could not lift off. Since the threshold friction speed versus friction Reynolds number curve is a double-valued curve, there is

also a lower limiting particle diameter below which particles
will not lift off. The maximum difference between the two
types of calculation (laminar sublayer, no sublayer) is never
greater than 4%. The result of these calculations show that
for larger particles the initial upward (or maximum) velocity
is not constant but should be a decreasing function of particle
size as well as a function of friction speed. It will be
shown later that if u_* is held constant that w_o (the maximum
or initial vertical velocity component) is nearly constant for
smaller size particles and then monotonically decreases for
increasing particle size.

2. Case of lift function for turbulent boundary layer with a laminar sublayer

The analytically derived lift coefficient function (see
Equation 4.41) from Saffman's (1965, 1968) original work was
applied to a fully turbulent boundary layer situation and
incorporated into the equations of motion. Particle trajec-
tories were calculated and compared to the limited experimental
data available. There was no initial velocity given to the
individual particles. The resultant trajectories were found
to be small in comparison to experimental work performed by
Zingg (1953).

Zingg's data do not give the average trajectory of
particles but rather an average height (particle mass flux
above equals mass flux below) calculated from experimental

distribution of particle material caught in a vertical tray. An average particle size is calculated from the particle distribution and associated with an average height. An empirical equation was developed by Zingg to match the experimental data. Figure 30 shows a plot of the average height versus particle size. Although Zingg's equation matches his experimental data, the trend of indefinitely increasing particle height with increasing particle diameter for a constant friction velocity is invalid. The same reasoning of the previous section can also be applied here and Zingg's empirical curves predict particle motion for conditions for which friction speeds are far below that of threshold. This is obviously in error. Although Zingg's empirical curve breaks down for large particles it should be valid for the vicinity in which the experimental data were taken. Although a direct comparison of Zingg's data to the present calculations is not strictly valid, the comparison is of some interest. The range of calculated maximum height should be from the average height of Zingg's data to approximately two times it, assuming the average height of the data to be somewhere between one-half the maximum height and the maximum height.

The effect of the wall on particles near and resting on the wall was not considered in the above calculation, however, it appears to have an important effect on both the lift and drag coefficients. From Saffman (1965), on the wall effect of particles in simple shear flow:
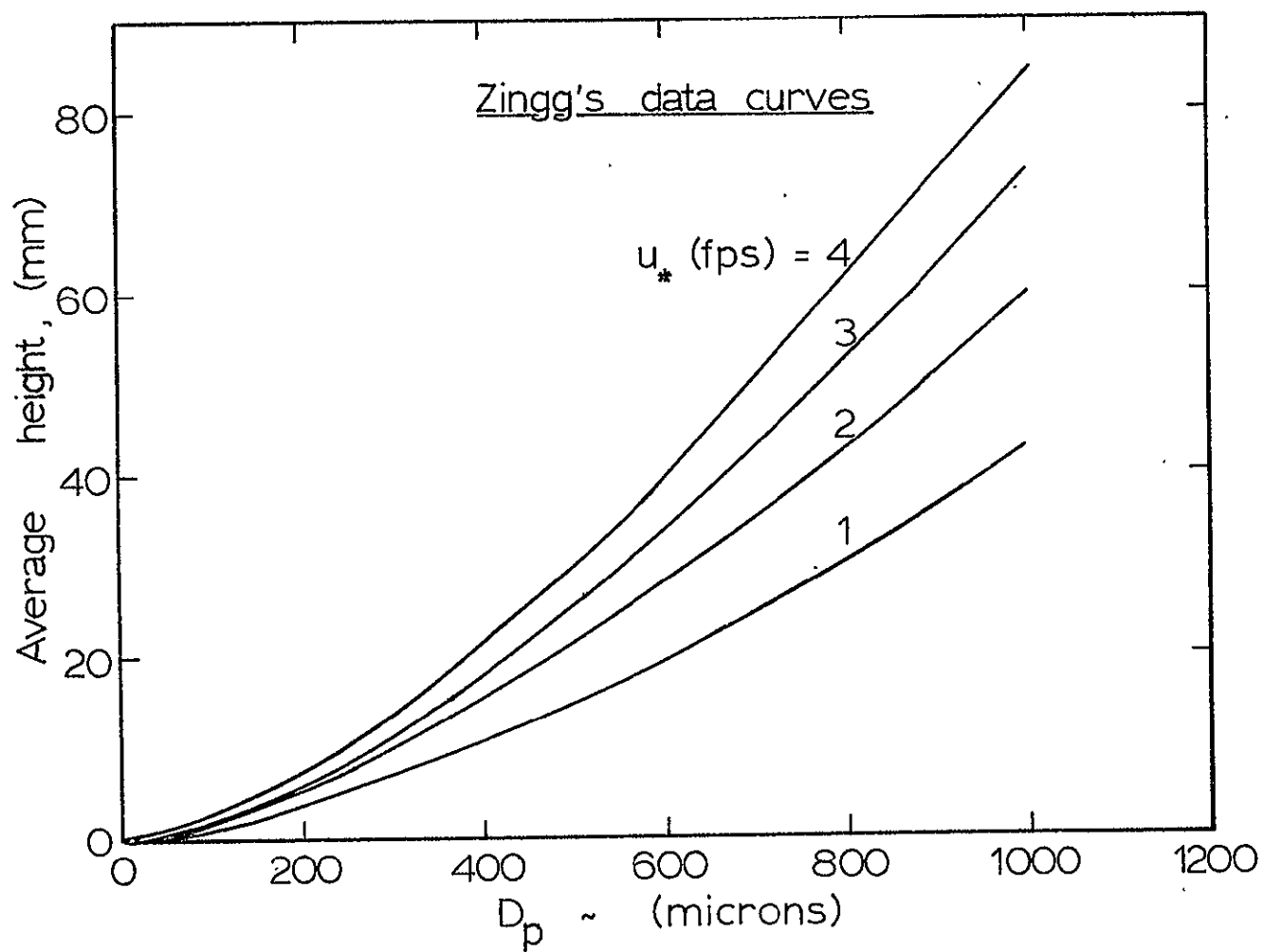
Figure 30. Average trajectory height, from Zingg's empirical relation

> The wall effect acts in two different
> ways. First, the extra drag due to the
> walls will make the particle lag behind
> the fluid; this relative velocity will
> be viscosity independent when the
> viscosity is large, and will depend only
> on the relative size of particle and the
> distance from the wall. Secondly, the
> flow field around the particle is
> altered to the presence of the walls and
> the inertial effects will differ from
> those for a particle in an unbounded
> flow, especially when the particle is
> near the walls.

This altering of the flow around a particle will also affect
the lift on the particle. The flow will be slower on the side
of the particle nearest the wall and this change in the flow
field will create a new pressure distribution on the particle.
The pressure will be significantly higher on the under side of
the particle thus effectively making the lift force much
higher than normally predicted for flow in the absence of the
wall. The lift and drag forces have the net effect of
creating initial vertical motion, then turning the particle's
motion to the direction of the stream. This phenomenon of a
particle leaving the surface nearly vertically has been
observed by the author and previously by others. It was
assumed that the lift force for a turbulent boundary layer
with a laminar sublayer acts only in the sublayer region. The
laminar sublayer was then broken into two regions. The first
region is the one nearest the wall where the wall effects are
included in the lift force function empirically. The second
or outer region does not include the wall effect. For Earth

the wall effect was empirically simulated by allowing a region of high lift force to act from a height of one-half the particle diameter to a height equal to the particle's diameter. The analytic derivation of the wall effect on drag force was performed by Goldman et al. (1967) and O'Neill (1968). O'Neill (1968) obtains an exact solution of the linearized Stokes flow equation derived for a viscous flow about a fixed sphere in contact with a plane for uniform linear shear flow if the sphere were not present. The sphere's forces are calculated explicitly. Goldman et al. (1967) in an earlier paper obtained an exact solution to Stokes equation for the translational and rotational velocities of a neutrally bouyant sphere moving close to a plane wall for uniform linear shear flow if the sphere were not present.

The empirical expressions for lift used were:

$$L = 15.71 \rho u_*^3 D_p^3 / \nu \qquad \text{for} \quad \frac{1}{2} \leq \frac{z}{D_p} \leq 1 \qquad (6.2)$$

and

$$L = 1.615 \rho u_*^3 D_p^2 \, z/\nu \qquad \text{for} \quad 1 < \frac{z}{D_p} \leq \frac{10\nu}{D_p u_*} \qquad (6.3)$$

A velocity profile of

$$\frac{u}{u_*} = \frac{u_* z}{\nu} \qquad (6.4)$$

was used for the laminar sublayer region and a velocity profile of

$$\frac{u}{u_*} = \frac{1}{k} \log \left(\frac{z u_*}{\nu} \right) + 5.5 \qquad (6.5)$$

used for the turbulent portion of the boundary layer.

Unfortunately, the laminar sublayer height $10\nu/u_*$ is smaller than nearly all of the particle diameters calculated and thus the friction Reynolds number is that of flow for transition. In order to obtain a laminar sublayer solution to be later used in asymptotic matching of laminar flow to turbulent flow the length of the range of the second region was increased from $10\nu/D_p u_*$ to 10, i.e.

$$L = 1.615 \ u^3 D_p^2 z/\nu \qquad \text{for} \qquad (1 \le \frac{z}{D_p} \le 10) \qquad (6.6)$$

Recalling Saffman's statement that the wall effect depends only on the size of the particle and distance away from wall, Equation 6.6 should be approximately valid. To assume a constant distance that depends only on the particle diameter may not be correct for the fully turbulent flow where simple shear flow no longer exists.

The above lift force was substituted in the equations of motion and again the maximum heights calculated were all found to be less than 1 cm high. This does not agree with Zingg's experimental data. In Saffman's original work the lift was in error by a factor of 4π which he later corrected in 1968. The above lift force in both the wall effect region and the outer layer of the laminar sublayer were then increased by a factor of 4π to match the lift forces predicted by Saffman's original work. The results of this modified lift force are given in

Figure 31.

Figure 31 shows a plot of the calculated maximum height
z_{max} versus the particle diameter for the latter case (for
lift force in the second region of the sublayer as described
above). Of course these calculations are probably in error
for the case where a laminar sublayer does not exist but will
be utilized to approximate a solution in the transition region
between the sublayer case and the fully turbulent one. Four
different friction speeds, $u_* = 4$, 3, 2, and 1 fps are shown.
The region of small particle diameter ($D_p < 300$) is to be
considered more valid than the range of larger particle
diameter ($D_p > 300$). These curves also exhibit a decreasing
z_{max} with increasing particle diameter size for a constant
value of friction speed. They show a rapid increase in z_{max}
for a range of D_p from 50 microns to 300 microns.

Figure 32 shows the same type plot with the exception
that the particle density is varied and the friction speed has
a constant value of $u_* = 2$ fps. The trend in this plot is
for lower density particles to rise higher under identical
conditions than those for heavier particles. This trend is
opposite to that of the case where no lift force exists and
force motion is created by setting $w_o = u_*$, where the heavier
density particles went higher under identical conditions
(since they have more momentum). The trend of lower density
particles rising higher in Figure 32 seems conceptually valid.
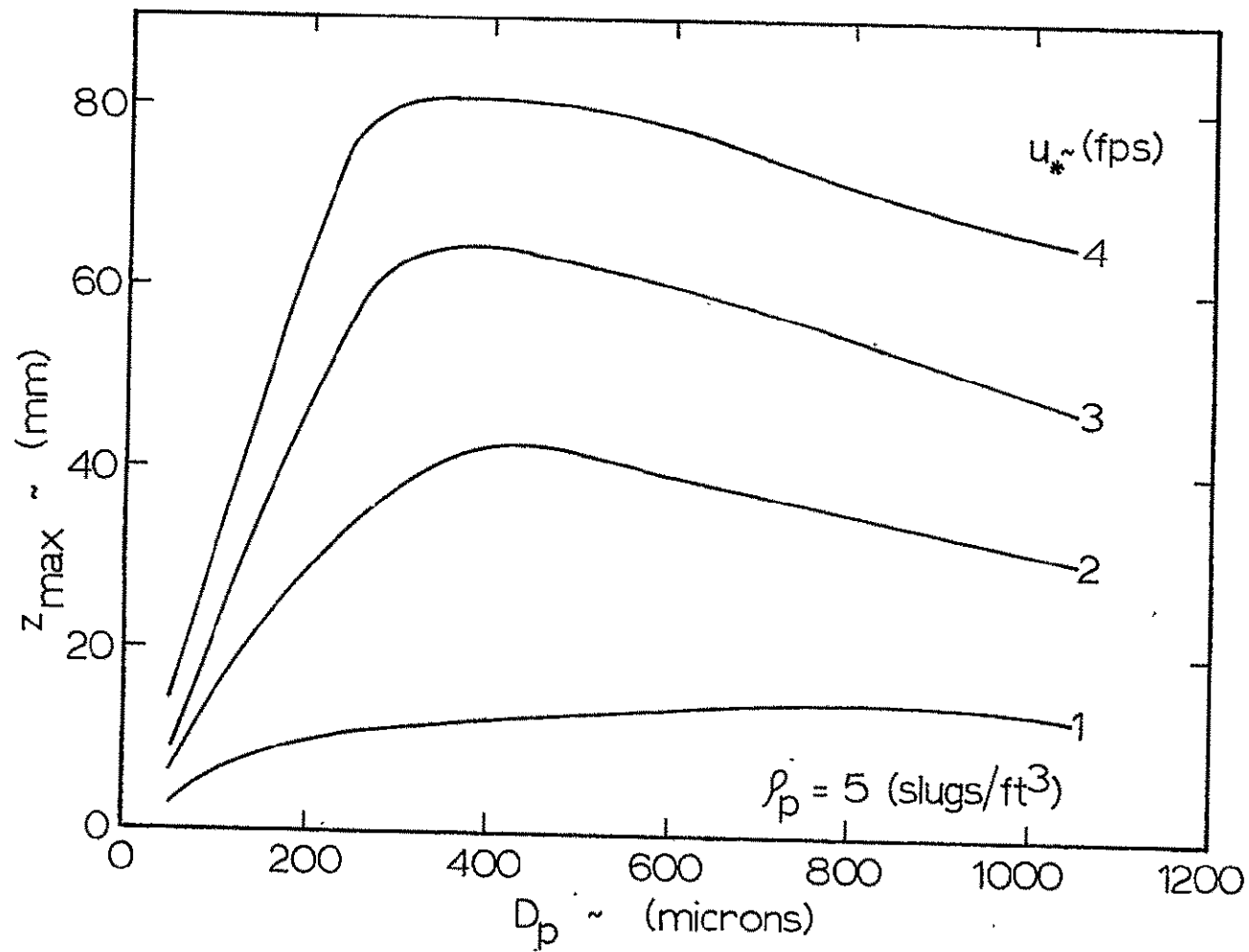
Figure 31. Maximum trajectory height for Earth, effect of friction speed (laminar sublayer)
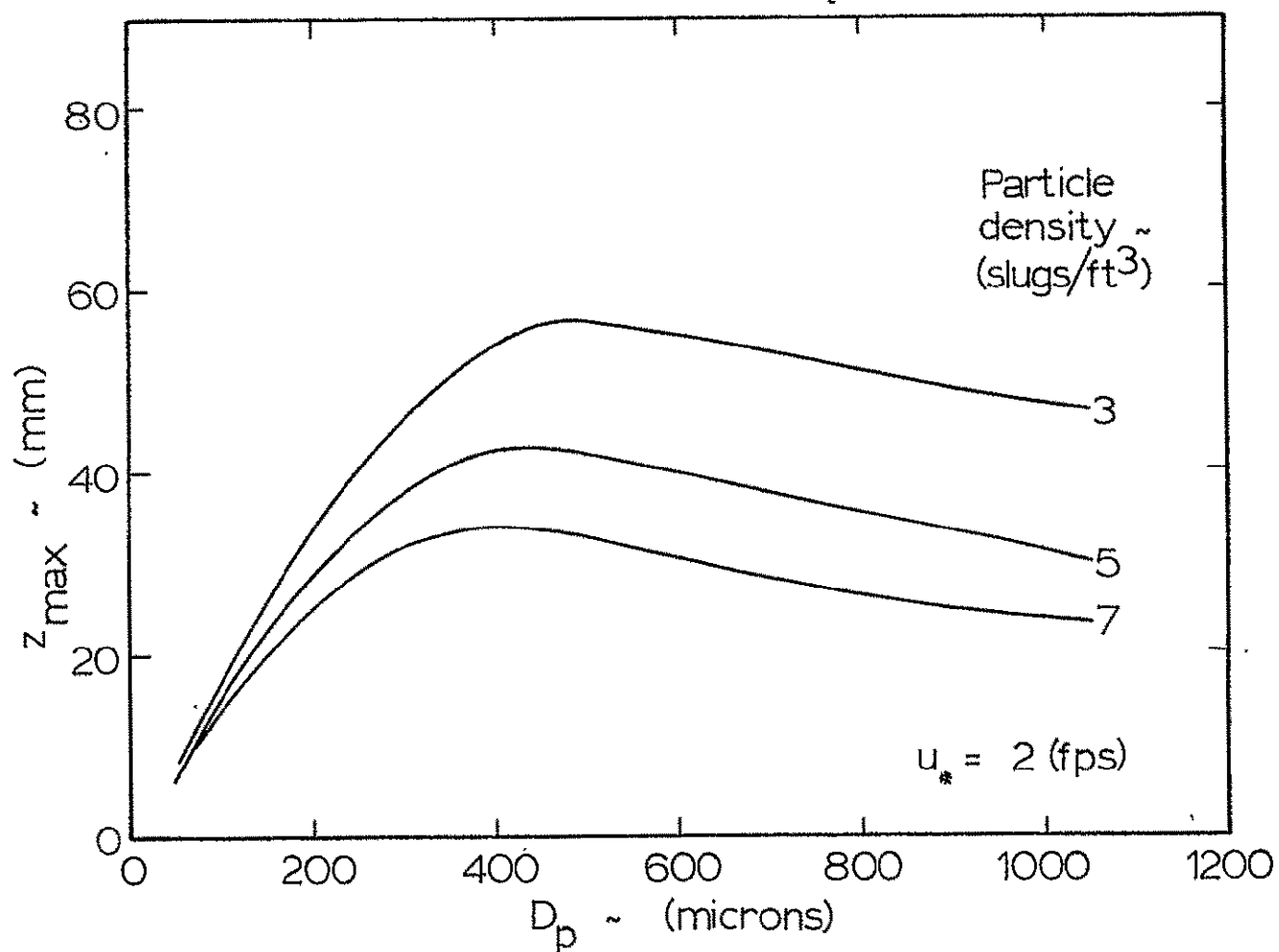
Figure 32. Maximum trajectory height for Earth, effect of particle density (laminar sublayer)

Figure 33 exhibits the dimensionless maximum vertical velocity ratio w_o/u_* versus the particle diameter for the corresponding curves of Figures 31 and 32. Plausible trends are displayed in these plots. Here the value of initial dimensionless vertical velocity w_o/u_* decreases with increasing particle size which has to occur to meet threshold conditions for the large particles. These trends show a rather large ratio of w_o/u_* for larger particles ($D_p > 400$ microns) which is a result caused by the large extent to which lift was allowed to act (up to $z = 10D_p$), which is larger than the laminar sub-layer would be if it could exist. This may, however, better approximate a particle initially at rest in a region of higher surface roughness, z_o.

3. Case of lift function for fully turbulent boundary layers

The lift force and coefficient developed for a fully turbulent boundary layer flow in section V was substituted in the equations of motion and a velocity profile of

$$\frac{u}{u_*} = \frac{1}{k} \log(30z/D_p) \qquad (6.7)$$

used, where the roughness height is

$$z_o = D_p/30 \qquad (6.8)$$

The resulting trajectories were again low in comparison to experimental data. The lift coefficient was increased by a factor 4π, i.e.,
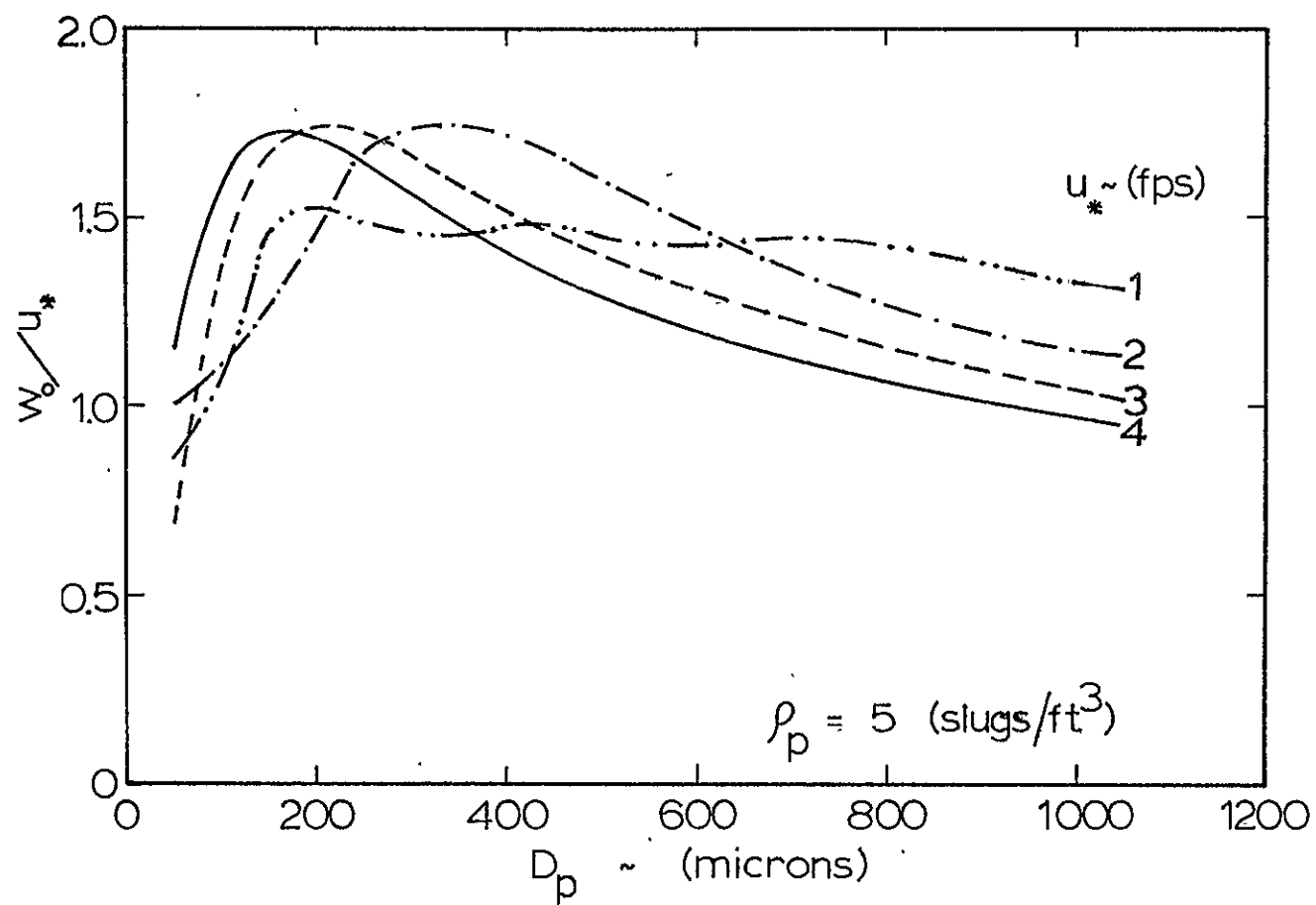
Figure 33. Maximum vertical velocity for Earth, effect of friction speed (laminar sublayer)

$$C_L = 32.48[(u_*z/\nu)\log(30z/D_p)]^{-1/2} \qquad (6.9)$$

Figure 34 displays the resultant calculations of maximum height z_{max} versus the particle size D_p using the above lift coefficient. The calculated maximum heights are larger than that of the laminar sublayer flow of Figure 31. The curves show a sharp decrease of z_{max} for increasing D_p ($D_p > 400$) which must exist if threshold data are to be satisfied. These curves (for constant u_*) probably are incorrect for the smaller particles where a laminar sublayer would exist. The flow for the majority of these curves in the transition region and the calculated values would not be expected to identically represent the physical process. However, in the transition region especially at large friction Reynolds numbers the flow resembles the characteristics of turbulent flow more so than laminar flow. For friction Reynolds number greater than 70 the trends the solution exhibits would be expected to be valid although the relative values might not be exact since neither analytical nor empirical values of lift coefficient in the transition and fully rough regions are known.

Figure 35 shows a plot of z_{max} versus D_p for a constant value of $u_* = 2$ fps for three different particle densities, $\rho_p = 3, 5, 7$ slugs/ft^3. Again the lighter material obtains a higher z_{max} than that of a heavier density particle under identical conditions. This shows that lighter materials are
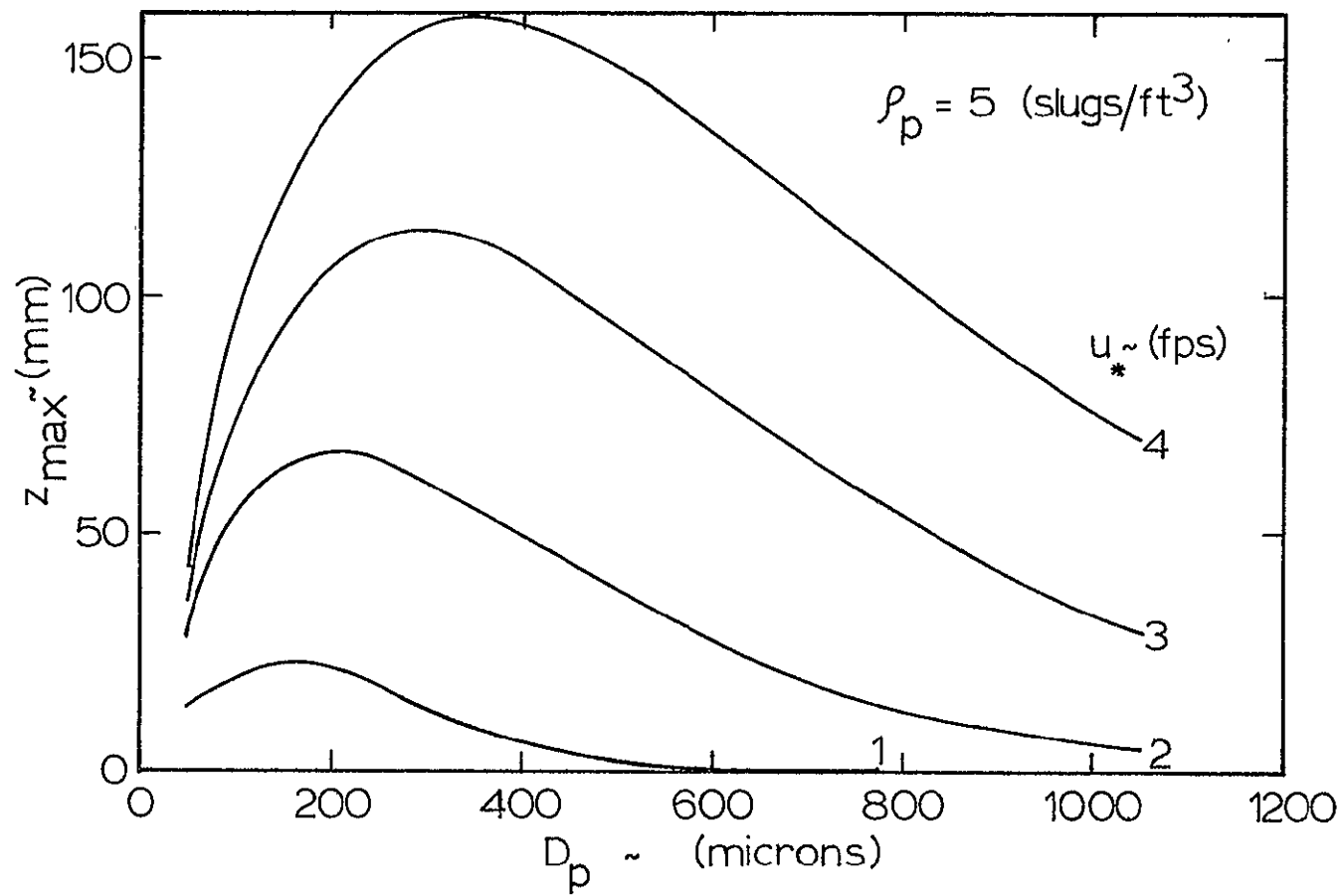
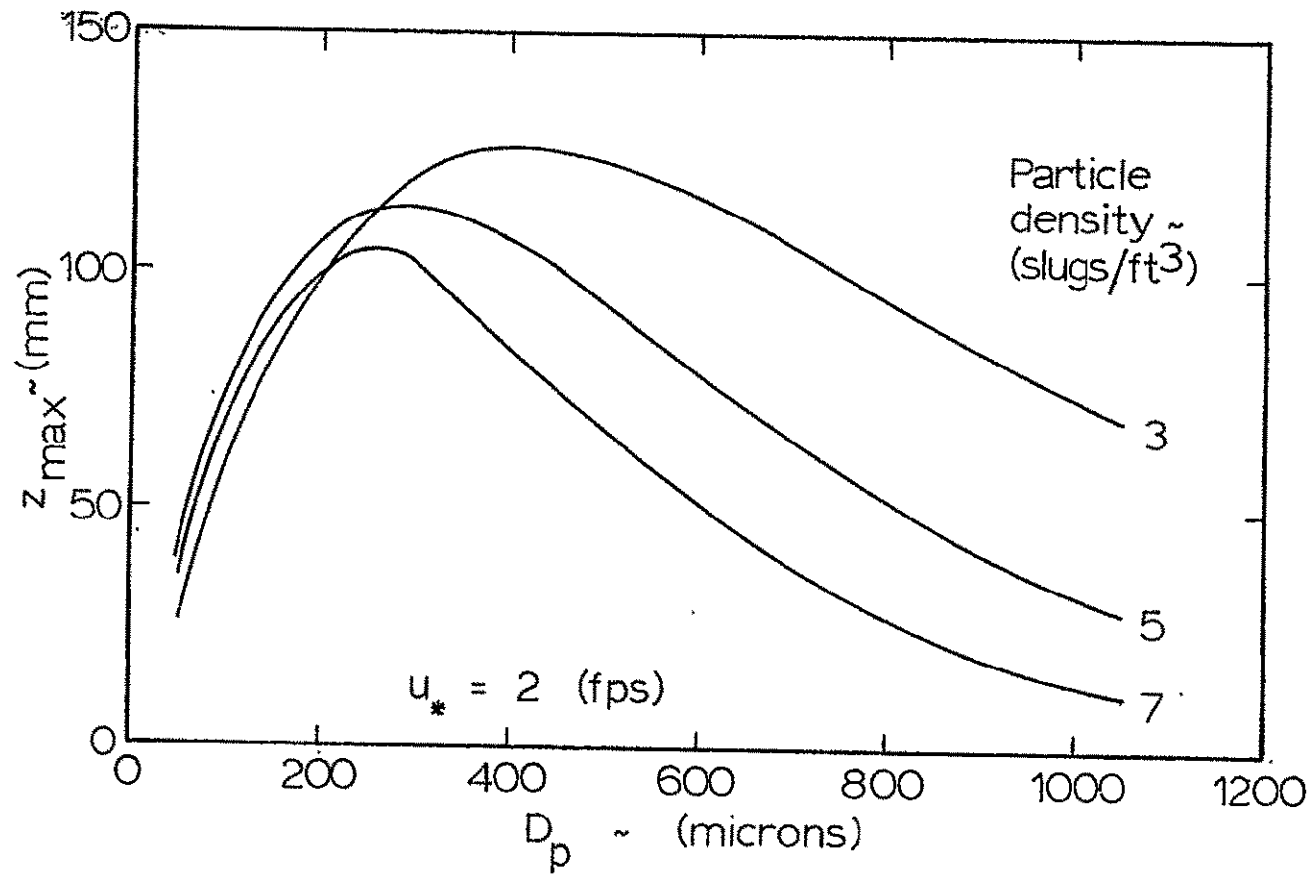Figure 34. Maximum trajectory height for Earth, effect of friction speed (fully turbulent)

Figure 35. Maximum trajectory height for Earth, effect of particle density (fully turbulent)

much more susceptible to gusts of wind and the lighter material is the first to move with an increasing wind speed. With decreasing densities of material under a constant set of conditions the particle goes higher than normally would be expected for the denser material.

Figure 36 records the maximum vertical components of velocity divided by the friction speed versus particle diameter. Here the trends agree with that of Figure 33 but a sharp decrease with increasing particle diameter is noted. This conceptually seems more plausible, as the larger the particle the slower would it lift off under similar conditions. The values of the velocity ratio of larger particles ($D_p > 500$) have a range from 0.5 to 1.0 for the friction speed $u_* = 4$. This is more realistic than the higher values displayed in Figure 34.

4. Composite results of laminar and turbulent flows

Although the majority of points calculated in the fully turbulent boundary layer are actually in the transition region the solutions to the particle motion are a better approximation than that of the laminar sublayer for reasons discussed earlier. With the laminar sublayer and turbulent flows known for the same set of initial conditions a composite curve of z_{max} versus D_p may be made assuming the solution exists somewhere between the laminar and turbulent cases and
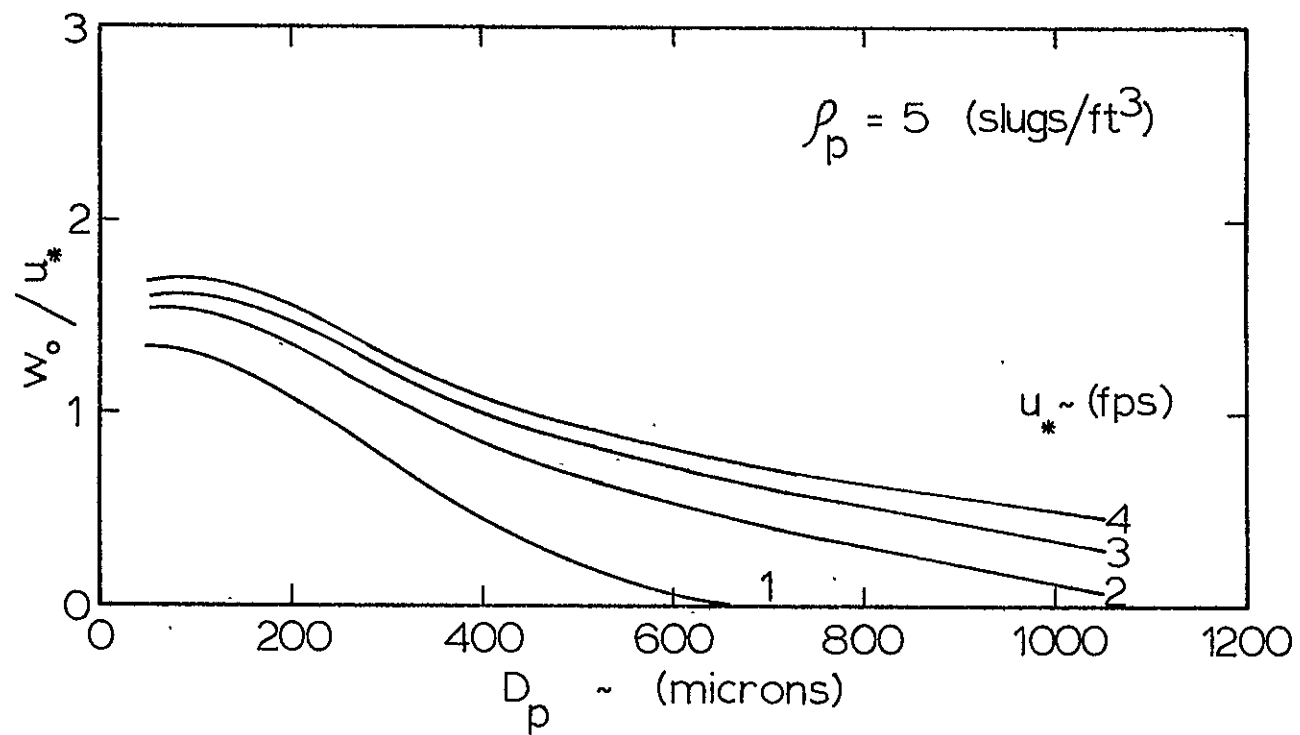
Figure 36.   Maximum vertical velocity for Earth, effect of friction speed (fully turbulent)

144a

and asymptotically meets each other as flow turns from completely laminar to transition and from transition flow to fully turbulent flow.

Figure 37 is such a plot which displays the solution for a fully turbulent boundary layer and one with a laminar sublayer for a constant value of friction speed u_* equal to 2 fps. Also displayed in the figure are the curves for Zingg's experimental data and for the case where no lift force acts on the particle, but motion is produced by giving the particle an initial vertical velocity component of $w_o = u_*$. Zingg's experimental points are also shown in the figure as hollow circle symbols. The single solid circle symbol that lies on the ordinate axis is the empirically determined threshold value and thus the curve of z_{max} versus particle diameter D_p must reach zero at this particle diameter.

For lower particle diameters the laminar sublayer solution should be valid at least up to the particle diameter size that corresponds to the upper limit of the particle friction Reynolds number (R_f) range for laminar sublayer existence. In this case that is a D_p of 250 microns which has a corresponding R_f of 10.935 which is in the lower end of the transition range. At larger values of D_p the correct solution for the transition region should asymptotically match the fully turbulent case at a R_f of approximately 70. The largest R_f obtained in this plot is for a D_p of 1050 microns which corresponds to $R_f = 45$, thus
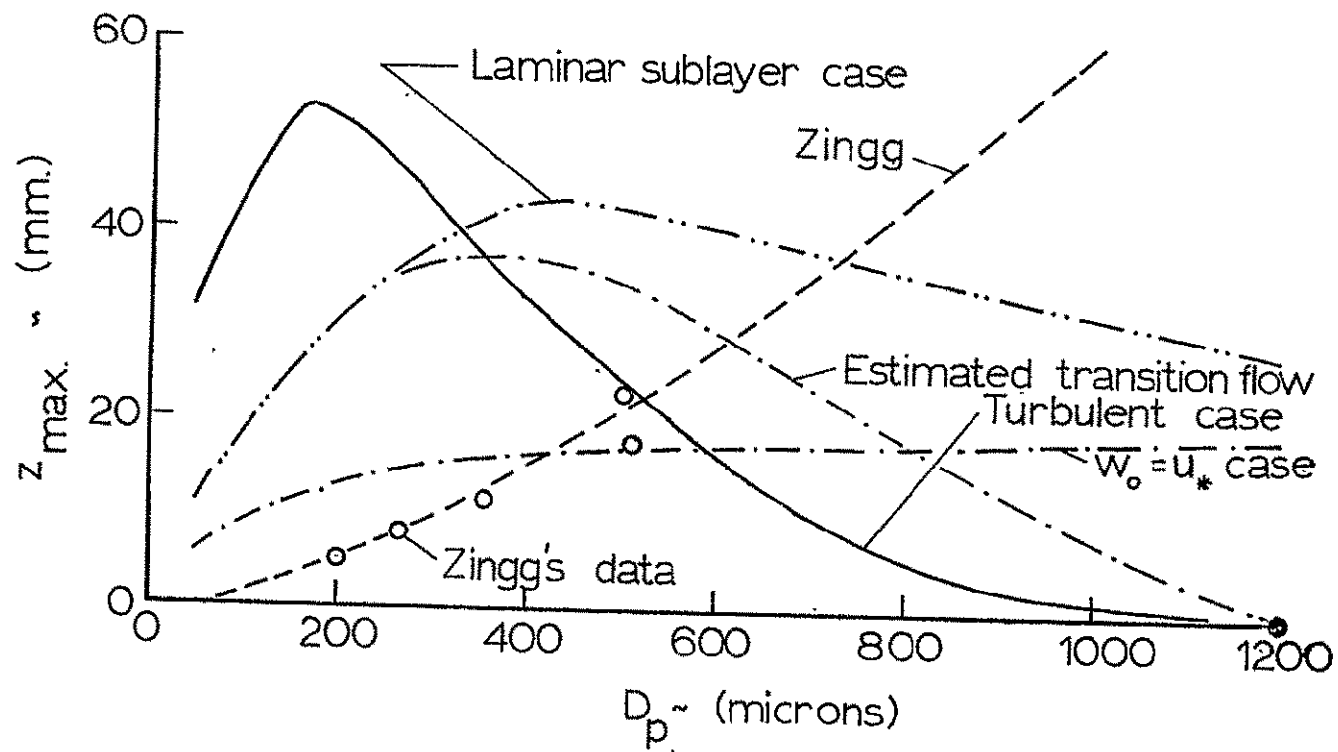
Figure 37. Maximum trajectory height for Earth, comparison for solution and experiment and estimated transition interpolation

the interpolated solution for the transition region would be expected to meet that obtained for the fully turbulent boundary layer at $R_f = 70$. The dashed-dotted line is the interpolated solution for the transition range that approaches the laminar sublayer calculation at $D_p \cong 250$ microns (corresponding to $R_f \cong 5$). It would approach the fully turbulent boundary layer solution at $R_f = 70$ but does not reach it in this case since threshold conditions occur in the transition region.

Although the final estimation of the z_{max} versus D_p curve lies above the experimental data points of Zingg, the solution appears to be valid since Zingg's experimental points represent intermediate positions from one-half the maximum height to the maximum height as discussed earlier. Thus the estimated curve has the proper shape to compare favorably with experimental points and also to obey threshold conditions. This basic trend of increasing z_{max} for smaller D_p and obtaining a maximum z_{max} for some optimum particle size and then z_{max} decreasing with increasing D_p to the threshold condition appears to be conceptually correct. All 167 separately calculated cases have identical trends and same shaped curves but this particular case was selected to exhibit the experimental data of Zingg. In many of the cases calculated, unlike the above example, the solutions do extend into the fully turbulent region instead of only the transition region as above. The shape of the curve remains the same and continues to retain all of the above

characteristics. In particular, interpolated curves for the transition region are made to asymptotically match the solution of the fully turbulent region.

5. Effect of turbulence on particle trajectories

The effect of turbulence on a particle trajectory was accounted for in the equations of motion and solved numerically. The model of turbulence used was to assume that the streamwise component of velocity obeyed the time averaged velocity profile of Equation 6.7 and the vertical component of velocity had a cyclic velocity distribution. The cyclic vertical fluctuating velocity had an absolute maximum value of 1.1 times the friction velocity, e.g.,

$$w' = 1.1 \ u_* \ \sin \omega t \tag{6.10}$$

where ω represents the angular velocity of the vortex eddies. The representation of ω was taken from Panofsky and McCormick (1960),

$$\omega = \frac{7.25 \ u_*}{z} \ \log \left[\frac{z + z_0}{z_0} \right] \tag{6.11}$$

where the roughness z_0 is assumed equal to $D_p/30$.

$$\omega = \frac{7.25 \ u_*}{z} \ \log(1 + 30z/D_p) \tag{6.12}$$

Therefore,

$$w' = 1.1 \ u_* \ \sin\left[\frac{7.25 \ u_*}{z} \log(1 + 30z/D_p)t\right] \qquad (6.13)$$

This expression of w' was incorporated in the equations of motion for the fully turbulent Earth boundary layer Equation 6.9 and the motion of a particle calculated.

The results of the calculations show that turbulence plays a minor role in the particle's motion ($D_p \geq 100$ microns). For example, the calculated trajectory for a particle diameter of 100 microns with a friction speed $u_* = 2$ fps and $\rho_p = 5$ slug/ft^3 shows only a 3.5% increase (with respect to the w' = 0 calculation) in the calculated z_{max} and only a 1.1% increase in the final velocity of the particle u_F. Since the case of 100 micron particles would be far more susceptible to the effects of turbulence than larger particles this would indicate that turbulence plays a minor role in altering the particle's path. An exception to this generalization is when the friction speed u_* is of the same order of magnitude or greater than the terminal speed of a particle. Turbulence then completely dominates the particle motion and the particle is then said to be in suspension.

To extrapolate the above results to the case of Mars would be very hazardous since the basic structure of the Martian boundary layer is not known at the present time and also for nearly all conceivable flow conditions a rather large

laminar sublayer would exist. In the laminar sublayer the effect of turbulence is negligible and therefore the particle would only be affected by turbulence outside of the laminar sublayer. At these heights the velocity of the particle is relatively high in comparison to the estimated turbulent fluctuations and therefore need not be included in the calculation (at the risk of an approximate 4% error). Thus, the effect of turbulence in the Mars calculation was not felt to be of importance in accurate solution of the particle path and was not included in the calculations. Also the computer calculating time for the turbulent condition increased by a factor of 10 times over that for flow without simulated turbulence.

B. Two-dimensional Calculation of Particle Trajectories under Mars Surface Conditions

The numerical solutions obtained for the Mars surface conditions were performed in a similar fashion as those calculated for Earth with the exception of a fully turbulent boundary layer case which was not calculated. All cases calculated for Mars have a friction Reynolds number R_f less than seven and a laminar sublayer exists for all of these cases. It was necessary to consider slip flow around the particle caused by the rarefied atmosphere of Mars. The numerical coefficients used for these calculations as well as the different variables used in the calculations are given in

Table 3.

The values of friction speed u_* were selected by approximately matching the ratio of flow friction speed to that of threshold, u_*/u_{*_t}, to that of the cases calculated for Earth. These calculated values of u_{*_t} were taken from the work of Iversen et al. (see Section III) and are presented in Table 4. It was assumed that a similar range of particle densities existed on Mars as on Earth, as well as a similar range of particle size distribution. The atmospheric density was taken from the work Iversen et al. (1975a).

1. Case of no lift force

The dimensionless equations of motion were solved for an initial upward vertical component of velocity equal to one-tenth and one-twentieth of the prevailing friction speed u_*. These values of initial upward velocity were calculated from trajectory calculations with lift and from the work of Bagnold (1941) in which he assumes the quantity $(u_F w_o/g y_{max})$ is a constant for any universal set of conditions. These values of w_o were also supported by numerical calculations for the laminar sublayer case.

Figure 38 displays a plot of z_{max} versus D_p for the no lift force case with w_o set equal to one-tenth u_*. Similar trends as those calculated for Earth with no lift force present are observed. Here the turbulent boundary layer with a laminar sublayer velocity profile was used. This plot is for a

Table 4. Threshold friction speeds (fps)

	Earth			Mars		
ρ_p (slug/ft^3)	3	5	7	3	5	7
D_p (microns)						
50	0.531	0.686	0.700	9.024	9.578	10.095
150	0.540	0.698	0.826	7.464	8.757	9.808
250	0.698	0.901	1.066	7.666	9.164	10.344
350	0.826	1.066	1.261	7.93	9.60	10.865
450	0.936	1.209	1.430	8.23	10.05	11.445
550	1.035	1.336	1.581	8.53	10.465	12.02
650	1.125	1.453	1.719	8.78	10.85	12.56
750	1.209	1.560	1.846	9.04	11.22	13.11
850	1.287	1.661	1.965	9.29	11.60	13.61
950	1.36	1.756	2.078	9.52	11.93	14.06
1050	1.43	1.846	2.184	9.75	12.24	14.48

constant particle density of ρ_p = 5 (slugs/ft^3).

It might be noted that similar trends to those discussed earlier (Earth case of no lift, $w_o = u_*$) for changing particle density also are present in these calculations and the same analysis can be applied to these as was done to the Earth case. Recall that the main point made earlier was that the trend of
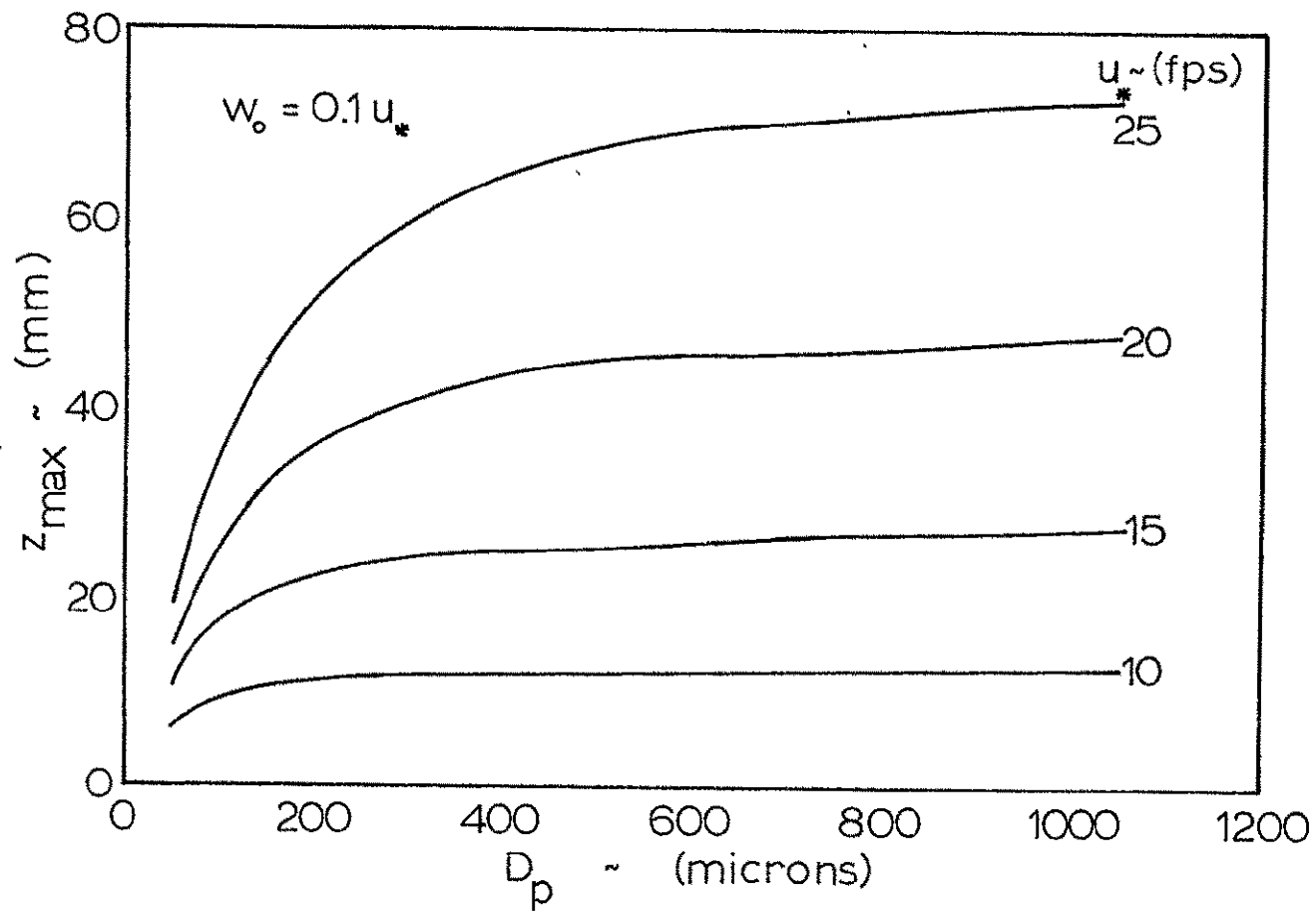
Figure 38. Maximum trajectory height for Mars, no lift, $w_o = 0.1\ u_*$

heavier density particles lifting off higher than those of lighter density for identical conditions is incorrect. The $w_0 = $ constant calculations are thus used only to gain insight to the overall transport process. It might be noted that in comparison to Figure 29 (the Earth case) that the Earth curves fall off much more quickly at the smaller particle size than that of Mars. An apparent explanation of this phenomenon is the slip flow effect of Mars. Even though the w_0 on Mars is much smaller (on the order of 10% of Earth's) the shape of the calculated curves and their trends should be similar to Earth with the exception of the effect of slip flow.

The effect of slip flow can be observed in Figure 30, where the plot shows z_{max}/D_p versus D_p for ρ_p equal to 5 (slugs/ft^3) and $w_0 = 0.1\ u_*$ (with no lift force) for a friction velocity $u_* = 25$ fps. The solid line represents the solution of the equations of motion including the slip flow effect of C. N. Davies (1945). The dashed line displays the solution for continuum flow (no rarefied gas effects included). There appears to be very little difference in the solution down to a particle diameter of approximately 250 microns. The effect of slip flow drastically increases for 50 micron diameter particles. This effect is identical for all cases of Mars calculated since the effect of slip flow is independent of the lift mechanism employed to particle motion. Therefore, it will suffice to examine closely only one case of the effect
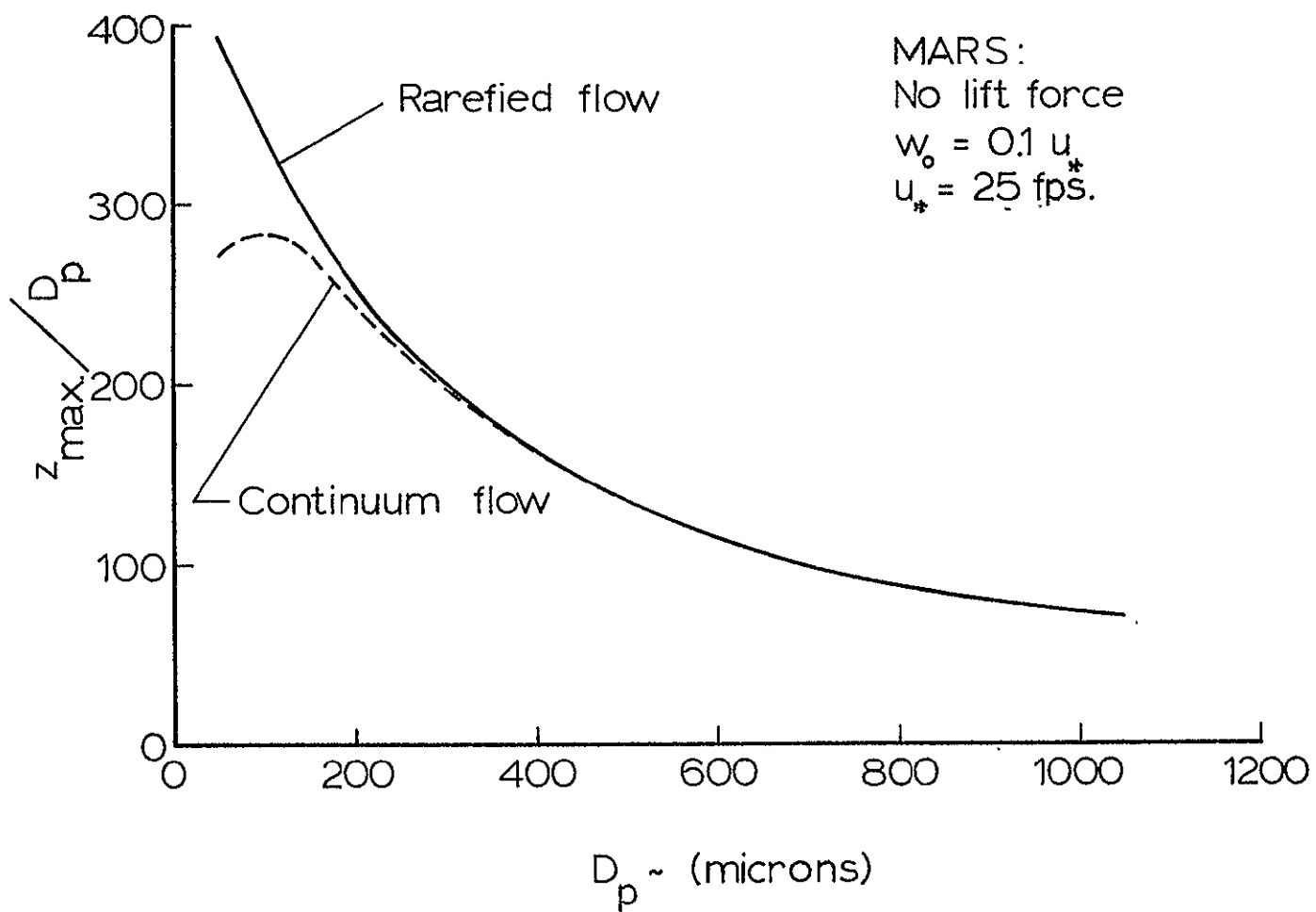
Figure 39. Maximum trajectory height for Mars, effect of slip flow in a rarefied atmosphere

154

of slip flow compared to continuum flow as was done here.

Figure 40 shows the relation between z_{max}/D_p versus D_p curves for $w_o = 0.1\ u_*$ and $w_o = 0.05\ u_*$. Each trajectory was calculated with identical conditions (with the exception of initial velocity) which were $u_* = 25$ fps and $\rho_p = 5.00$ slugs/ft^3. The figure displays similar trends and only the magnitude of the curve is increased for increasing initial velocity. As the initial momentum is increased, the particle maximum energy or height will also increase. The validity of one curve over the other curve in Figure 40 remains unknown but a numerical investigation of the case of a lift present in the laminar sublayer region with the initial vertical and horizontal velocity set equal to zero will indicate which curve in Figure 40 more closely represents the trends exhibited by the solution of the equations of motion for a lift force present.

2. Case of lift function for turbulent boundary layer with a laminar sublayer

The analytically derived lift coefficient function (see Equation 4.41) based on Saffman's (1965, 1968) work was used in the solution of the equations of motion. The solutions (as in the Earth case) of the particle's motion resulted in very low z_{max} and are not believed by the author to be valid. Consequently, the factor of 4π was applied to the lift coefficient and the equations solved again. This is the same process or technique that was used in the Earth calculations
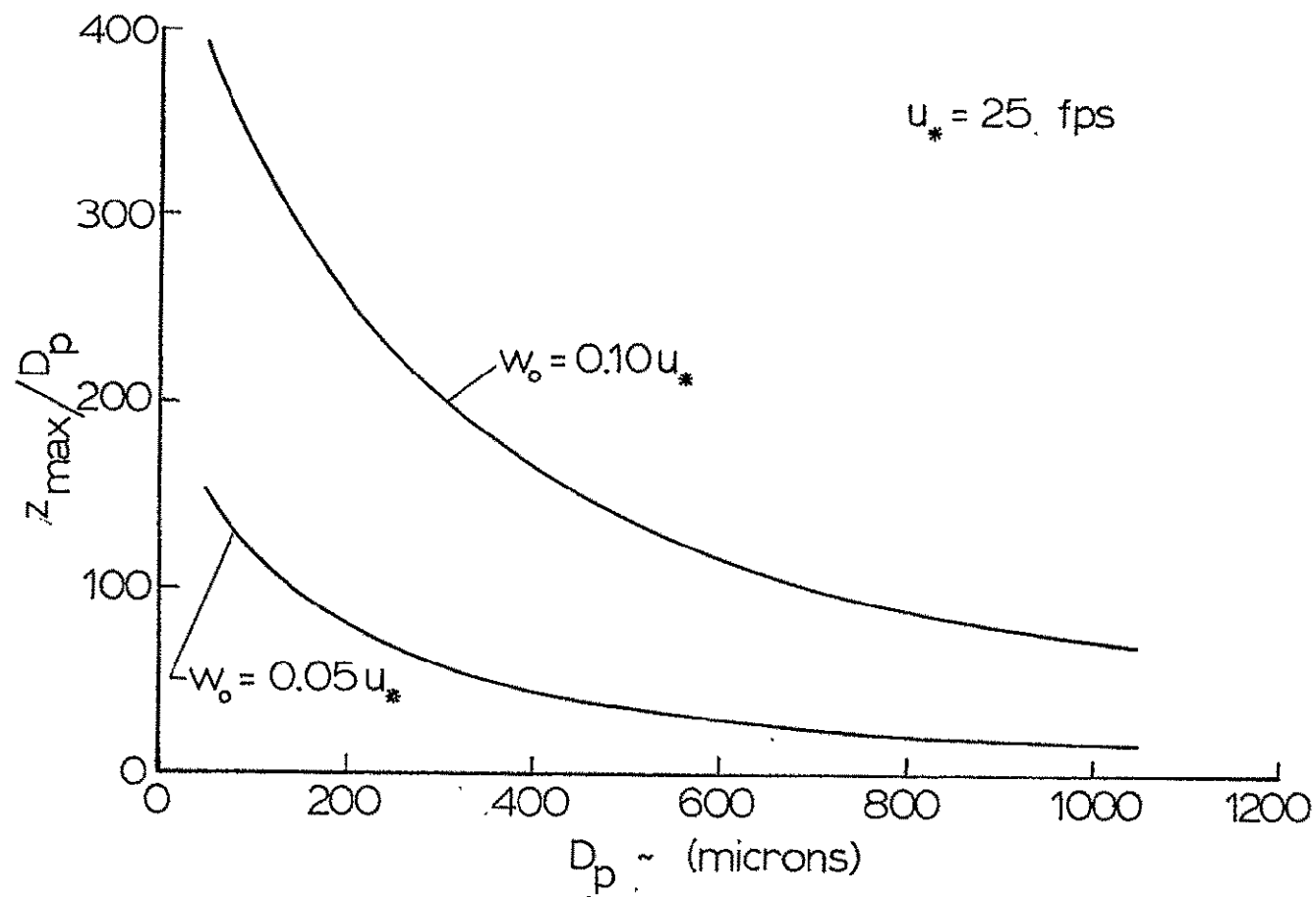
Figure 40. Maximum trajectory height for Mars, no lift, $w_o = 0.1\ u_*$ and $w_o = 0.05\ u_*$

and is believed to be as valid for these calculations (Mars) as it was for the Earth. Essentially this states that the solutions obtained in the Mars calculation should be of the same order of accuracy as the solutions of the Earth case. Recall that the Earth solution was definitely within an order of magnitude of related experimental data and believed to have a valid and accurate trend in analysis of the experimental data of Zingg (1953) and supporting threshold work of Iversen et al. (1975a). Therefore, extending this analysis, the Mars calculations should be of the same order of magnitude as the physical situation and quite possibly would describe the particle motion very accurately. Of course, these claims can not yet be supported by experimental data or visual observation.

A velocity profile for the viscous laminar sublayer and the turbulent portion of the boundary layer were the same as Equations 6.4 and 6.5, with the appropriate values of Mars used for the various constants.

Again as for Earth, the sublayer was broken into two regions; one accounting for the wall effect where the lift coefficient was

$$C_L = 41.12 \; D_p \nu / u_* z^2 \qquad \text{for} \qquad \frac{1}{2} \le z/D_p \le 1 \qquad (6.14)$$

and for the second region was

$$C_L = 12.91 \nu / \pi \; \Delta V_r D_p \qquad \text{for} \qquad 1 \le z/D_p \le \frac{10\nu}{u_* D_p} \qquad (6.15)$$

where both of the above are multiplied by 4π. The fully developed equations of motion are presented in Appendix B.

Figure 41 shows the solution of the equations of motion using the above assumptions. This figure displays z_{max} versus D_p for ρ_p equal to 5 (slugs/ft^3) and $u_* = 25$, 20, 15, and 10 fps. The z_{max} calculated here are generally higher than those calculated for Earth recalling that the ratio of u_*/u_{*t} is approximately equal thus making a comparison valid. The trends of the Mars calculations are basically different from those of the Earth calculations and this altering of the curves (for $D_p > 250$ microns) are caused by boundary layer profile differences due to different particle friction Reynolds number R_f. However, no physical explanation of the shape of the curves for larger particles ($D_p > 250$ microns) is offered. The point of interest is the gradually decreasing slope of the curves for larger particles for decreasing friction speed u_*. It is apparent that these curves (for $u_* = 15$ fps) must be returned to the ordinate axis with a further increase in D_p in order to meet threshold conditions predicted by Iversen et al. (1975a). Thus there should be a double peak curve of z_{max} versus D_p. The predicted threshold for 450 microns is 10 fps so the lower curve should appear closer to the dashed line as shown.

An alternate way of presenting the curves of Figure 41 is to normalize the maximum height z_{max} by the particle diameter
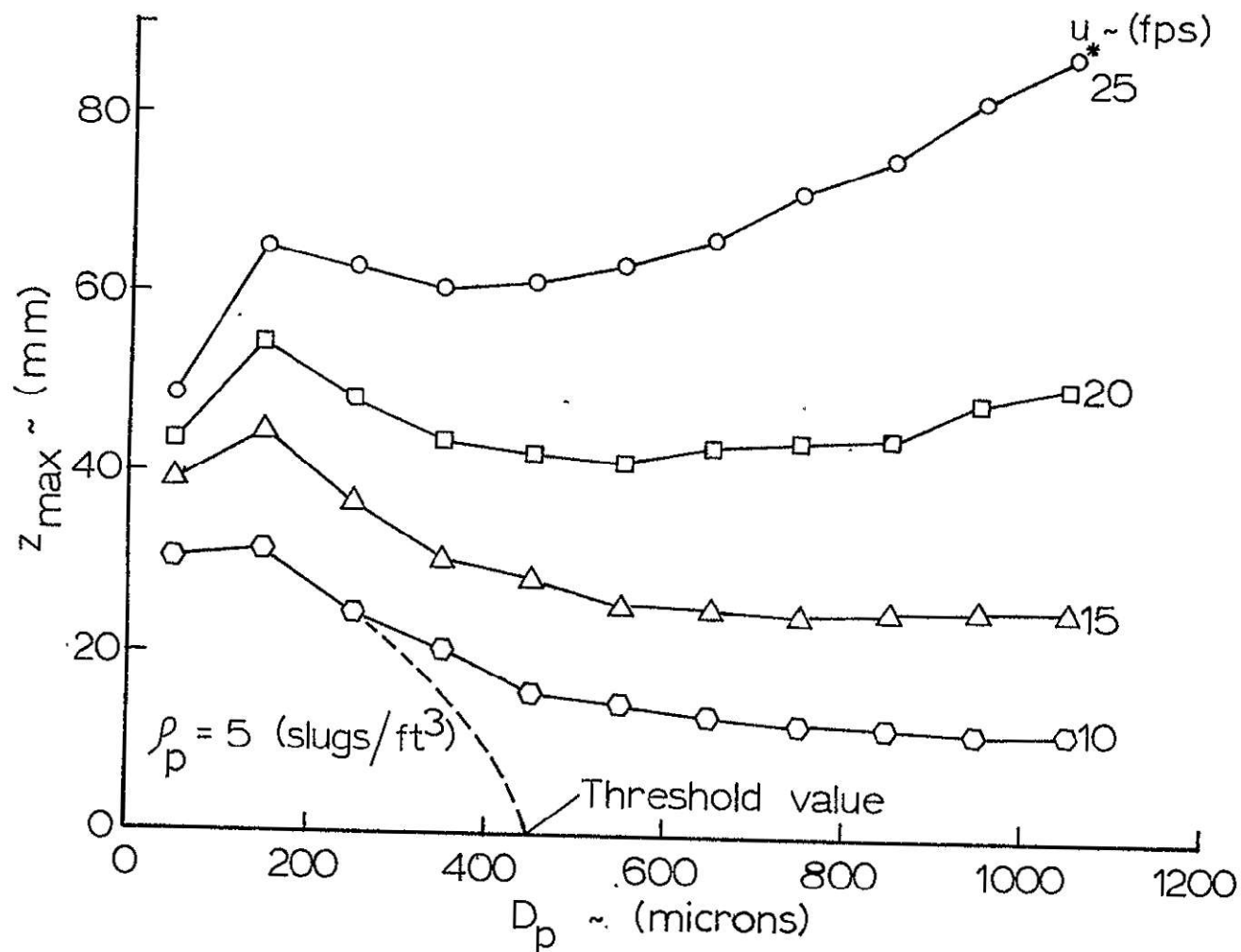
Figure 41. Maximum trajectory height for Mars, effect of friction speed (laminar sublayer)

D_p, e.g. z_{max}/D_p versus D_p. Figure 42 is such a plot of the identical data as presented in Figure 41. The unusual char-acteristics of the curves in Figure 41 disappear and a unique set of curves results. Although the set of curves presented in Figure 41 are nicely defined they may be misleading since the normalizing factor D_p is continually changing which makes relative comparison difficult between different size particle diameters D_p. The dashed line shown corresponds to that of Figure 41.

Figure 43 records a plot of z_{max} versus D_p for a constant u_* of 20 fps and three different particle densities $\rho_p = 3, 5,$ and 7 slugs/ft^3. The trends of these plots are opposite to those of the case of no lift force. The curves of Figure 43 infer that light density material lift off to a higher z_{max} than heavier density material under the same flow conditions. These trends agree with those of the Earth case calculation with a laminar sublayer. The relative increase of z_{max} with decrease of ρ_p is similar to the trends exhibited in the Earth calculations.

Figure 44 shows a plot of w_o/u_* for the corresponding conditions of Figure 42 and 41. It shows a nearly constant w_o/u_* of 0.1 for all friction speeds u_* for D_p greater than 450 microns. An interesting point on the curve is at $D_p = 550$ microns where all w_o/u_* ratios are almost identical. Here all the curves reverse position in relation with each other.
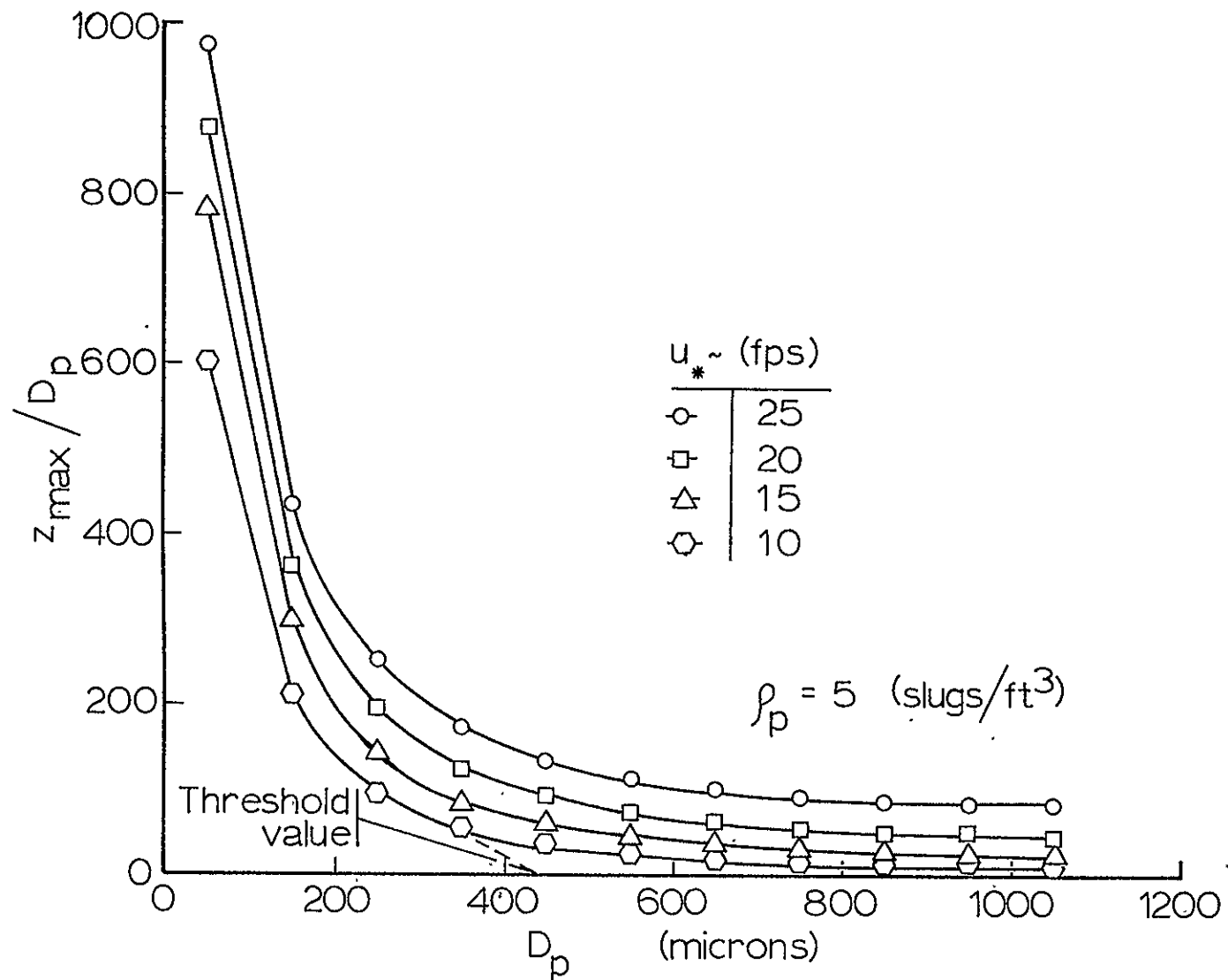
Figure 42. Normalized trajectory height for Mars, effect of friction speed (laminar sublayer)
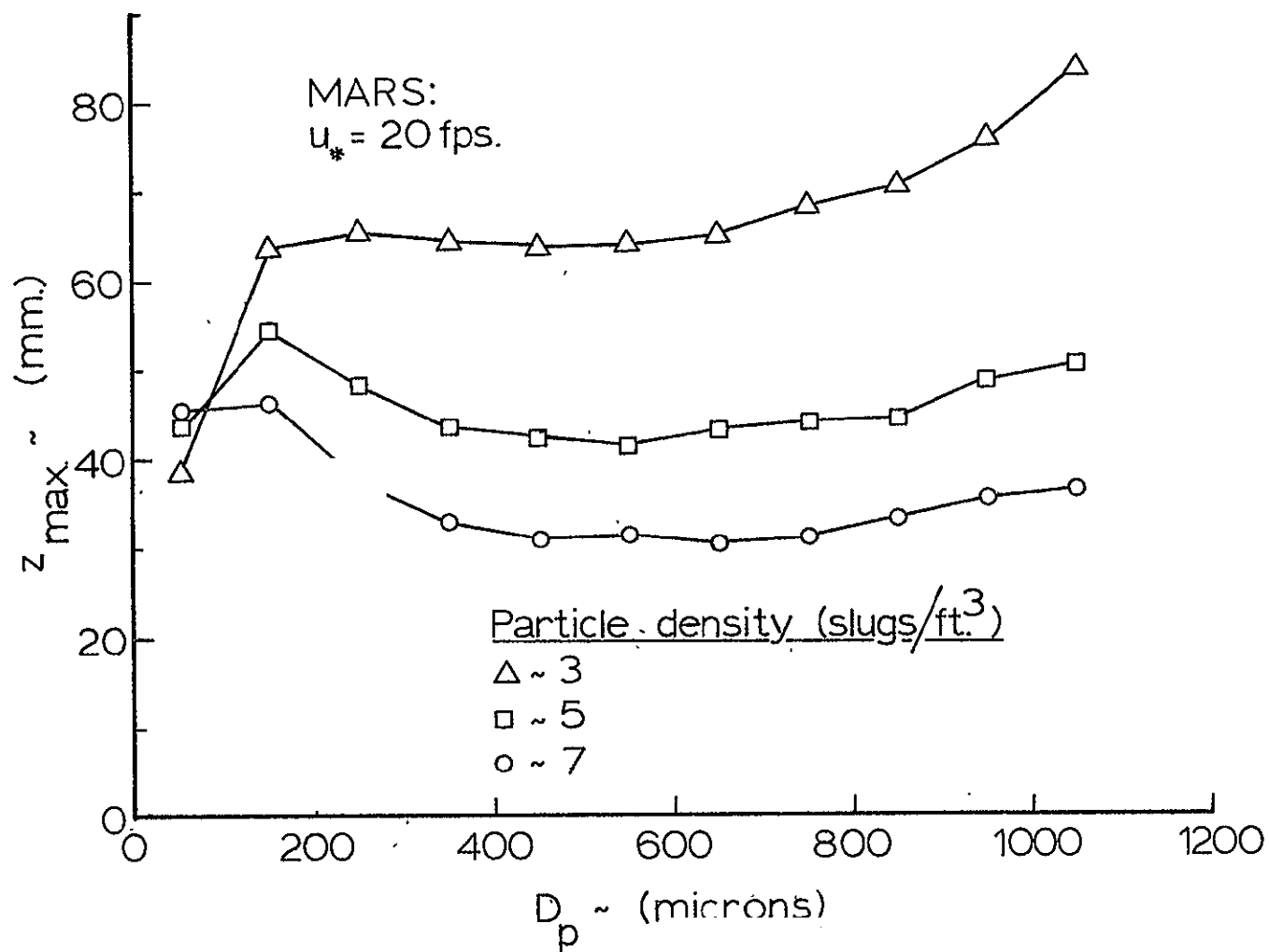
Figure 43. Maximum trajectory height for Mars, effect of particle density (laminar sublayer)
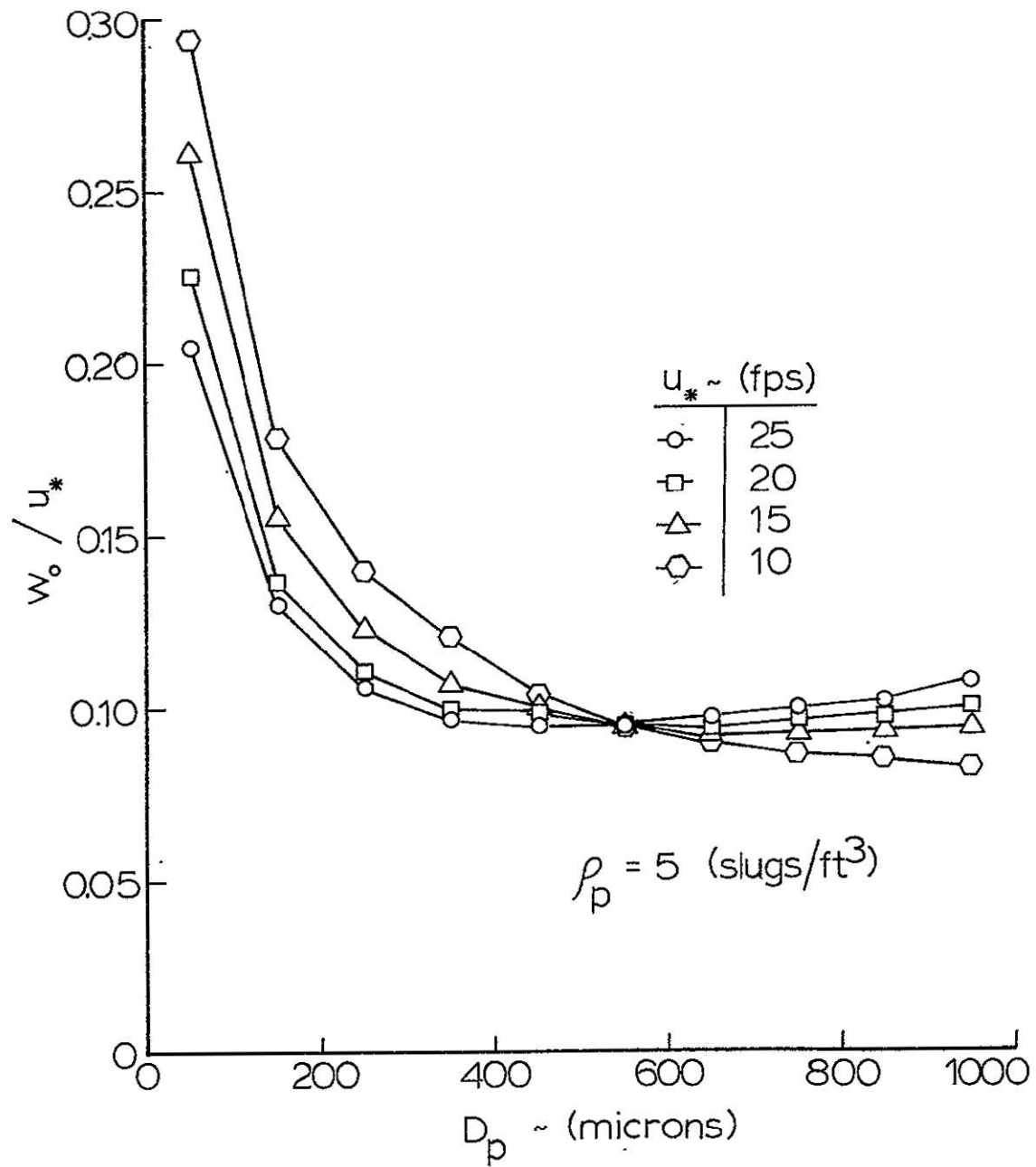
Figure 44. Maximum vertical velocity for Mars, effect of friction speed (laminar sublayer)

At smaller D_p (D_p < 350 microns) the ratio w_o/u_* increases rapidly as is the case of the fully turbulent boundary layer calculation for Earth. This exhibits the susceptibility of the smaller particles to movement by wind.

Figure 45 shows a plot of z_{max} versus u_* for four different particle diameters D_p = 250, 550, 750, and 1050 microns. An interesting point of this plot is that the variation of z_{max} for a constant u_* for a large range in D_p is relatively small and all seem to cross for a u_* range of 16-21 fps and reverse relative positions between the various particle diameters. The dashed lines connect the predicted threshold value (Iversen, 1975b) to curves of the numerical results.

Several additional mechanisms of lift function were also calculated. Of these, four cases were calculated in which the effect of the wall was increased from one particle diameter to 2, 3, 4, and 5 particle diameters. The resultant solution of the equations of motion shows very little increase in the z_{max} calculation. Both the Saffman lift and the modified Saffman lift (4π times the Saffman lift) were calculated with similar results.

One additional case calculated was that of the one earlier presented for Figure 41-45 with the exception that the lift function of 4π times Equation 6.6 was allowed to act for a distance of 10 particle diameters. This essentially curtailed the region of active lift force for smaller D_p
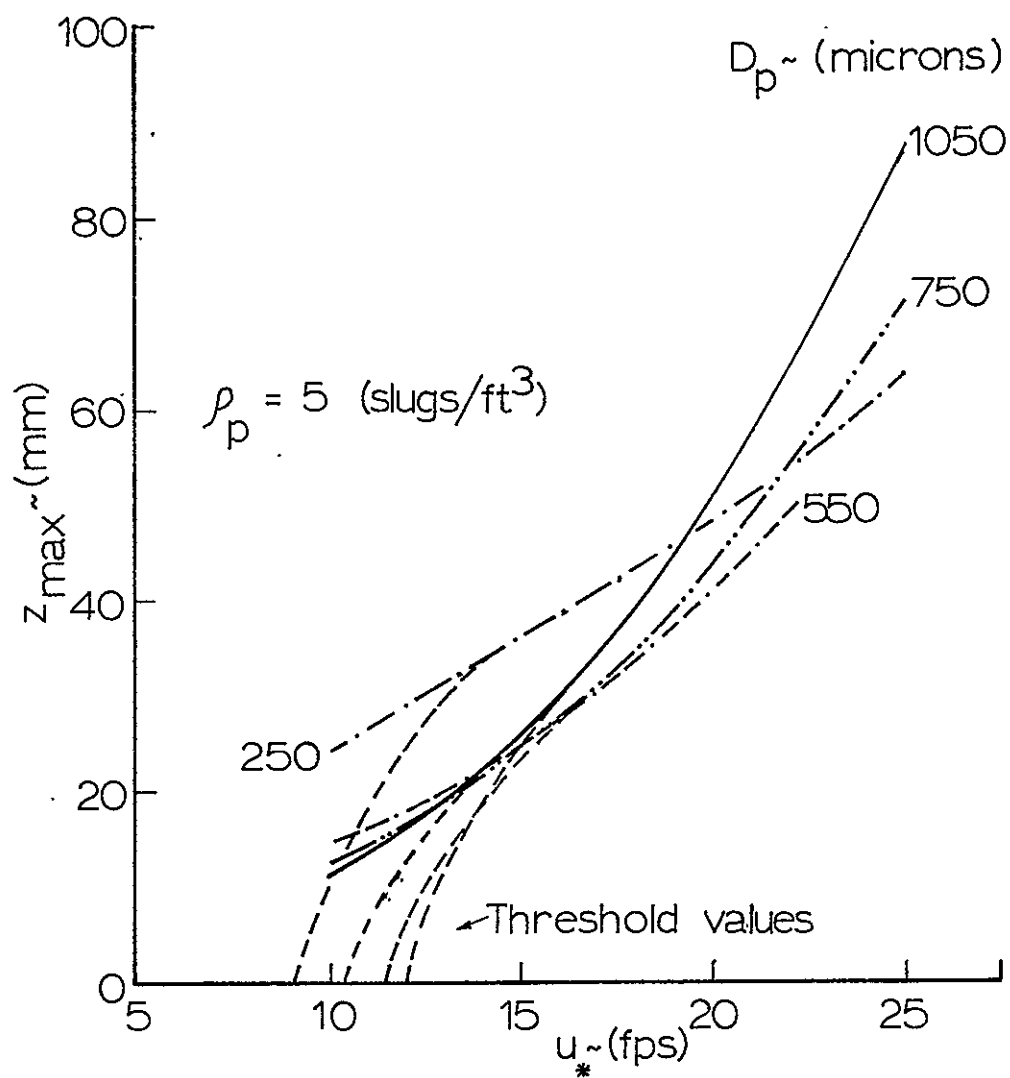
Figure 45. Maximum trajectory height for Mars, effect of particle size (laminar sublayer)

(D_p < 200 microns) and enhanced the net lift force of larger
D_p (D_p > 200 microns). This did not change the lift force
produced in the wall effect region but only altered the length
of the outer region where no wall effects were considered.
This type of calculation has the same type of validity as the
similar case presented for the Earth case (see the Earth case
of a laminar sublayer for a detailed discussion). Figure 46
displays a comparison of z_{max} versus D_p for $u_* = 20$, and 25
fps for the lift function where the outer lift region was
allowed to act to 10 particle diameters and to the sublayer
height for a constant $\rho_p = 7$ (slugs/ft^3). As can be observed
from the figure the effect of allowing lift to act to 10
particle diameters for the larger particles enhances the z_{max}
by a factor of 2 (D_p > 250) and suppresses the z_{max} for smaller
particle diameter (D_p < 150). The validity of the sublayer
calculation is believed by the author to be more accurate than
the comparative lift model of 10 particle diameters; however,
the true solution can only be guessed at this time. Figure 47
shows the corresponding curves of Figure 46 for w_o/u_* versus
D_p, and again similar trends to those of Figure 46 manifest
themselves.

3. Particle rebounding at Martian surface

An important process of particle saltation motion is the
bouncing interaction that occurs at the end of a particle
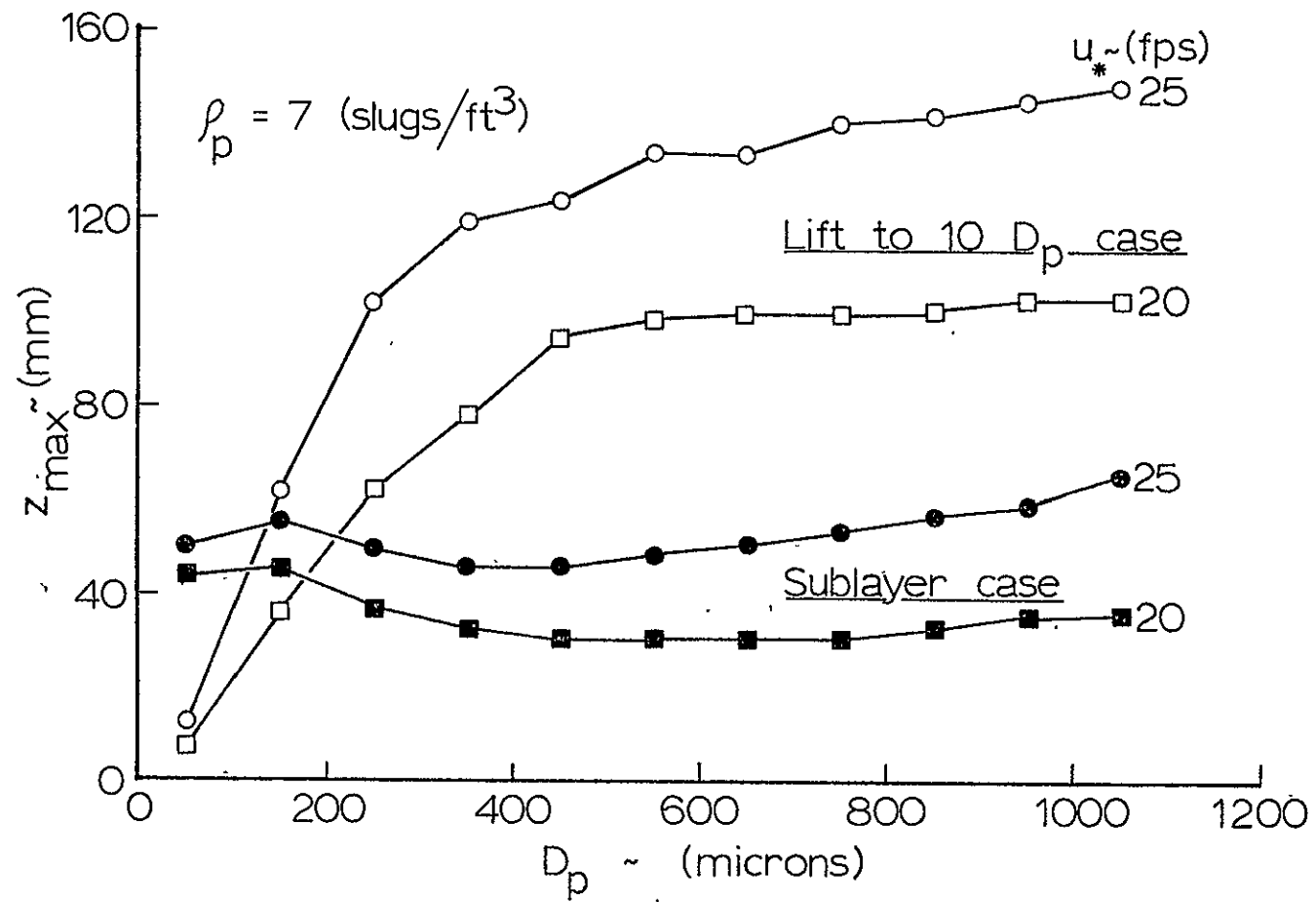trajectory. This process has long been observed and it is

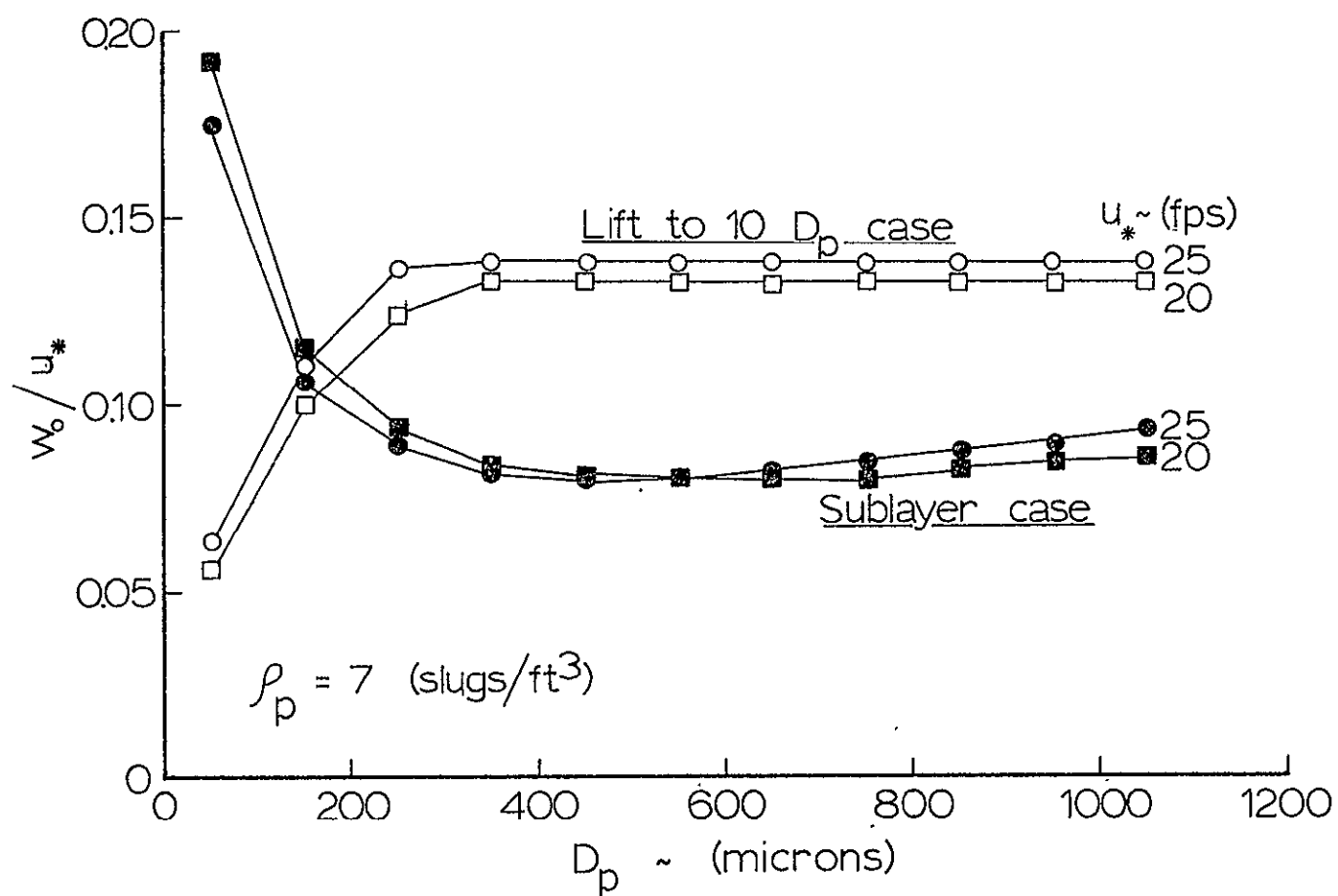Figure 46. Maximum trajectory height for Mars, comparison of lift model

Figure 47. Maximum vertical velocity for Mars, comparison of lift model

169

known that the collision of a single particle with a surface
of random composite of similar particles results in a highly
inelastic collision. Generally the single particle in motion
imparts the majority of its momentum to the surrounding
particles in contact with it at the surface which, according
to Allen (1968), initiates several other particles in motion.
The ensuing initial motion is nearly always vertical. These
particles then turn and travel in low trajectories at veloci-
ties nearly parallel to the surface at the end of the trajec-
tory. When particles strike the surface, a particle may either
rebound off the surface from a stationary particle or group of
particles, or impact into the surface of particles when several
other particles' motion may be initiated as discussed earlier.
In the case of the rebounding particle (or for that matter
particles initiated with a given percentage of the original
particle's momentum) the lifting process is a combination of
the initial upward component of vertical as well as the lift
force function.

Figure 48 is a plot of the normalized maximum height of
the trajectory and the final (or maximum) downstream distance,
z_{max}/D_p and Y_{max}/D_p respectively, versus the percentage of
momentum retained by the rebounding particle or which may be
considered as the percentage of momentum imparted to a similar
size particle upon collision. The lift function used in the
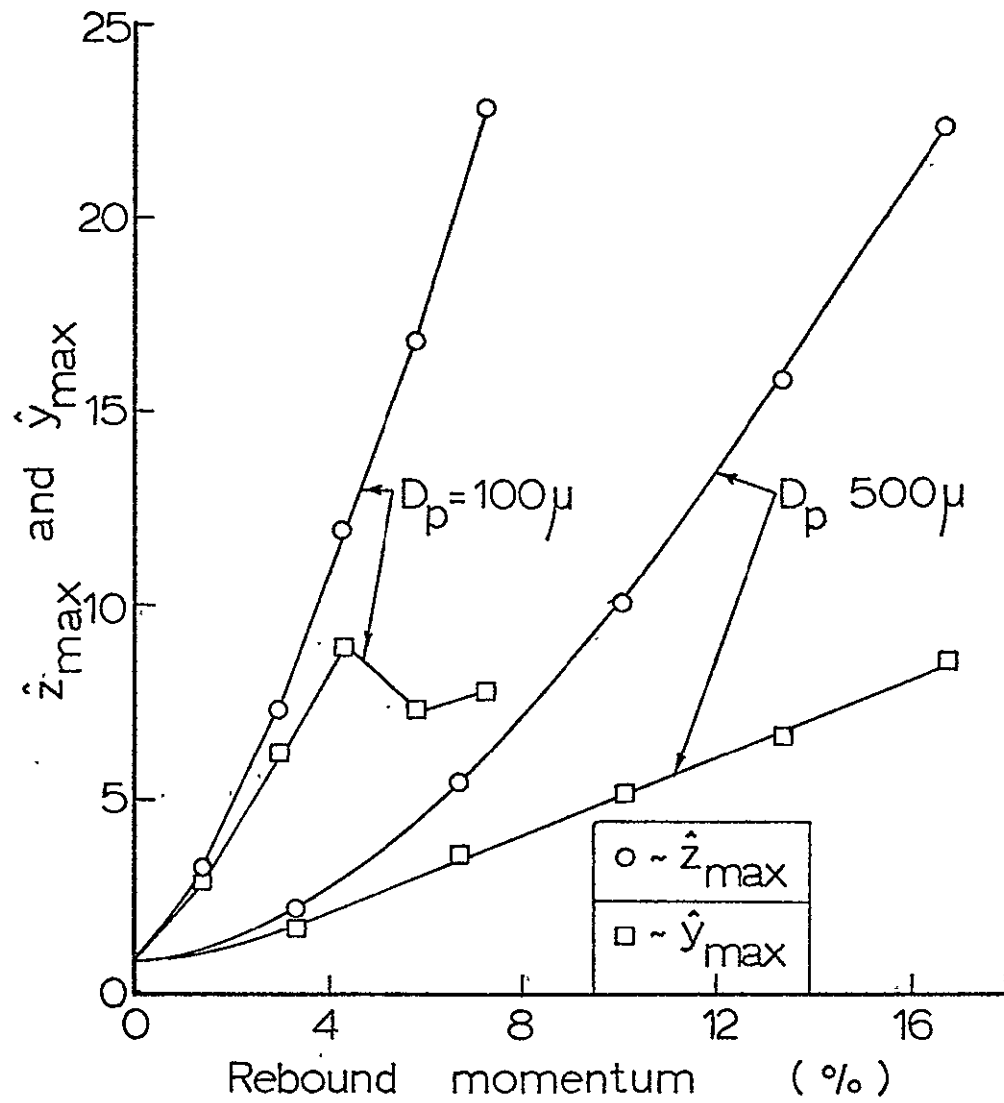calculations is that of 4π times Equations 6.2 and 6.4 for a

Figure 48. Effect of rebound momentum of trajectory height and length

100 and 500 microns particle diameter, however, for the case of the 100 microns particle the range of the lift function is the same as that of Equation 6.3. Nevertheless, the normalized quantities should be the same for similar type lifting functions as in the case here. As can be observed from these plots one sees that z_{max}/D_p increases much more rapidly than y_{max}/D_p for both the cases of 100 microns and 500 microns.

There is a rapid increase in z_{max}/D_p for small changes in the percentage of momentum. An unusual characteristic of the 100 microns y_{max}/D_p curve in the figure where a 4-5% momentum of original impact the y_{max}/D_p takes an unpredicted decrease in value. The value of curves is unity at zero momentum transfer and is an ordinary lift function calculation.

In connection with the rebounding particle it might be of interest to note that the particle returning to the surface seldom makes an angle with the surface of greater than 3 degrees and is often less than one degree. This value is unusually low but is characteristic of all Martian trajectory calculations. The typical collision for Earth conditions, as reported by Allen (1968), is in a range of 5 to 10 degrees which agrees with the Earth calculations. An important fact noted here then is that the Martian trajectories are much more parallel to the surface at collision than Earth trajectories. As a result the erosional effect may be greater on Mars than on Earth. The y_{max}/z_{max} ratio is much greater on Mars in

comparison to Earth calculations. In a paper by Andres (1969) the Mars particles trajectories were calculated and the surface interactions were taken into account. From Andres: "It was assumed that the incident particle upon impact with the surface loses the velocity component normal to the surface; that the particle rotation and remaining tangential velocity component adjust to the condition of rolling contact; and that the particle leaves the surface with these adjusted tangential and angular velocities in the direction given by the local surface slope." For the cases presented in Figure 48 this would infer that less than 1% of the impact momentum would be lost since the collision angle is very small. This assumption of Andres seems to be basically wrong and the actual situation appears to be a highly complicated interaction of several particles, none of which receive a large percentage of momentum.

Other numerical calculations of particle trajectories under Mars surface conditions were performed by Henry (1975) in which particle impact on wind sensors was investigated.

C. Simulated Flow Around a Crater

An interesting application of particulate flow is that of simulating particle motion in the downstream wake of crater flow. A detailed discussion of the characteristics of the flow field around a crater are given in Section V and pictorially displayed in Figure 3. The main aspect on the downstream wake flow of a crater is the existence of two counterrotating

vorticies formed from the horseshoe vortex which is wrapped around the front and sides of the outside crater rim. The direction of rotation of the two downstream vorticies is the same as the trailing vorticies created by a finite airfoil moving through a fluid.

A set of three-dimensional equations of motion were developed and programmed with capabilities of analytically input crossflow functions for the v and w components of velocity as well as the stream component u (recall the coordinate used here is the same as that of Figure 9). To numerically simulate the downstream flow of a crater with a vortex present the flow is assumed to be symmetric and stable around the crater. Thus it is only necessary to solve one-half the flow field (separated by the axial center $x = 0$).

A Rankine vortex is used in the numerical calculations to form the crossflow. From visual observation and studying the details of Tani's et al. (1962), Gregory and Walker's (1951), and Sedney's (1973) paper, the single vortex core is positioned at a height $z_0 = 2$ cm above the surface and a transverse distance of $x_0 = 6$ in. (≈ 15 cm) off of the axial centerline. The crossflow component of velocity V_θ is then expressed as

$$V_\theta = \frac{\Gamma r}{2\pi r_1^2} \qquad \text{for} \quad r \leq r_1 \qquad (6.16a)$$

and

$$V_\theta = \Gamma/2\pi r \qquad \text{for} \qquad r > r_1 \qquad (6.16b)$$

where Γ is the strength of the circulation, r_1 is the radius of the vortex core, and r is the distance of the particle from the center of the vortex core, i.e.,

$$r = \sqrt{(z-z_o)^2 + (x-x_o)^2} \qquad (6.17)$$

The value of the strength of the vortex Γ was selected from the experimental results of Section V, and given a value that corresponds to a maximum crossflow speed (at $r = r_1$) of 10% of freestream value, i.e.,

$$V_\theta = 0.1\, u_\infty \qquad (\text{at } r = r_1) \qquad (6.18)$$

And from experimental results it is found that

$$u_\infty = 23\, u_* \qquad (6.19)$$

and thus substituting this into the above equation yields

$$V_\theta = 2.3\, u_* \qquad (\text{at } r = r_1) \qquad (6.20)$$

or

$$\Gamma = 14.45\, u_*\, r_1 \qquad (6.21)$$

and for $r_1 = 1$ cm this is

$$\Gamma = 0.47396\, u_*\, [\text{ft}^2/\text{sec}] \qquad (6.22)$$

This expression predicts a velocity flow through the surface which physically can not exist and therefore was corrected to account for this wall effect. The empirically approximated wall effect is assumed to have the same fundamental properties as the function of axial velocity. This states that the wall effect of the vortex motion tends to curtail the flow in much a similar matter as the axial velocity profile, i.e.

$$V_{\theta_{eff}} = f_1(u_*, r_1) f_2(u/u_o) \tag{6.23}$$

where $V_{\theta_{eff}}$ is the effective crossflow velocity, f_1 is the unbound vortex motion function, and f_2 is the empirical function of wall effect. A suitable f_2 was selected as

$$f_2 = (u/u_o)^{0.15} \tag{6.24}$$

where u_o is a reference velocity calculated at the height of the center of the vortex core (2 cm). Thus, at a height of the vortex core the motion of the vortex is unaffected by the wall.

The components of crossflow v and w then are expressed as

$$v = V_{\theta_{eff}} (z_o - z)/r \tag{6.25}$$

$$w = V_{\theta_{eff}} (x - x_o)/r \tag{6.26}$$

for the selected direction of the vortex.

The equations of motion including the crossflow given above were solved for the Martian surface condition of $\rho_p = 5$ (slugs/ft^3) and a friction velocity of $u_* = 20$ fps with a lifting function of Equations 6.2 and 6.3 for both a 100 and 500 micron particle diameter. Generally speaking the motion of saltating particles is severely inhibited on the downwind side of the vortex motion and greatly enhanced on the upwind side. This causes increases in the final velocity of the particle's trajectories, u_F, and also in y_{max}, z_{max}, and the maximum upward component of vertical velocity, w_o.

Figures 49 and 50 show plots of the above quantities (normalized by the vortex-free solution) versus the transverse distance x away from the axial centerline for both a 100 and 500 micron particle diameter case, respectively. The location of the vortex position is denoted by a single vertical dashed line.

Figure 49 has two different vertical scales, the left one for w_{max} and V_F and the right one for the x_{max} and y_{max}. The plot displays the enormous effect the vortex crossflow has on the particle's trajectories. For transverse length less than 5 inches the vortex's vertical component velocity is downward and inhibits the particle motion in all four variables displayed, but for larger values of x ($x \geq 5$) the motion is tremendously increased in all variables. Both x_{max} and z_{max} obtain values nearly 50 times their normal value at the vortex
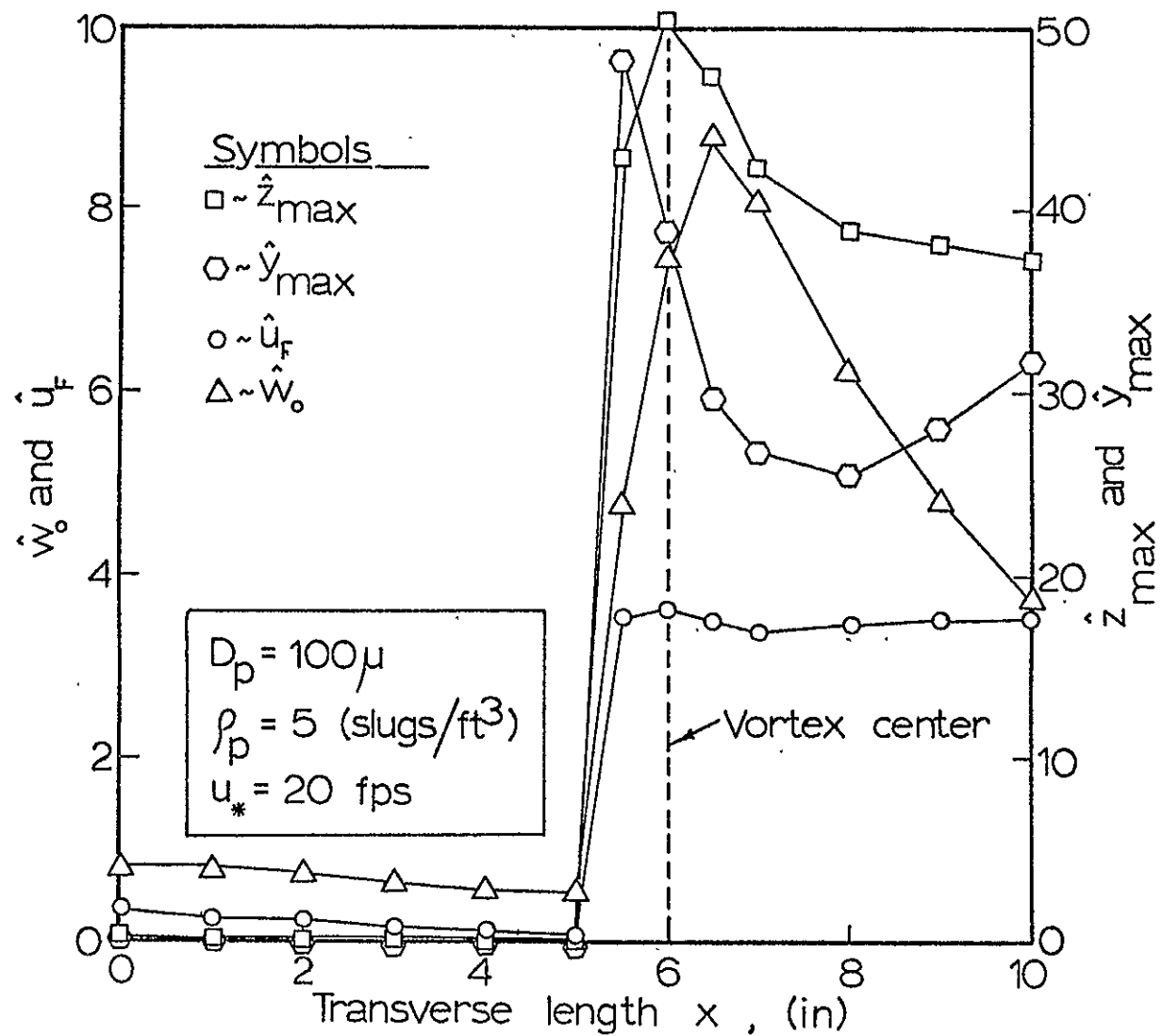
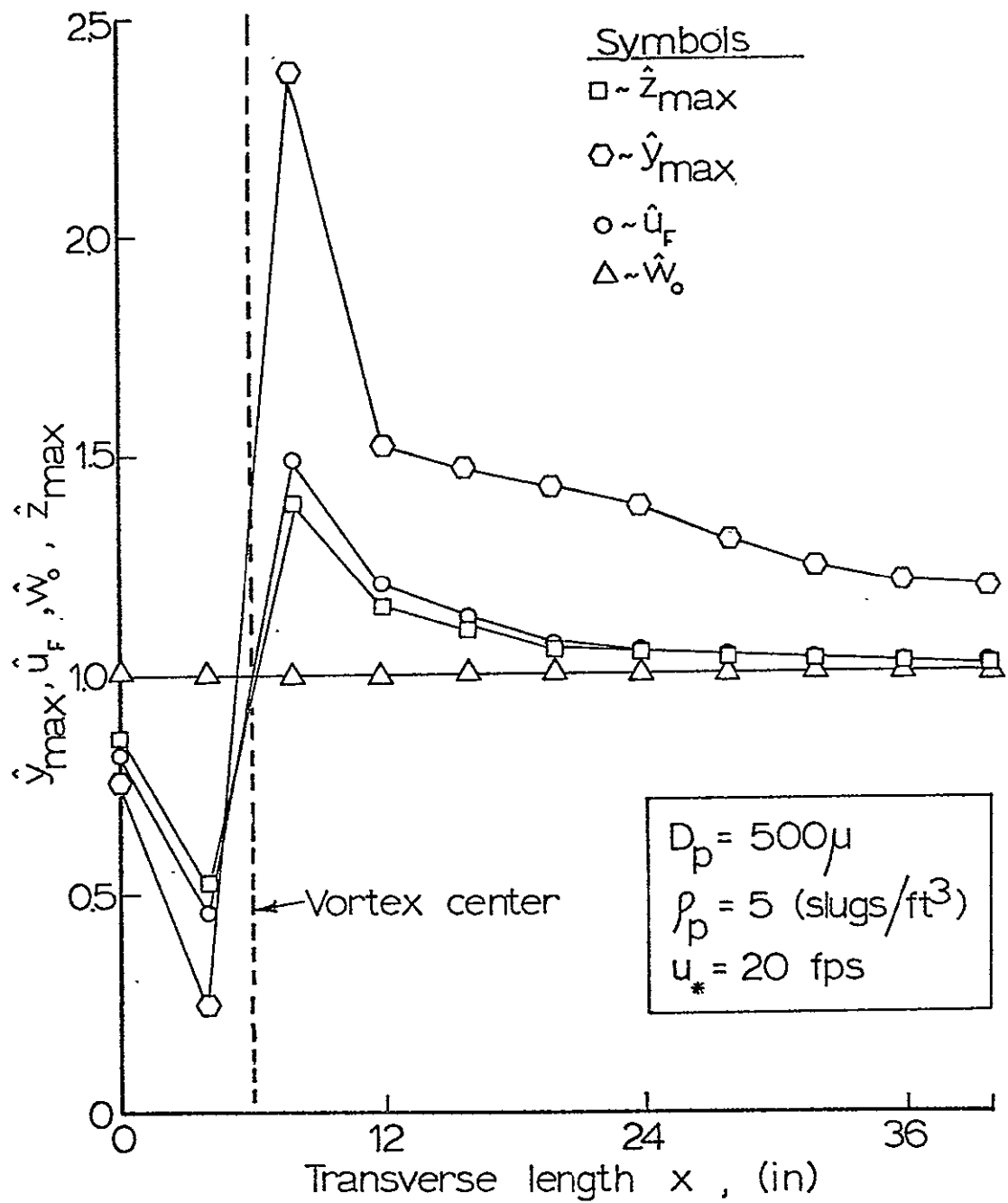Figure 49. Effect of initial particle location with respect to vortex on trajectory characteristics ($D_p = 100\mu$)

Figure 50. Effect of initial particle location with respect to vortex on trajectory characteristics (D_p = 500μ)

location and then gradually return to unity with increasing distance. The normalized final velocity u_F and normalized maximum vertical velocity w_0 obtain values of 3.63 and 8.8, respectively. An interesting point is that the u_F does not immediately return to unity but retains a value nearly constant of 3.5. This would decrease the collision angle of the surface compared to normal trajectories without vortex presence. Also as the transverse length is increased ($x \geq 5$ inches) the z_{max} decreases but the u_F stays the same. This would also decrease the collision angle further with increase in transverse length. The net effect of this would be to increase the erosion on the outward side of the vortex transverse location. These numerical results seem to support the theories of a similar nature expressed by and the experimental results of Greeley et al. (1974) and Iversen et al. (1975a). This is a remarkable result which also supports imagery received from Mariner 9 (see Figures 1 and 2).

Figure 50 shows the similar case for a 500 micron particle diameter but the effects of the vortex motion are considerably less.

Figure 51 displays the lateral motion (or spiral) of a single particle initially started at several various transverse positions. All of the trajectories show a motion of the particle that generally follows the direction of the vortex velocity. These trajectories are for the corresponding
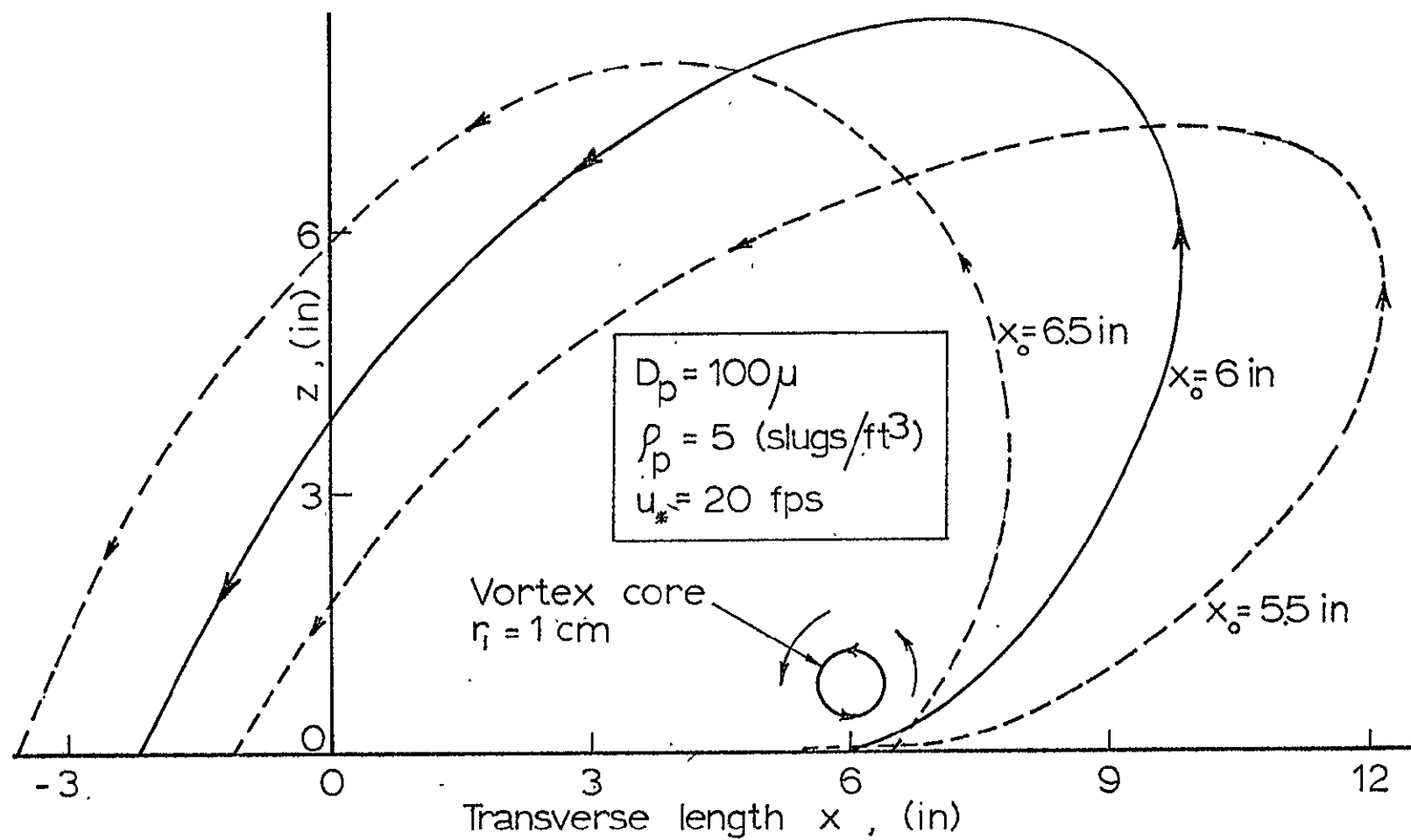
Figure 51. Lateral and vertical particle position with respect to the vortex.

calculations of Figure 49. These curves show that the smaller particles are greatly affected by the vortex motion and obtain heights of two orders of magnitude higher than normal. It also infers from the curvature of the particle trajectories that there would be considerably more particle interaction (collisions) in the vicinity of the vortex cores.

The net conclusion of these vortex calculations is that the final velocity of the particle u_F is increased on the outer edge of the vortex core thus causing a greater increase in surface erosion rate. Also trajectory calculations show a curvature of the particle motion that follows the vortex motion which affects smaller particles much more than larger particles.

C. 3

VII. CONCLUDING REMARKS

The experimental pitot tube study of the three-dimensional wake flow field around the model crater performed in an environmental wind tunnel proved to be very important. A qualitative description of the surface shear stress was obtained which exhibits large shear stresses immediately downstream of the crater centerline. The data also displayed trends that occurred in the dimensionless velocity profile with different locations in the flow field downstream of the crater including velocity defects possibly resulting from the horseshoe vortex system. In addition to the pitot probe, a three-dimensional hot-film sensor was used to measure magnitudes of crossflow. These were used later in three-dimensional numerical crater simulation flow.

For the two-dimensional numerical study of particle flow the importance of the lift force in the equation of motion was demonstrated. Empirical lift functions were developed for both laminar sublayer and fully turbulent flow for Earth (that approximates the limited experimental data) and was used to approximate transition flow. The effect of an idealized cyclic numerical turbulence model showed turbulence to be a minor factor in the determination of particle trajectories ($D_p > 100$ microns).

The empirical lift functions were used to calculate particle trajectories for the Mars surface conditions and should be as accurate as for Earth. The effect of slip flow was shown to be an important factor in small diameter particle trajectories (D_p < 250 microns) and therefore was included in all Mars calculations. In comparison to Earth trajectories for the same friction velocity ratio, u_*/u_{*t}, the Mars trajectories exhibit higher z_{max}'s (up to approximately 40%) and longer y_{max}'s than that of Earth. The ratio y_{max}/z_{max} was considerably larger on Mars and exhibited a much lower surface collision angle (generally less than 3°) than Earth's (usually from 5° to 10°). Some other significant results are that the maximum upward velocity ratio w_o/u_* is approximately one-tenth of that of Earth's, and the final velocity u_F is much higher on Mars thus causing a high erosional effect.

The effect of momentum exchange of inelastic collisions of particles at the surface for Mars was investigated and it is found that smaller particles rebounded several times higher than normally would be predicted, while retaining after collision only a small percentage of its total momentum. This effect decreased with increasing particle size.

Finally, a combination of the experimental data and two-dimensional particle calculation was used in the three-dimensional particle flow in the wake of a crater. The significant results of this combination of a turbulent layer

and a vortex flow include curtailment of particle motion on the side of the vortex closest to the wake centerline and an enhancement of the trajectories on the outer side of the vortex. An increased value of u_F and a decreased value of the collision angle compared to vortex free motion result both of which add to the erosional effect. Also the small particle ($D_p < 200$ microns) trajectories were highly affected by the vortex motion.

However, the results of this study are by no means conclusive and would indicate the need for future work. Of the future work an interesting research area would be the experimental investigation of the actual lift force exerted on small particles and also of interest would be an experimental investigation of the average paths of particle motion under various wind tunnel conditions. This could possibly be accomplished by the use of high speed movies.

Numerically, the ultimate goal of this study would be to combine a three-dimensional flow field with the particle equations of motion to study the motion of a particle in flow around a crater. Several particles could simultaneously be followed through the flow field. The specific application of this process to Martian conditions could possibly match the imagery (received from Mariner 9) of what is believed to be caused by flow over Martian craters provided the movement of many particles is allowed to occur. The resultant type of

program could also be used to test newly designed structures
that might be subject to snow, dust and sand storms. This
ultimate goal is quite complex and would involve a large amount
of computer storage and computer time to solve for the
trajectories of hundreds and even thousands of particles in
simultaneous motion. Eventually, perhaps a dual process could
be involved where the particle equations of motion are solved
numerically and then the partial differential equations of
motion could be solved thus yielding a new flow field. This
process could be repeated until the problem is solved. Cur-
rently, most such solutions are beyond the storage capacity of
present day computers.

VIII. LITERATURE CITED

Adlon, G. L., R. K. Weinberger, and D. R. McClure. 1969. "Sand and Dust Storm Simulation and Evaluation." National Aeronautics and Space Administration, NASA CR-66882.

Allen, J. R. L. 1968. Physical Process of Sedimentation an Introduction. London: George. Allen and Unwin LTD.

Andres, R. M. 1970. "The Mechanics of Dust Lifting with Particular Emphasis on the Planet Mars." Ph.D. dissertation, Library, St. Louis University, St. Louis, Missouri.

Arvidson, R. E. 1974. "Wind-blown streaks, splotches, and associated craters on Mars: Statistical analysis of Mariner 9 photographs." Icarus 21: 12-27.

Arya, S. P. S. and E. J. Plate. 1969. Modeling of the Stably Stratified Atmospheric Boundary Layer." Journal of Atmospheric Sciences 26, No. 4: 656-665.

Bagnold, R. A. 1941. The Physics of Blown Sand and Desert Dunes. London: Methuen and Co., Ltd.

Bagnold, R. A. 1973. "The Nature of Saltation and of 'Bedload' Transport in Water." Proceedings of the Royal Society, London, Series A, 332: 473-504.

Bailey, A. B. 1974. "Sphere Drag Coefficient for Subsonic Speeds in Continuum and Free-Molecule Flow." Journal of Fluid Mechanics, 65, No. 2: 401-410.

Basset, A. B. 1961. Hydrodynamics. New York: Dover.

Benson, B. W. 1966. "Cavitation Inception on Three-Dimensional Roughness Elements." David Taylor Model Basin, Washington, D.C., Report 2104.

Bidwell, J. M. 1965. "Notes on Martian Sandstorms." Martin Marietta Corporation Report 1610-68-34.

Bradshaw, P. 1967. "'Inactive' Motion and Pressure Fluctuations in Turbulent Boundary Layers." Journal of Fluid Mechanics 30: 241-258.

Brown, R. L. 1961. Flow Properties in 'Powders in Industry.' New York: Gordon and Breach.

Bull, M. K.   1967.   "Wall Pressure Fluctuations Associated
    with Subsonic Turbulent Boundary Layer Flow." Journal
    of Fluid Mechanics 28:   719-754.

Calder, K. L.   1966.   "Concerning the Similarity Theory of
    A. S. Monin and A. M. Obukhov for the Turbulent Structure
    of Thermally Stratified Surface Layer of the Atmosphere."
    Quarterly Journal of the Royal Meteorological Society 92,
    No. 301:   141-146.

Cermak, J. E.   1963.   "Lagrangian Similarity Hypothesis
    Applied to Diffusion in Turbulent Shear Flows." Journal
    of Fluid Mechanics 15, No. 1:   49-64.

Cermak, J. E.   1971.   "Laboratory Simulation of the Atmospheric
    Boundary Layer." AIAA Journal 9, No. 9:   1746-1754.

Cermak, J. E. et al.   1966.   "Simulation of Atmospheric Motion
    by Wind Tunnel Flows." Fluid Dynamics and Diffusion Lab,
    Colorado State University, Technical Report CER66JEC-VAS-
    EJP-GJB-HC-RNM-SI17.

Chang, T. S., W. C. Lucau, and W. W. Youngblood.   1968.
    "Laboratory Simulation of the Mars Atmosphere, A
    Feasibility Study." National Aeronautics and Space
    Administration, NASA CR-61168.

Chepil, W. S.   1945.   "Dynamics of Wind Erosion, II.
    Initiation of Soil Movement." Soil Science 60:   397-411.

Chepil, W. S.   1958.   "The Use of Evenly Spaced Hemispheres to
    Evaluate Aerodynamic Forces on a Soil Surface."
    Transactions, American Geophysical Union 39, No. 3:   397-
    403.

Chepil, W. S.   1959.   "Equilibrium of Soil Grains at the
    Threshold of Movement by Wind." Soil Science Society
    Proceddings 1959:   422-428.

Chepil, W. S. and N. P. Woodruff.   1963.   "The Physics of Wind
    Erosion and its Control." Advances in Agronomy 15:   211-
    302.

Clark, J. A.   1968.   "A Study of Incompressible Turbulent
    Boundary Layers in Channel Flow." American Society of
    Mechanical Engineers Transactions, Series D: Journal of
    Basic Engineering 90:   455-468.

Clauser, F. H. 1956. "The Turbulent Boundary Layer." Advances in Applied Mechanics 4: 1-51.

Counihan, C. 1969. "An Improved Method of Simulating an Atmospheric Boundary Layer in a Wind Tunnel." Atmospheric Environment 3: 197-214.

Crane, R. L. 1962. "Stability and local accuracy of numerical methods for ordinary differential equations." Library, Iowa State University, Ames, Iowa.

Cunningham, E. 1910. "On the Velocity of Steady Fall of Spherical Particles Through Fluid Medium." Proceedings of the Royal Society, London, Series A, 83: 357-365.

Davies, C. N. 1945. "Definitive Equations for the Fluid Resistance of Spheres." The Proceedings of the Physical Society 57, part 4, No. 322: 259-270.

deVaucoulers, G. 1954. Physics of the Planet Mars. London: Faber and Faber Ltd.

Einstein, H. A. and E. El-Samni. 1949. "Hydrodynamic Forces on a Rough Wall." Reviews of Modern Physics 21, No. 3: 520-524.

Ekman, V. W. 1905. "On the Influence of the Earth's Rotation on Ocean-Currents." Arkiv För Matematik, Astronomi Och Fysik 2, No. 11: 1-52.

Epstein, P. S. 1924. "On the Resistance Experienced by Sphere in Their Motion Through Gases." Physical Review 23: 710-733.

Ford, E. F. 1957. "The Transport of Sand by Wind." Transactions of the American Geophysical Union 38: 171-174.

Francis, J. R. D. 1973. "Experiments on the Motion of Solitary Grains Along the Bed of a Water-Stream." Proceedings of the Royal Society, London, Series A, 332: 443-471.

Fuchs, N. A. 1964. Mechanics of Aerosols. New York: Pergamon Press.

Gerdel, R. W. and G. H. Strom. 1961. "Scale Model Simulation of a Blowing Snow Environment, Proceedings." Institute of Environmental Science 53: 53-63.

Giedt, W. H. 1951. "Effect of Turbulence Level of Incident Air Stream on Local Heat Transfer and Skin Friction on a Cylinder." Journal of Aerospace Science 18: 725-732.

Goldman, A. J., R. G. Cox, and H. Brenner. 1967. "Slow Viscous Motion of a Sphere Parallel to a Plane Wall-II." Chemical Engineering Science 22: 653-660.

Goldstein, S. 1938. Modern Developments in Fluid Dynamics. London: Oxford University Press.

Greeley, R., J. D. Iversen, J. B. Pollack, N. Udovich, and B. R. White. 1973. "Wind Tunnel Studies of Martian Eolian Processes." National Aeronautical and Space Administration, NASA TM X-62,297. (To be published by Proceedings of the Royal Academy of Science London).

Greeley, R., J. D. Iversen, J. B. Pollack, N. Udovich, and B. R. White. 1974. "Wind Tunnel Simulation of Light and Dark Streaks on Mars." American Association for the Advancement of Science 132: 847-849.

Gregg, S. J. 1961. The Surface Chemistry of Solids. New York: Reinhold.

Gregory, N. and W. Walker. 1951. "The Effect of Transition of Isolated Surface Excrescences in the Boundary Layer," Great Britain, Aeronautical Research Council, Reports and Memoranda No. 2779.

Gugan, K., J. Lawton, and F. J. Weinberg. Proceedings of the 10th Symposium (International) on Combustion, 709.

Halitsky, J. 1969. "Validation of Scaling Procedures for Wind Tunnel Model Testing Diffusion Near Buildings." Geophysical Sciences Laboratory, New York University, Technical Report 69-8.

Harper, E. Y. and I. D. Chang. 1968. "Maximum Dissipation Resulting from Lift in a Slow Viscous Shear Flow." Journal of Fluid Mechanics 33, No. 2: 209-225.

Henry, R. M. 1975. "Saltation on Mars and the Expected Lifetime of Viking 75 Wind Sensors." National Aeronautics and Space Administration, NASA Prospective Technical Note.

Hertzler, R. G. 1966a. "Behavior and Characteristics of Simulated Martian Sand and Dust Storms." McDonnell Aircraft Corporation Report E720.

Hertzler, R. G. 1966b. "Particle Behavior in a Simulated Martian Environment." McDonnell Aircraft Corporation Report E418.

Hidy, G. M. 1966. "On Atmospheric Simulation: A Colloquium." National Center for Atmospheric Research, Boulder, Colo., NCAR-TN-22.

Hoglund, R. F. 1962. "Recent Advances in Gas-Particle Nozzle Flows." Aeronautical Royal Society Journal 32: 662.

Hunt, J. C. R. 1971. "The Effect of Single Buildings and Structures." Philosophical Transactions of the Royal Society of London, Series A, 269: 457-468.

Iversen, J. D., R. Greeley, J. B. Pollack, and B. R. White. 1973. "Simulation of Martian Eolian Phenomena in the Atmospheric Wind Tunnel." 7th Conference on Space Simulation, NASA SP-336: 191-213.

Iversen, J. D., R. Greeley, B. R. White, and J. B. Pollack. 1975a. "Saltation Threshold on Mars; the Effect of Interparticle Force, Surface Roughness, and Low Atmospheric Density." Submitted by Icarus.

Iversen, J. D., R. Greeley, B. R. White, and J. B. Pollack. 1975b. "Eolian Erosion on the Martian Surface; Part 1: Erosion Rate Similitude." Submitted to Icarus.

Jeffreys, H. 1929. "On the Transport of Sediments by Streams." Cambridge Philosophical Society Proceedings 25: 272-276.

Jensen, J. 1958. "The Model-Law for Phenomena in Natural Wind." Ingeniøren 2: 121-128.

Kitchener, J. A. 1961. Powders in Industry. New York: Gordon and Breach.

Kline, S. J. 1966. "Some Remarks on Turbulent Shear Flows." Proceedings of the Institution of Mechanical Engineers 180: 222-244.

Kline, S. J., W. C. Reynolds, F. A. Schraub, and P. W. Runstadler. 1967. "The Structure of Turbulent Boundary Layers." Journal of Fluid Mechanics 30: 741-773.

Knudsen, M. and S. Weber. 1911. "Luftwiderstand gegen die langsame Beweguny Kleiner Kugeln." Ann. der Physik, 36: 981-994.

Kuhn, W. E. 1961. Ultrafine Particles. New York: Wiley.

Kuiper, G. P. 1957. "Visual Observations of Mars, 1956."
    Astrophysics Journal 125: 307-317.

Lamb, H. 1932. Hydrodynamics. New York: Dover.

Lumley, J. L. and H. A. Panofsky. 1964. The Structure of
    Atmospheric Turbulence. New York: Wiley.

Malina, F. J. 1941. "Recent Developments in the Dynamics of
    Wind-Erosion." Transactions of the American Geophysical
    Union, Part II, 262.

Marble, F. E. 1962. "Dynamics of a Gas Containing Small
    Solid Particles." Combustion and Propulsion, Fifth AGARD
    Colloqium, Braunschweig, April 9-13. High-Temperature
    Phenomena. New York: Pergamon Press.

Masursky, H. 1973. "An Overview of Geological Results from
    Mariner 9." Journal of Geophysical Research 78: 4009-
    4030.

Mattauch, J. 1925. "Eine Experimentelle Ermittlung des
    Widerstandsgesetzes Kleiner Kugeln in Gasen." Zeitschrift
    Physik 32: 439-472.

McVehil, G. E., G. R. Ludwig, and T. R. Sundaram. 1967.
    "On the Feasibility of Modeling Small Scale Atmospheric
    Motion." Cornell Aeronautical Laboratory, Buffalo,
    New York, CAL Report ZB-2328-P-1.

Millikan, R. A. 1923a. "The General Law of Fall of a Small
    Spherical Body Through a Gas, and its Bearing Upon the
    Nature of Molecular Reflection From Surfaces." The
    Physical Review 22, No. 1: 1-23.

Millikan, R. A. 1923b. "Coefficients of Slip in Gases and the
    Law of Reflection of Molecules From Surfaces of Solid and
    Liquids." The Physical Review 21, No. 3: 217-239.

Monin, A. S. 1970. "The Atmospheric Boundary Layer."
    Annual Reviews of Fluid Mechanics 1970: 225-250.

Monin, A. S. and A. M. Obukhov. 1954. "Basic Regularity in
    Turbulent Mixing in the Surface Layer of the Atmosphere."
    Izv. Akad. Nauk. SSSR, Ser. Geotiz, No. 24.

Monin, A. S. and A. M. Yaglom. 1965. Statistical Hydro-mechanics, Part I: The Mechanics of Turbulence. Moscow: Nauka Press, English translation by Joint Publications Research Service, U.S. Department of Commerce.

Morsi, S. A. and A. J. Alexander. 1972. "An Investigation of Particle Trajectories in Two-Phase Flow Systems." Journal of Fluid Mechanics 55, No. 2: 193-208.

Nikuradse, J. 1932. "Gesetzmä igkeit der Turbulenten Strömung in Glatten Rohren." Forsch. Arb. Ing.-Wes., No. 356.

Nikuradse, J. 1933. "Strömungsgesetze in Rauhen Rohren." Forsch. Arb. Ing.-Wes., No. 361.

O'Neill, M. E. 1968. "A Sphere in Contact with a Plane Wall in a Slow Linear Shear Flow." Chemical Engineering Science 23: 1293-1298.

Owen, P. R. 1964. "Saltation of Uniform Grains in Air." Journal of Fluid Mechanics 20: 225-242.

Panofsky, H. A. and R. A. McCormick. 1960. "The spectrum of vertical velocity near the surface." Quarterly Journal of the Royal Meteorological Society 86: 495-503.

Plate, E. J. and J. E. Cermak. 1963. "Micro-Meteorological Wind Tunnel Facility." Fluid Dynamics and Diffusion Laboratory, Colorado State University, Report CER63EJP-JEC9.

Plate, E. J. and A. A. Ouraishi. 1965. "Modeling Velocity Distributions Inside and Above Tall Crops." Journal of Applied Meteorology 4, No. 3: 400-408.

Pollack, J. B., R. Greeley, J. D. Iversen, and R. Haberle. 1974. "Estimates of the Minimum Wind Needed to Raise Dust on Mars." Presented to American Astronomical Society, Div. Planetary Sciences, 5th Annual Meeting.

Prandtl, L. 1952. Essentials of Fluid Dynamics. New York: Hafner Publishing Co.

Proundman, I. and J. R. A. Pearson. 1957. "Expansions at Small Reynolds Numbers for the Flow Past a Sphere and a Circular Cylinder." Journal of Fluid Mechanics 2: 237-262.

Rainbolt, M. T. 1968. "A Study of the Wake Downstream of Single Three-Dimensional Roughness Elements." Unpublished M.S. Thesis, Library, Washington State University, Pullman, Washington.

Raudkivi, A. J. 1967. Loose Boundary Hydraulics. Oxford: Pergamon Press.

Rea, D. G. 1964. "The Darkening Wave of Mars." Nature 201: 1014-1015.

Roberson, J. A. and C. K. Chen. 1970. "Flow in Conduits with Low Roughness Concentration." Journal of the Hydraulics Division, ASCE 96, No. HY4: 941-957.

Roberts, L. 1966. The Fluid Dynamics of Space Flight, II. New York: Gordon and Breach.

Robinow, S. and J. Keller. 1961. "The Transverse Force on a Spinning Moving in a Viscous Fluid." Journal of Fluid Mechanics 11: 447-459.

Rubey, W. W. 1938. "The Force Required to Move Particles On a Stream Bed." U.S. Geological Survey Paper 189E.

Ryan, J. A. 1964. "Notes on the Martian Yellow Clouds." Journal Geophysical Research 69: 3759-3770.

Saffman, P. G. 1965. "The Lift on a Small Sphere in a Slow Shear Flow." Journal of Fluid Mechanics 22: 385-400; Corrigendum. 1968. Journal of Fluid Mechanics 31: 624.

Sagan, C. and J. B. Pollack. 1969. "Windblown Dust on Mars." Nature 223: 791-794.

Sagan, C., J. Veverka, P. Fox, R. Dubisch, J. Lederberg, E. Levinthal, L. Quam, R. Tucker, J. B. Pollack, and B. A. Smith. 1972. "Variable Features on Mars: Preliminary Mariner 9 Television Results." Icarus 17: 346-372.

Sagan, C., J. Veverka, P. Fox, R. Dubisch, R. French, P. Gierasch, L. Quam, J. Lederberg, R. Leventhal, R. Tucker, B. Eross, and J. B. Pollack. 1973. "Variable Features on Mars II: Mariner 9 Global Results." Journal of Geophysical Research 78: 4163-4196.

Schlichting, H. 1968. Boundary Layer Theory. New York: McGraw-Hill.

Sedney, R. 1973. "A Survey of the Effects of Small Protuberances on Boundary-Layer Flow." AIAA Journal 11: 782-792.

Snyder, W. 1972. "Similarity Criteria for the Application of Fluid Models to the Study of Air Pollution Meteorology." Boundary Layer Meteorology 3: 113-134.

Soo, S. L. 1967. Fluid Dynamics, of Multiphase Systems. Waltham, Massachusetts: Blaisdell Publishing Co.

Soo, S. L. and C. L. Tien. 1960. "Effect of the Wall on Two-Phase Turbulent Motion." Journal of Applied Mechanics Transactions, ASME 27: 5-14.

Stokes, G. G. 1891. Mathematical and Physical Papers 3: 55.

Strom, G. H., G. R. Kelly, E. L. Keitz, and R. F. Weiss. 1962. "Scale Model Studies on Snow Drifting." R. R. 73, U.S. Army Snow Ice and Permafrost Research Establishment, Corps of Engineers, Department of Army Task, 8X99-27-001-03.

Sundaram, T. R., G. R. Ludwig, and G. T. Skinner. 1972. "Modeling of the Turbulence Structure of the Atmospheric Surface Layer." AIAA Journal 10, No. 6: 743-750.

Sutton, O. G. 1953. Micrometeorology. New York: McGraw-Hill.

Sydney, R. 1972. "The Effects of Steady, Three-Dimensional Perturbations in Boundary Layers." AIAA 5th Fluid and Plasma Dynamics Conference, Paper No. 72-713, New York, N.Y.

Tani, I. 1968. "Computation of Turbulent Boundary Layers." AFOSR-IFP-Stanford Conference 1: 483.

Tani, I., H. Komoda, Y. Komatsu, and M. Iuchi. 1962. "Boundary-Layer Transition by Isolated Roughness." Aeronautical Research Institute, University of Tokyo, Report No. 375, 28, No. 7: 129-142.

Teilman, H. W., K. P. Fewell, and H. L. Wood. 1971. "An Evaluation of the Three-Dimensional Split-Film Anemometer for Measurements of Atmospheric Turbulence." Dept. of Engineering Science and Mechanics, Virginia Polytechnic Institute and State University, Blacksburg, Virginia.

Thermo-Systems Incorporated. 1970. "Operating and Service Manual for Model 1080 and Model 1080D Total Vector Anemometer." St. Paul, Minnesota: Thermo-Systems Incorporated.

Torobin, L. G. and W. H. Ganvin. 1959. "Fundamental Aspects of Solid-Gas Flow." Canadian Journal of Chemical Engineering 37: 129-141, 167-176, 224-276; 38 (1960): 142-153, 189-200.

Tritton, D. J. 1967. "Some New Correlation Measurements in a Turbulent Boundary Layer." Journal of Fluid Mechanics 28: 439-462.

Truckenbrodt, E. 1955. "A Method of Quadrature for Calculation of the Laminar and Turbulent Boundary in Case of Plane and Rotationally Symmetrical Flow." U.S. National Advisory Committee for Aeronautics, NACA-TN-1379.

Udovich, N. 1973. "The Physics of Eolian Erosion and Deposition Around a Crater." Unpublished report submitted to the Physics Department, University of Santa Clara, California.

Warnock, H. 1948. Engineering Hydraulics. New York: Wiley.

Weinberger, R. K. and G. L. Adlon. 1971. "Particle Dislodgement and Entrainment by a Low Density Airstream Flowing over a Surface." National Aeronautics and Space Administration, NASA CR 111924.

White, C. M. 1940. "The Equilibrium of the Grains of the Bed of a Stream." Proceedings of the Royal Society of London, Series A, 174, No. 958: 322-328.

White, S. J. 1970. "Plane Bed Thresholds of Fine Grained Solids." Nature 228: 152-153.

Willmarth, W. W. and R. L. Enlow. 1969. "Aerodynamic Lift and Moment Fluctuations of a Sphere." Journal of Fluid Mechanics 36, Part 3: 417-432.

Zingg, A. W. 1953. "Wind Tunnel Studies of the Movement of Sedimentary Material." Proceedings of the 5th Hydraulic Conference, Bull. 24, University of Iowa Studies in Engineering: 111-135.

IX. ACKNOWLEDGMENT

X.   APPENDIX A

Listed here are the formulas used to calculate the drag coefficient numerically in the computer programs that numerical solved the system of ordinary differential equations of the motion of the particle's trajectory.

$C_D = 24.0/R$ for $R \leq 0.1$

$C_D = 22.73/R + 0.0903/R^2 + 3.69$ for $0.1 < R \leq 1.0$

$C_D = 29.1667/R - 3.8889/R^2 + 1.222$ for $1.0 < R \leq 10.0$

$C_D = 46.5/R - 116.67/R^2 + 0.6167$ for $10.0 < R \leq 100.0$

$C_D = 98.33/R - 2778.0/R^2 + 0.3644$ for $100.0 < R \leq 1000.0$

$C_D = 148.62/R - 4.75 \times 10^4/R^2 + 0.357$ for $1000.0 < R \leq 5000.0$

$C_D = -490.546/R + 57.87 \times 10^4/R^2 + 0.46$

$\qquad\qquad\qquad\qquad$ for $5000.0 < R \leq 10000.0$

$C_D = -1662.5/R + 5.4167 \times 10^6/R^2 + 0.5191$

$\qquad\qquad\qquad\qquad$ for $10000.0 < R \leq 50000.0$

$C_D = 0.4$ for $R > 50000.0$

XI.   APPENDIX B

Two-dimensional Equations of Motion

$$m_p\ddot{x} = \frac{\pi}{8}\,\rho\Delta V_r D_p^2[(u-\dot{x})C_D + (\dot{z} - w)C_L] \tag{B.1}$$

$$m_p\ddot{z} = \frac{\pi}{8}\,\rho\Delta V_r D_p^2[(w-\dot{z})C_D + (u-\dot{x})C_L]-m_p g \tag{B.2}$$

$$\text{where}\qquad \Delta V_r = \sqrt{(u-\dot{x})^2 + (w-\dot{z})^2} \tag{B.3}$$

$$m_p = \pi\rho D_p^3/6 \tag{B.4}$$

Dimensionless Equations of Motion

$$\hat{\ddot{x}} = 0.75\,\frac{\rho}{\rho_p}\,\Delta\,\hat{V}_r[(\hat{\dot{z}}-\hat{w})C_L + (\hat{u}-\hat{\dot{x}})C_D] \tag{B.5}$$

$$\hat{\ddot{z}} = 0.75\,\frac{\rho}{\rho_p}\,.\,\Delta\hat{V}_r[(\hat{u}-\hat{\dot{x}})C_L + (\hat{w}-\hat{\dot{z}})C_D]-\hat{g} \tag{B.6}$$

$$\text{where}\qquad \hat{x} = x/D_p \;;\; \hat{\dot{x}} = \dot{x}/u_* \;;\; \hat{\ddot{x}} = \ddot{x}D_p/u_*^2 \tag{B.7}$$

$$\hat{g} = gD_p/u_*^2 \;;\; \hat{u} = u/u_* \;;\; \hat{\Delta V}_r = \Delta V_r/u_*$$

Three-dimensional Equations of Motion

$$m_p\ddot{x} = \frac{\pi}{8}\,\rho\Delta V_r^2 D_p^2\left[\frac{(u-\dot{x})}{\Delta V_r}\,C_D + L_x C_L\right] \tag{B.8}$$

$$m_p\ddot{y} = \frac{\pi}{8}\,\rho\Delta V_r^2 D_p^2\left[\frac{(v-\dot{y})}{\Delta V_r}\,C_D + L_y C_L\right] \tag{B.9}$$

$$m_p \ddot{z} = \frac{\pi}{8} \rho \Delta V_r^2 D_p^2 \left[\frac{(w-\dot{z})}{\Delta V_r} \; C_D + L_z C_L \right] - m_p g \qquad (B.10)$$

where

$$L_x = \frac{(w-\dot{z})[v(w-\dot{z})-w(v-\dot{y})] - (u-\dot{x})[u(v-\dot{y})-v(u-\dot{x})]}{\Delta L} \qquad (B.11)$$

$$L_y = \frac{(v-\dot{y})[u(v-\dot{y})-v(u-\dot{x})] - (w-\dot{z})[w(u-\dot{x})-u(w-\dot{z})]}{\Delta L} \qquad (B.12)$$

$$L_z = \frac{(u-\dot{x})[w(u-\dot{x})-u(w-\dot{z})] - (v-\dot{y})[v(w-\dot{z})-w(v-\dot{y})]}{\Delta L} \qquad (B.13)$$

$$\Delta L = \left[\{(w-\dot{z})[v(w-\dot{z})-w(\dot{v}-\dot{y})] - (u-\dot{x})[u(v-\dot{y})-v(u-\dot{x})]\}^2 \right.$$

$$+ \{(v-\dot{y})[u(v-\dot{y})-v(u-\dot{x})] - (w-\dot{z})[w(u-\dot{x})-u(w-\dot{z})]\}^2$$

$$\left. + \{(u-\dot{x})[w(u-\dot{x})-u(w-\dot{z})] - (v-\dot{y})[v(w-\dot{z})-w(v-\dot{y})]\}^2 \right]^{1/2} \qquad (B.14)$$

Dimensionless Equations of Motion

$$\hat{\ddot{x}} = 0.75 \frac{\rho}{\rho_p} \Delta \hat{V}_r^2 \left[L_x C_L + \frac{(\hat{u}-\hat{\dot{x}})C_D}{\Delta \hat{V}_r} \right] \qquad (B.15)$$

$$\hat{\ddot{y}} = 0.75 \frac{\rho}{\rho_p} \Delta \hat{V}_r^2 \left[L_y C_L + \frac{(\hat{v}-\hat{\dot{y}})C_D}{\Delta \hat{V}_r} \right] \qquad (B.16)$$

$$\hat{\ddot{z}} = 0.75 \frac{\rho}{\rho_p} \Delta \hat{V}_r^2 \left[L_z C_L + \frac{(\hat{w}-\hat{\dot{z}})C_D}{\Delta \hat{V}_r} \right] - \hat{g} \qquad (B.17)$$